Quantifying Dust Deposition over the Atlantic Ocean

Emmanouil Proestakis[1,2], Vassilis Amiridis[1], Carlos Pérez García-Pando[3,4], Svetlana Tsyro[5], Jan Griesfeller[5], Antonis Gkikas[6], Thanasis Georgiou[1,7], María Gonçalves Ageitos[3,8], Jeronimo Escribano[3], Stelios ~~Myriokefalitakis[1]~~Myriokefalitakis[8], Elisa Bergas Masso[3,~~8~~9], Enza Di Tomaso[3,a], Sara Basart[3,b], Jan-Berend W. ~~Stuut[9]~~Stuut[10,~~10~~11], Angela ~~Benedetti[11]~~Benedetti[12]

[1]Institute for Astronomy, Astrophysics, Space Applications and Remote Sensing, National Observatory of Athens, Athens, Greece.
[2]School of Chemical and Environmental Engineering, Technical University of Crete, Chania, Greece.
[3]Barcelona Supercomputing Center (BSC), Barcelona, Spain.
[4]Catalan Institution for Research and Advanced Studies (ICREA), Barcelona, Spain.
[5]Research and Development Department, Norwegian Meteorological Institute, Oslo, Norway.
[6]Research Centre for Atmospheric Physics and Climatology, Academy of Athens, Athens, Greece.
[7]School of Physics, Faculty of Sciences, Aristotle University of Thessaloniki, Thessaloniki, Greece.
[8]Institute for Environmental Research and Sustainable Development, National Observatory of Athens, Penteli, Greece
~~[8]Universitat~~ [9]Universitat Politècnica de Catalunya, Barcelona, Spain.
~~[9]Royal~~ [10]Royal Netherlands Institute for Sea Research, The Netherlands.
~~[10]Vrije~~ [11]Vrije Universiteit Amsterdam, the Netherlands.
~~[11]Research~~ [12]Research Department, European Centre for Medium-Range Weather Forecasts, Reading, UK.
[a] now at: European Centre for Medium-Range Weather Forecasts (ECMWF), Bonn, Germany.
[b] now at: World Meteorological Organisation (WMO), Science and Innovation Department, 1201 Geneva, Switzerland.

Correspondence to: Emmanouil Proestakis (proestakis@noa.gr)

Abstract. Quantification of atmospheric dust deposition into the Atlantic Ocean is provided. The estimates rely on the four-dimensional structure of atmospheric dust provided by the ESA-LIVAS climate data record established on the basis of CALIPSO-CALIOP observations. The data record of atmospheric dust deposition rate is provided for the Atlantic Ocean region, between latitudes 60°S to 40°N, and is characterized by 5° (zonal) x 2° (meridional) spatial resolution, seasonal-mean temporal resolution, for the period 12/2006-11/2022. The estimates of dust deposition are evaluated on the basis of sediment-trap measurements of deposited lithogenic material. The evaluation intercomparison shows a good agreement between the two datasets, revealing the capacity of the satellite-based product to quantitatively provide the amount of dust deposited into the Atlantic Ocean, characterized by correlation coefficient of 0.79 and mean bias of 5.42 mg m^{-2} d^{-1}. Integration of the satellite-based dust deposition rate dataset into AeroVal allowed assessment comparison of the dust deposition product against dust deposition field estimates provided by MONARCH, EMEP MSC-W, and EC-Earth3-Iron models. The comparison revealed the capacity of the satellite-based product to follow the seasonal activation of dust source regions and the four-dimensional migration of dust transport pathways. Overall, the annual-mean amount of dust deposition into the Atlantic Ocean is estimated at 274.79 ± 31.64 Tg yr^{-1}, of which 243.98 ± 23.89 Tg yr^{-1} of dust is deposited into the North Atlantic Ocean and 30.81 ± 10.49 Tg yr^{-1} of dust is deposited into the South Atlantic Ocean. Moreover, a negative statistically significant trend in atmospheric

dust deposition over the Atlantic Ocean is revealed. The satellite-based dust deposition product is considered unique with respect to a wide range of potential applications, including compensating for geographical and temporal gaps of sediment-trap measurements, supporting evaluation assessments of model simulations, unravelling physical processes related to the atmospheric cycle of dust, and providing deeper understanding of dust biogeochemical impacts on oceanic ecosystems, weather, and eventually climate.~~Quantification of atmospheric dust deposition into the Atlantic Ocean is provided. The estimates rely on the four-dimensional structure of atmospheric dust provided by the European Space Agency (ESA) "LIdar climatology of Vertical Aerosol Structure" (LIVAS) climate data record (CDR) established on the basis of Cloud-Aerosol Lidar and Infrared Pathfinder Satellite Observations (CALIPSO) – Cloud-Aerosol Lidar with Orthogonal Polarization (CALIOP) routine observations. The data record of atmospheric dust deposition rate is provided for the broader Atlantic Ocean region, the Caribbean Sea, and the Gulf of Mexico, confined between latitudes 60°S to 40°N, and is characterized by 5° (zonal) x 2° (meridional) spatial resolution, seasonal-mean temporal resolution, and for the period extending between 12/2006 and 11/2022. The estimates of dust deposition are evaluated on the basis of sediment-trap measurements of deposited lithogenic material implemented as reference dataset with good agreement between the two datasets, revealing the capacity of the satellite-based product to quantitatively provide the amount of dust deposited into the Atlantic Ocean region, as shown by the evaluation intercomparison, evaluation intercomparison characterized by correlation coefficient ~0.79 and mean bias of 5.42 mg/m^2d. Moreover, integration of the satellite-based dust deposition rate dataset into AeroVal allows assessment comparison of the variability amongst the dust deposition CDR and dust deposition field estimates provided by the Multiscale Online Nonhydrostatic AtmospheRe CHemistry (MONARCH), EMEP MSC-W, and EC-Earth3-Iron Earth System Models (ESM), with the comparison revealing the capacity of the satellite-based product to follow the seasonal activation of dust source regions and the four-dimensional migration of dust transport pathways. Overall, the annual-mean amount of dust deposition into the Atlantic Ocean is estimated at 274.79 ± 31.64 Tg yr^{-1}, of which 243.98 ± 23.89 Tg yr^{-1} of dust is deposited into the North Atlantic Ocean and 30.81 ± 10.49 Tg yr^{-1} of dust is deposited into the South Atlantic Ocean. Moreover, a negative statistically significant trend in Atlantic Ocean dust deposition is also revealed. The satellite-based dust deposition CDR is considered unique with respect to a wide range of potential applications, including compensating for geographical and temporal gaps of sediment-trap measurements, supporting evaluation assessments of model simulations, shedding light into physical processes related to the cycle of dust from emission to transport and eventually deposition, and providing a solid basis to better understand dust biogeochemical impacts on oceanic ecosystems, as well as impacts on weather and climate.~~

1 Introduction

The ocean plays a key role in climate by modulating energy fluxes and exchanging climate-relevant gases with the atmosphere. According to the Intergovernmental Panel on Climate Change Fifth Assessment Report (IPCC AR5 2014), ~90% of the total energy in excess in the atmosphere was absorbed by the ocean between 1971 and 2010. At the same time, gaseous CO_2 is absorbed in the surface layer of the ocean and becomes available for the process of "photosynthesis" performed by

phytoplankton cells, contributing through the processes of the "biological carbon pump" and the "solubility carbon pump" (Volk and Hoffert, 1985; Ito and Follows, 2003) to the slowing down of the increase of atmospheric CO_2 that results from anthropogenic activities (Raupach et al., 2008). Moreover, phytoplankton abundance and variability regulate ~~Ocean~~ ocean ~~Colour~~colour, which in turn determines the extent of light penetration in the water column (Hostetler et al., 2018), affecting sea surface temperature and resulting in potentially significant ocean-atmosphere feedbacks, such as possible determining the trajectory of tropical storms (Gnanadesikan et al., 2010).

Current estimates of primary production range between 30 and 70 Pg-C per year (Carr et al., 2006; Anav et al., 2013) with spatial distribution depending, among other factors, on the input of nutrients from the atmosphere (Krishnamurthy et al., 2010; Guerreiro et al., 2019; 2023; Myriokefalitakis et al., 2020). Among the key nutrients deposited into the open ocean, nitrogen (N), phosphorus (P), silica (SiO_2), and iron (Fe) are critical for regulating phytoplankton growth, and consequently for modulating marine productivity, ocean colour, and the ocean's capacity to absorb CO_2. Among these atmospheric deposited species, Fe availability is the most predominant limiting nutrient for phytoplankton growth over large oceanic areas (Jickells et al., 2005; Okin et al., 2011). Indeed, due to the key role of phytoplankton in the conversion of CO_2 into organic carbon and to carbon sequestration, Fe deposition, and more specifically its bioavailable (dissolved) forms (e.g., aqueous, colloidal, or nanoparticulate), likely plays a major role in oceanic primary productivity (Tagliabue et al., 2017) with impact on the global carbon cycle, hence modulating atmospheric CO_2 concentrations (Falkowski et al., 2000; Guerreiro et al., 2021) and in the long term the global climate. Another important biogeochemical parameter to characterize ocean productivity is marine nitrogen fixation, i.e., the reduction of gaseous N_2 to ammonium performed by marine organisms. N_2-fixing species (e.g., diazotrophs) have elevated Fe requirements and their growth may also be Fe-limited over large areas of the Atlantic Ocean (Pabortsava et al., 2017; Schlosser et al, 2014).

However, iron concentrations in vast areas of the ocean are very low, further enhanced by the characteristic low solubility of iron in seawater (Boyd and Ellwood, 2010). Across the broader surface of the open ocean, aeolian dust is the principal source of Fe (~95%), followed by Fe-containing aerosols from biomass burning and fossil-fuel combustion emissions (Mahowald et al., 2009). It should be noted that observations and laboratory experiments suggest that the solubility of bioavailable dissolved iron (DFe) in pyrogenic aerosols may be significantly higher than that in lithogenic aerosols, though considerably more sporadic than DFe from mineral dust (Ito et al., 2021). Mineral dust of natural sources, essentially composed of clay, silt, and soil particles (Adebiyi et al., 2023), is mechanically produced by surface winds breaking soil cohesion over surfaces with no vegetation and dry soil such as deserts. According to Yu et al. (2015b) and Kok et al., (2021; 2023) North Africa, including the Saharan desert and the Sahel area, is the biggest producer of mineral dust contributing to approximately 50% of the global atmospheric dust load (~2100 Tg yr^{-1}). Other natural sources of dust emission encompassing the South Atlantic Ocean include the desert areas of South Africa and South America, with estimated emissions of ~100 Tg yr^{-1} and ~190 Tg yr^{-1}, respectively (Kok et al., 2021; 2023). In addition to natural sources, the contribution of dust emitted into the atmosphere from anthropogenic activities remains elusive, with estimated values ranging between 10% and 50% (e.g., Ginoux et al., 2012). Upon emission into the atmosphere mineral dust particles are subject to aeolian transport over distances of thousands of kilometers downwind,

prior removal through wet deposition (i.e. scavenging through precipitation in the water or ice phase), dry deposition/gravitational settling, and turbulent mixing in the Planetary Boundary Layer (PBL) (Gao et al., 2003; Hand et al., 2004; Prospero et al., 2010; Mahowald et al., 2011; ~~Van~~ van der Does et al., 2021).

To date, one of the biggest unknowns in the dust cycle remains the amount of atmospheric dust which is actually deposited into the open ocean. Ridley et al. (2012), on the basis of reanalysis models and satellite observations, estimated dust deposition into the Atlantic Ocean of the order of approximately 218 ± 48 Tg yr^{-1}, though the model timeseries covered only two years. Kaufman et al. (2005), on the basis of Terra - Moderate Resolution Imaging Spectroradiometer (MODIS) routine aerosol observations, quantified the amount of Saharan dust deposited into the Atlantic Ocean and the Caribbean Sea to approximately 190 Tg yr^{-1}. Huneeus et al. (2011) performed cross-evaluation of a dozen global aerosol models against observed dust deposition measurements and reported discrepancies of up to an order of magnitude. Kok et al. (2023) estimated that dust emissions from the Saharan, Namib, Kalahari, and Atakama hyper-arid, arid, semi-arid, and dry subhumid areas encompassing the broader Atlantic Ocean contribute to approximately 230 Tg yr^{-1} and 86 Tg yr^{-1} of dust deposition into the North and South Atlantic Ocean, respectively. The estimated deposition fluxes were based on particles with geometric (volume-equivalent) diameter up to 20 μm, though larger dust particles have been measured aeolian transported in the atmosphere (Weinzierl et al., 2016; Ryder et al., 2018) and deposited in the ocean (van der Does et al., 2018b), ~~and~~ not accounting for high-latitude dust emission sources (Cvetkovic et al., 2022). ~~Reanalysis datasets of dust deposition, such as the Copernicus Atmosphere Monitoring Service (CAMS; Inness et al., 2019), are available but have not yet been validated with independent observations over the ocean.~~ Similarly, Yu et al. (2019) on the basis of a ten-year (2007-2016) analysis of Cloud Aerosol Lidar with Orthogonal Polarization (Winker et al., 2010), ~~MODerate resolution Imaging Spectroradiometer (~~MODIS~~)~~ (Remer et al., 2005), Multiangle Imaging Spectroradiometer (MISR) (Garay et al., 2020), and Infrared Atmospheric Sounding Interferometer (IASI) (Capelle et al., 2014) observations estimated the amount of dust deposited into the Tropical Atlantic Ocean in the range 136-222 Tg yr^{-1}, though the estimations correspond only to the Saharan dust outflow region (5°S - 40°N). Reanalysis datasets of dust deposition, such as the Copernicus Atmosphere Monitoring Service (CAMS; Inness et al., 2019), are available but have not yet been validated with independent observations over the ocean.

A better understanding and quantification of the atmospheric dust spatiotemporal variability in terms of deposition across the broader ocean would facilitate addressing long-open questions such as the relationship between dust deposition and dust biogeochemical impact processes on oceanic marine ecosystems. For instance, most IPCC-class Earth System Models (ESMs) use simplified climatological representations of dust deposition and of its composition and solubility to account for the effect of atmospheric nutrient inputs on ocean biogeochemical cycles (Aumont et al., 2015; Seland et al., 2020), although it is widely accepted that dust deposition is by nature highly episodic (Guieu et al., 2014). To date, models of the atmospheric iron cycle employed to simulate atmospheric Fe dissolution are characterized by different levels of complexity: from simple schemes including first-order rate processing constants applied to a globally uniform 3.5% of Fe in dust to more complex ones allowing different types of acidic species to interact with dust that account for mineral-specific dissolution rates and oxalate processing

(Myriokefalitakis et al., 2018; Ito et al., 2019). Model-based estimations on the global atmospheric dissolved dust-related Fe deposition fluxes into the ocean lie in the range 0.2–0.4 Tg-Fe yr^{-1} for present-day conditions (Myriokefalitakis et al., 2018; Ito et al., 2019), approximately a factor of ~2 higher than during the preindustrial times (Scanza et al., 2018; Bergas-Massó et al., 2023). However, atmospheric dust transport and deposition are also highly variable. Overall, is has been reported that dust mass increased up to 55 ± 30% since the preindustrial era (Kok et al., 2023). However recent studies debate on the magnitude of dust transport over the Atlantic Ocean, whether there is in recent years a decrease (Ridley et al, 2014) or increase (Cuevas-Agulló et al., 2023) on emission, transport, and deposition. Furthermore, future scenarios show a decrease in bioavailable Fe deposition in mid- and high-latitudes but an increase in equatorial regions such as the equatorial Pacific, Atlantic, and Indian Ocean. Those increases are sharper and have a broader extension for the SSP370 scenario, characterized by strong anthropogenic emission levels (Bergas-Massó et al., 2023). A potential increase (decrease) in dust transport and deposition over the ocean, could make iron and other nutrients, such as silica and phosphorus, more (less) available for phytoplankton (Gittings et al., 2024), hence triggering changes in marine primary productivity (Rodríguez et al., 2023), and the oceanic carbon pump (Volk and Hoffert, 1985; Ito and Follows, 2003), and climate.

The complex interactions of such mechanics are still not well understood. An integrated approach of modeling, satellite, and in-situ observations is needed to quantify the strength and the spatiotemporal characteristics of mineral dust deposition in the surface of the open ocean. An approach allowing to facilitate a better representation of the mechanisms behind the spatial and temporal variability of atmosphere-ocean interactions, key to interpret observed climatic change responses, and to better describe the future ones.

To date, satellite-based Earth Observations (EO) allow to address the link between atmospheric aerosol composition and ocean deposition over extensive areas and long temporal periods. It is important though to note emphasize that aerosol optical depth (AOD) or dust optical depth (DOD), as indicators of columnar total aerosol and dust aerosol load respectively, cannot be directly employed as proxies for total aerosol and dust deposition fluxes, as deposition processes are highly dependent on the vertical structure of aerosols in the atmosphere and the meteorologic conditions (Schepanski et al., 2009; Yu et al., 2013; 2015a2015b; 2019). However, a wealth of satellite-based observations on the four-dimensional (4-D) distribution of aerosols over oceans has become available during the past decades. The main satellite-based active systems include the Cloud-Aerosol Transport System (CATS) (McGill et al., 2015; Yorks et al., 2016; Proestakis et al., 2019) aboard the International Space Station (ISS; Rodier et al., 2015), the Atmospheric Laser Doppler Instrument (ALADIN) aboard Aeolus (Stoffelen et al., 2005; Ansmann et al., 2007), the joint European Space Agency (ESA) and JAXA's satellite Earth Cloud, Aerosol and Radiation Explorer (EarthCARE; Illingworth et al., 2015), and CALIOP aboard the Cloud-Aerosol Lidar and Infrared Pathfinder Satellite Observation (CALIPSO; Winker et al., 2007; 2009). In addition, novel techniques have been proposed, including the one-step polarization Lidar Photometer Networking (one-step POLIPHON; Tesche et al., 2009; Ansmann et al., 2012) developed in the framework of the European Aerosol Research Lidar Network (EARLINET; www.earlinet.org/; last access: 21/08/2024; Pappalardo et al. 2014), allowing to decouple the atmospheric dust component from the total aerosol load and accordingly to estimate the dust mass concentration (Ansmann et al., 2019). To date, the one-step POLIPHON has been extensively applied

to CALIOP and CATS optical products to provide information on atmospheric dust (Amiridis et al., 2013; Marinou et al., 2017; Proestakis et al., 2018; 2024). At the same time, state-of-the-art global atmospheric reanalysis datasets, such as the European Centre for Medium-Range Weather Forecasts (ECMWF) reanalysis (ERA5) (Hersbach et al., 2020) have been established, providing comprehensive climate and weather data, including information on the three-dimensional wind components. Such advances allow through synergetic implementation computation of dust mass fluxes in both zonal and meridional directions over specified oceanic areas and thus estimations of the deposited component. Finally, during the past decades the available observations of the ocean's interior in terms of atmospheric deposited lithogenic material have tremendously increased, thanks to the deployment of arrays of submerged sediment traps (Albani et al., ~~2016~~2014; Van der Does et al., 2016; Korte et al., 2017).

~~The challenge of the present work is to bring together this wealth of information to provide a full 4D reconstruction of the atmospheric dust component and accordingly estimate the atmospheric dust deposited component across the broader Atlantic Ocean. The paper is structured as follows: Sect. 2 provides an overview of the implemented datasets in terms of both satellite-based EOs and models (Sect. 2.1) and discusses the applied methodology (Sect. 2.2). Sect. 3 provides an overview of the three-dimensional (3-D) spatial distribution and temporal evolution of the dust aerosol in the atmosphere and the corresponding quantification of the dust deposited component across the broader Atlantic Ocean, based on more than 17 years of EOs (2007-2023). Sect. 4 provides a comprehensive evaluation of the EO-based dust deposition rate product, while comparison between the dust deposition rate product and ESMs is provided in Sect. 5. Sect. 6 provides and discusses quantification of the total atmospheric deposited dust mass into the broader Atlantic Ocean and Sect. 7 a summary of the study along with the main concluding remarks.~~The challenge of the present work is to bring together this wealth of information to provide a full four-dimensional reconstruction of the atmospheric dust component and accordingly to estimate the atmospheric dust deposited component across the broader Atlantic Ocean. The paper is structured as follows: Section 2 provides an overview of the implemented datasets in terms of both satellite-based EOs and models (Sect. 2.1) and discusses the applied methodology (Sect. 2.2). Section 3 provides an overview of the EO-based atmospheric dust and the dust deposition products (Sect. 3.1), the evaluation of the EO-based dust deposition estimates (Sect. 3.2), the quantification of the total atmospheric dust deposited into the broader Atlantic Ocean (Sect. 3.3), and finally the EO-based dust deposition rate intercomparison against respective ESMs outcomes (Sect. 3.4). Section 4, as the final part of this work, provides the summary of the study along with the main concluding remarks.

2 Datasets and Methodology

2.1 Datasets

2.1.1 CALIPSO-CALIOP

The Cloud-Aerosol Lidar and Infrared Pathfinder Satellite Observation (CALIPSO) environmental satellite is a joint~~-~~ satellite mission ~~venture~~ between the United States space agency National Aeronautics and Space Administration (NASA) and the French space agency Centre National D'Études Spatiales (CNES), developed to provide insight into and ~~and~~ eventually advance our fundamental understanding on the role of aerosols and clouds on weather and climate (Winker et al., 2010). CALIPSO was launched on the 28th of April 2006 to join with CloudSat the international Afternoon-Train (A-Train) group of polar-orbiting sun-synchronous satellites (Stephens et al., 2018), carrying a suite of three Earth-Observing instruments into space: an Imaging Infrared Radiometer (IIR; Garnier et al., 2017), a wide field-of-view camera (WFC), and the Cloud-Aerosol Lidar with Orthogonal Polarization (CALIOP) lidar (Hunt et al., 2009). CALIOP, the CALIPSO primal payload, ~~consists~~ consisted of a two-wavelength elastic backscatter Nd:YAG lidar system, emitting linearly polarized light-pulses at 532 and 1064 nm, and conducting range-resolved measurements of the parallel and perpendicular backscattered components at 532 nm and of the total backscatter intensity at 1064 nm (Winker et al., 2009).

CALIOP Level 2 (L2) optical products are established on the basis of a sequence of successive ~~sophisticated~~ algorithms ensuring, among others, daytime and nighttime calibration (Powell et al., 2009; Getzewich et al., 2018; Kar et al., 2018; Vaughan et al., 2019), atmospheric layer detection (Vaughan et al., 2009), and cloud-aerosol discrimination (Liu et al., 2009; Liu et al., 2019; Zeng et al., 2019). The detected atmospheric features classified as "tropospheric" or "stratospheric" aerosol are further sub-classified between "marine", "dust", "polluted continental/smoke", "clean continental", "polluted dust", "elevated smoke", "dusty marine", "PSC aerosol", "volcanic ash", and "sulfate/other" categories (Omar et al., 2009; Kim et al., 2018, Kar et al., 2019), a classification crucial towards retrieval of extinction coefficient profiles on the basis of backscatter coefficient profiles (Young and Vaughan, 2009). Here, we use CALIOP ~~L2~~ level 2 (L2) Version 4.5 (V4.5) Aerosol Profile (APro) and Cloud Profile (CPro) optical products (i.e., backscatter coefficient and particulate depolarization ratio at 532 nm), profile geolocation descriptors (i.e., longitude, latitude, time), quality-assurance (i.e., Cloud-Aerosol-Discrimination) and atmospheric classification flags (i.e., feature type, aerosol subtype) along the CALIPSO orbit path, provided at 5 km horizontal resolution and 60 m vertical resolution, for the Atlantic Ocean geographical domain confined between 40°N and 60°S latitude, and for the temporal period extending between 12/2006 and 11/2022. Accordingly, mean pure dust extinction coefficient at 532 nm profiles within each 5° (zonal) x 2° (meridional) spatial resolution are produced through aggregation and averaging of all quality-assured cloud-free :2 5 km pure dust profiles located within each latitude, longitude, altitude grid cell per each season, following the averaging approach provided and discussed in Tackett et al. (2018) (Sect. 2.2.1).

2.1.2 ERA5

The ERA5 dataset is a global reanalysis product that provides estimates of atmospheric, land, and oceanic variables from 1950 onward, with continuous updates in near real-time up to the present day (Hersbach et al., 2020). ERA5 is produced by ECMWF, for the Copernicus Climate Change Service (C3S), by combining historical observations with ECMWF's Integrated Forecast System (IFS) model. Atmospheric variables are available at a horizontal resolution of 0.25°×0.25° considered as a continuous tiled surface with the point coordinates corresponding to the centroids of the tiles.

In the framework of the study, we use the ERA5 seasonally averaged zonal and meridional components of wind (m/s) from 12/2006 and 11/2022. The vertical resolution of ERA5, in pressure levels between 1000 hPa and 1 hPa, is converted to height above mean sea level based on geopotential (Φ) using an approximation for variation of gravity with altitude and assuming a spherical Earth and no centrifugal force effects (Wallace and Hobbs, 2006~~Hobbs, 2006~~). The ERA5 wind speed parameters in the original regular latitude/longitude grid in the region of interest ~~RoI~~ are re-gridded into a uniform spatial grid of 2° latitude by 5° longitude and of seasonal temporal resolution. Figure 1 shows the ERA5 annual mean speed of the horizontal component of wind for the period extending between 12/2006 and 11/2022.

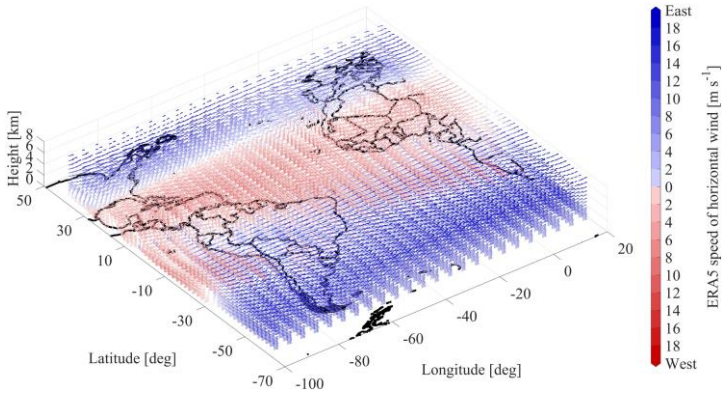

Figure 1: ERA5 annual mean speed of the horizontal component of wind for the period 12/2006 and 11/2022.

2.1.3 Dust deposition with the EC-Earth3-Iron Earth System Model

EC-Earth3 (Döscher et al., 2022) is a state-of-the-art ~~Earth System Model (~~ESM~~)~~, with a modular structure in which different Earth System components (atmosphere, ocean, sea ice, land surface, dynamic vegetation, atmospheric composition, and ocean biogeochemistry) that can be coupled in various model configurations according to ~~the~~ specific scientific needs. In this work, we apply the EC-Earth3-Iron (Myriokefalitakis et al., 2021; Bergas Massó et al., ~~2022~~2023) version, with a configuration that accounts for atmospheric dynamics and land surface processes through the Integrated Forecast System (IFS) cycle 36r4 from the ECMWF, and the interactive simulation of atmospheric aerosols and reactive gas species via the Tracer Model 5 (TM5) (van Noije et al. 2021), including a complex aqueous phase chemistry and an interactive calculation of aerosol and in-cloud pH (Myriokefalitakis et al., 2022). The modal aerosol microphysical scheme M7 (Vignati et al., 2004) represents different aerosol components~~,~~ and considers internally mixed particles in four water-soluble (nucleation, Aitken, accumulation, and

coarse) and three insoluble modes (Aitken, accumulation, and coarse). Dust emission is calculated online, following Tegen et al. (2002, 2004). Freshly emitted dust aerosols are allocated in the accumulation and coarse insoluble modes, but they are allowed to become soluble via atmospheric processing (further details are provided in Table 1).

To reproduce close-to-reality present-day climate conditions, the model is executed in an atmosphere-chemistry coupled mode using observed ocean conditions (sea surface temperature and sea ice concentration) as in the Atmospheric Model Intercomparison Project (AMIP) protocol (Gates et al., 1999). Furthermore, the atmospheric circulation is constrained towards ERA5 reanalysis data (Herbach et al., 2020), by adjusting the modeled wind vorticity and divergence through Newtonian relaxation towards the reanalysis.

The simulation period spans from the year 1991 to 2020. For the 1991-2014 period, anthropogenic and biomass burning emissions are taken from the Coupled Model Intercomparison Phase 6 (CMIP6) historical datasets (Hoesly et al., 2018), while for the 2015-2020, we have selected an intermediate scenario from those defined in the CMIP6 protocol, the SSP2-4.5 (Gidden et al., 2019). The model is executed at the standard spatial resolution, with T255L91 for IFS (approximately 80 km at mid-latitudes, and 91 vertical levels) and 3°x2° and 34 vertical levels for TM5.

2.1.4 Dust simulation with the EMEP MSC-W Model

EMEP MSC-W chemical transport model (herefrom referred to as EMEP model) has been used to perform simulations of the global load and deposition of mineral dust ~~discussed in this paper~~. The EMEP model is extensively used for air quality assessments in Europe and globally, both for policy related issues and research studies. The parameterisation of windblown dust emissions from deserts, arid areas, and arable lands used in the EMEP model is based on the works of Marticorena and Bergametti (1995), Marticorena et al. (1997), Alfaro and Gomes (2001), Gomes et al. (2003), and Zender et al. (2003). Dust particles up to 10 μm in diameter, represented by two size fractions (fine and coarse), are presently considered by the model. Aerosol extinction coefficient is diagnosed from the modeled ~~3d~~ three-dimensional fields of mass concentrations of individual aerosols, including mineral dust, using ~~Mass~~ mass ~~Extinction~~ extinction ~~Coefficients~~ coefficients based on Chin et al. (2002) and Hess et al. (1998). The EMEP simulations for the year 2020 have been made on a resolution of 0.5°x0.5°, driven by ECMWF IFS 3-hourly meteorological fields for the actual year. Dry and wet deposition of mineral dust, as well as DOD, have been outputted on a daily basis. A comprehensive description of the EMEP MSC-W model can be found in Simpson et al. (2012)~~, Simpson et al. (2024, in preparation)~~, with further details provided in Table 1.

2.1.5 Dust simulation with the MONARCH model

The Multiscale Online Nonhydrostatic AtmospheRe CHemistry (MONARCH) model (Klose et al., 2021 and references therein) is a fully coupled atmosphere-chemistry model developed by the Earth Sciences Department of the Barcelona Supercomputing Center (BSC). MONARCH atmospheric dynamics rely on the Non-hydrostatic Multiscale Model on the B-grid (NMMB) (Janjic, 2003; Janjic and Gall, 2012). The model incorporates an advanced representation of the atmospheric dust cycle, including dust generation and uplift by surface winds and turbulence, transport through advection~~,~~ and diffusion

and~~,~~ vertically~~,~~ by turbulence and convection. Removal of dust from the atmosphere occurs in MONARCH through gravitational settling in the atmospheric column, dry deposition through turbulent diffusion, as well as via wet deposition, including in-cloud and below-cloud scavenging from stratiform and convective clouds (Pérez et al., 2011, Haustein et al., 2012; Klose et al., 2021). Dust is represented by a sectional size distribution including 8 log-normal bins that cover up to 20 μm in diameter. For this work, dust emission from saltation is represented following Ginoux et al. (2001) with the modifications described in Klose et al. (2021), and follows a size distribution at emission invariant with wind speed (Kok ~~et al.~~, 2011). Dust emissions are corrected by factors issued from a modified version of the Local Ensemble Transform Kalman Filter assimilation procedure where we target the correction of emissions in spatial scales of tens to few hundreds of kilometers. This system assimilates dust-filtered AOD from SNPP-VIIRS Deep Blue retrievals in the MONARCH with the dust filtering procedure described in Escribano et al. (2022). The lagged assimilation method uses 20 members, with a moving 15 days assimilation window around and ahead each estimate. The control vector consists of dust emission scaling factors, which have a temporal resolution of three days and the native spatial resolution of the model. These factors improve the spatial distribution of dust emissions in the model, but they do not change significatively the accumulated emissions of dust in seasonal and yearly scales (Escribano et al., 2023).

Dust interacts with long- and short-wave radiation, which is resolved by the model radiation scheme RRTM-G (Iacono et al., 2000, 2008). For the experiments presented here, dust particles are assumed non-spherical, long-wave optical properties are derived from the Optical Properties of Aerosols and Clouds (OPAC) dataset (Hess et al., 1998) and short-wave refractive indices consider internal mixtures of different minerals present in dust (Klose et al., 2021).

MONARCH experiments are run at the global scale (with 1°x1.4° horizontal resolution in latitude and longitude, and 48 vertical layers up to 10 hPa), for the year 2020 using more than 1 year of spin-up. The meteorological variables are initialized every 24 hours from ERA-Interim reanalysis data (Berrisford et al., 2009; Dee et al., 2011)~~,~~ to constrain the modelled circulation towards close-to-reality fields, while the soil variables and dust are kept as calculated by the model in the initialization (further details are provided in Table 1). Dust concentrations, AOD, and dry/wet deposition rates are direct outputs from the models and were provided as daily fields (at their respective grids), which were averaged to obtain the monthly mean fields to be used in the AeroVal evaluations and consistency checks. No special selection of days with dust events has been made, so that the monthly mean values include both data in dusty and not-dusty days, consistent with EO-based dust products used here.

Table 1: EC-Earth3-Iron ESM, EMEP MSC-W, and MONARCH configuration.

	EC-Earth3-Iron ESM	EMEP MSC-W	MONARCH
Resolution	IFS (T255L91), TM5 (3ºx2º,34 layers)	0.5°-x-0.5 °	~~1° in latitude and x~~1.4°x1° ~~in longitude,~~ 48 vertical layers
Meteorology	Online IFS 36r4	ECMWF IFS 3-hourly	Online NNMB

Dust emission scheme	Based on Tegen et al. (2002, 2004)	Based on Marticorena and Bergametti (1995), Marticorena et al. (1997), Alfaro and Gomes (2001), Gomes et al. (2003), and Zender et al. (2003). Dust fluxes are distributed within the lowest, 45 m thick layer.	G01-UST of Klose et al. (2021)
Dust size distribution	2 modes (accumulation, coarse)	2 size bins (fine and coarse), up to 10 μm.	8 size bins (with boundaries at 0.2, 0.36, 0.6, 1.2, 2.0, 3.6, 6.0, 12.0, 20.0 μm of diameter)
Dust dry deposition	Resistance based dry deposition scheme (land-use dependent), gravitational settling from the lowest layer	Landuse dependent dry deposition, gravitational settling from the lowest layer	Gravitational settling and turbulent diffusion schemes
Dust wet deposition	Scavenging by precipitation in convective clouds and in-cloud and below-cloud scavenging for stratiform clouds.	In-cloud scavenging (based on scavenging ratios) and sub-cloud washout.	In-cloud and below-cloud scavenging from stratiform and convective clouds
AOD calculation	Aerosol optical properties consider internal mixtures of the different aerosol components in each mode (van Noije et al., 2014). The refractive indices for dust particles are taken from the aerosol-climate model ECHAM-HAM (Zhang et al., 2012)	Calculated for fine and coarse dust using Mass Extinction coefficients (Chin et al., 2002; Hess et al., 1998).	Aerosol optics consider non-spherical aerosols with refractive indexes computed by representative mineral fractions (Table 6 in Klose et al. 2021)
References	van Noije et al. (2021), Myriokefalitakis et al. (~~2023~~2022)	Simpson et al. (2012), ~~Simpson et al. (2024, *in preparation*).~~	Perez et al. (2011); Klose et al. (2021) and references therein

2.2 Methodology

2.2.1 Decoupling the atmospheric pure-dust component from the total aerosol load

Decoupling of the atmospheric ~~pure~~ dust component from the total aerosol load is performed on the basis of the one-step POLIPHON (Tesche et al., 2009; Ansmann et al., 2012) technique, established in the framework of EARLINET (www.earlinet.org/; last access: 21/08/2023; Pappalardo et al. 2014). As discussed and demonstrated in the framework of the European Space Agency (ESA) - LIdar climatology of Vertical Aerosol Structure for space-based lidar simulation studies activity (LIVAS; Amiridis et al., 2015) project, proper implementation of the one-step POLIPHON technique to CALIPSO L2 optical products at 532 nm towards derivation of the four-dimensional atmospheric dust climate data record requires a sequence

of intermediate steps, considerations, and assumptions. Figure 2 provides an illustration of the methodology towards establishing the ESA-LIVAS atmospheric dust product of the ~~CDR~~climate data record, on the basis of a CALIPSO nighttime granule over the broader Atlantic Ocean on the 12th of August 2012 (Fig. 2a). As shown, two distinct dust plumes emitted from the broader Saharan Desert and the desert areas of South America were present over the North Atlantic Ocean and South Atlantic Ocean, respectively (areas "A" and "B" delineated by ellipses in yellow colour).

The first step relates to quality-assurance of the generated CALIPSO-based L2 atmospheric pure-dust product, following the procedures established in the framework of the official CALIPSO Level 3 (L3) aerosol products (Winker et al. 2013; Tackett et al., 2018) and the ESA-LIVAS database (Amiridis et al., 2013; Marinou et al., 2017; Proestakis et al., 2018; Proestakis et al., 2024). The quality-assurance criteria (Table 2) are conservatively selected here, aiming to balance between the removal of a significant number of low-quality features and the preservation of the dataset. The quality-screening procedures are iteratively applied to both CALIPSO L2 backscatter coefficient at 532 nm and particulate depolarization ratio at 532 nm profiles, prior application of the one-step POLIPHON technique.

Table 2: Quality control procedures and filtering applied in CALIPSO data.

	Quality Assurance procedures
1	Screen out all cloud features.
2	Aerosol extinction coefficient for "clear air" assigned equal 0.0 km^{-1}.
3	Screen out atmospheric features of CAD score outside the range [-100, -20].
4	Screen out atmospheric features of Extinction QC flag ≠ 0, 1, 16 and 18.
5	Screen out atmospheric features of aerosol extinction uncertainty ≤ 99.9 km^{-1}.
6	Screen out misclassified cirrus fringes.
7	Screen out isolated aerosol features of horizontal resolution 80 km.
8	Features of large negative extinction coefficient values ≤ -0.2 km^{-1}, detected ≤ 60 m a.g.l., are removed.
9	Features of large positive extinction coefficient values ≥ 2.0 km^{-1}, detected ≤ 60 m a.g.l., are removed.
10	Features of large positive pure-dust extinction coefficient values ≥ 0.25 km^{-1} (95th percentile) or large negative pure-dust extinction coefficient values ≤ -0.25 km^{-1} are removed.
11	Pure-dust extinction coefficient values above 10 km above mean sea level (a.m.s.l) are removed.
12	"Clear-Sky" Mode

Accordingly, the decoupling of the ~~pure~~ dust and non-dust atmospheric components is performed under two conditions. The first one relates to the consideration of atmospheric aerosol layers as external mixtures of two distinct aerosol-subtype classes with distinct depolarizing properties. Following the CALIPSO feature-type (Fig. 2b) and aerosol-subtype (Fig. 2c) classification algorithms and towards the overarching objective of decoupling the pure-dust component from the total aerosol load, the separation scheme assumes the "dust", "polluted dust", and "dusty marine" aerosol-subtypes as external mixtures of a "dust" and a "non-dust" component, while the rest of the "tropospheric" and "stratospheric" defined aerosol-subtype classes ~~is~~ are considered virtually dust-free (Kim et al., 2018, Kar et al., 2019). The first consideration, of external aerosol mixtures, allows for the second condition, that the total backscattered signal corresponds to the summation of the parallel and perpendicular backscattered signals by the two aerosol-subtype classes. Under these two conditions, and according to the one-

step POLIPHON technique, the contribution of the pure-dust aerosol component to the total aerosol load, in terms of backscatter coefficient, is calculated by Eq. (1).

$$\beta_{\lambda,d}(z) = \beta_{\lambda,p}(z)\frac{\left(\delta_{\lambda,p}(z) - \delta_{\lambda,nd}(z)\right)\left(1 + \delta_{\lambda,nd}(z)\right)}{\left(\delta_{\lambda,d}(z) - \delta_{\lambda,nd}(z)\right)\left(1 + \delta_{\lambda,p}(z)\right)} \quad (1)$$

In Eq. (1) the parameters "$\delta_{\lambda,p}(z)$", "$\beta_{\lambda,p}(z)$", and "$\beta_{\lambda,d}(z)$" correspond to the particulate depolarization ratio (Fig. 2d), total backscatter coefficient (Fig. 2e), and pure-dust backscatter coefficient (Fig. 2f), respectively, while the input constants of "$\delta_{\lambda,d}$" and "$\delta_{\lambda,nd}$" correspond to the typical particulate depolarization ratio of the pure-dust and non-dust components of the external aerosol mixture, expressed as functions of wavelength "λ" and height "z".

(a) CALIPSO nighttime granule 12/08/2012

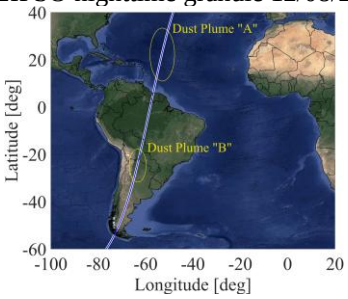

(b) CALIPSO Feature Type

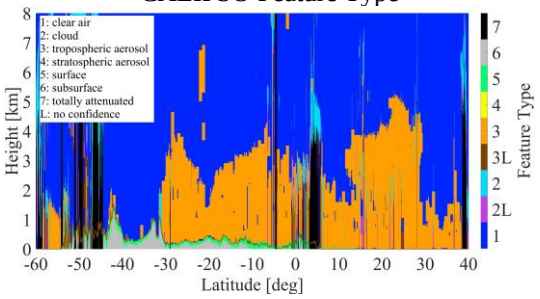

(c) CALIPSO Aerosol Subtype

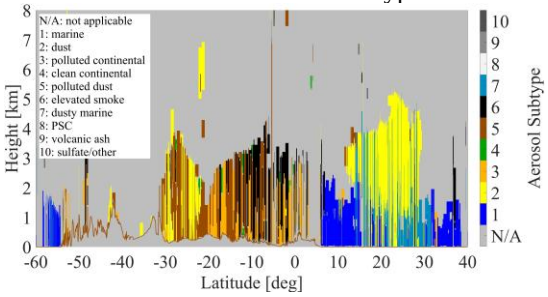

(d) Particulate Depolarization Ratio at 532 nm

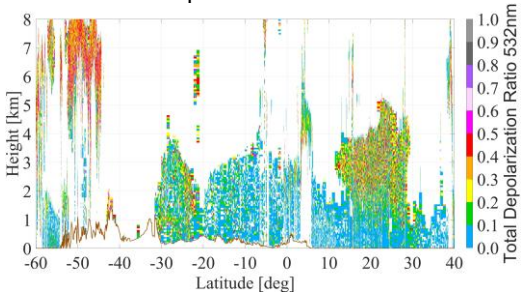

(e) Total Backscatter Coefficient at 532 nm

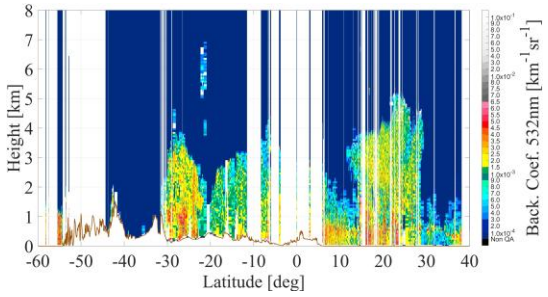

(f) Pure-dust Backscatter Coefficient at 532 nm

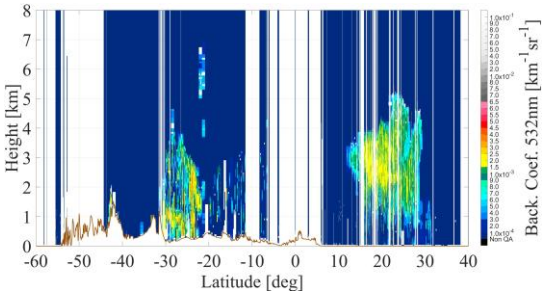

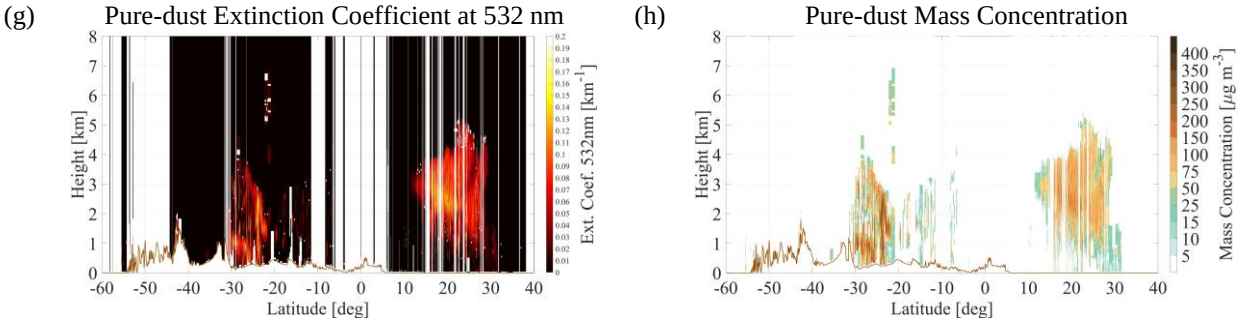

Figure 2: CALIPSO nighttime granule on the 12th of August 2012 (Fig. 2a), Feature-Type (Fig. 2b), Aerosol-Subtype (Fig. 2c), particulate depolarization ratio at 532nm (Fig. 2d), and total backscatter coefficient at 532nm (Fig. 2e), implemented towards the extracting the pure-dust atmospheric component in terms of backscatter coefficient at 532 nm (Fig. 2f), pure-dust extinction- coefficient at 532 nm (Fig. 2g), and pure-dust mass concentration (Fig. 2h).

A crucial step towards proper implementation of the one-step POLIPHON technique to CALIPSO L2 optical products at 532 nm with the objective to decouple the pure-dust and non-dust atmospheric components of the total aerosol load is the proper consideration of the $\delta_{\lambda,d}$ and $\delta_{\lambda,nd}$ parameters. With respect to $\delta_{\lambda,d}$, an increasing number of studies report particulate depolarization ratio measurements of dust-dominant aerosol layers around 0.31±0.04 at 532 nm (Sugimoto et al., 2003; Esselborn et al., 2009; Freudenthaler et al., 2009; Ansmann et al. 2011; Gross et al., 2011a; Wiegner et al., 2011; Mamouri et al., 2013; Baars et al., 2016; Hofer et al., 2017; Filioglou et al., 2020), corroborating on the assumption that the particulate depolarization ratio is a characteristic property of dust with little variability on a global scale. However, assumption on the $\delta_{\lambda,nd}$ requires consideration of the particulate depolarization ratio properties of the major non-dust tropospheric aerosol-subtype categories (i.e., marine, biomass burning smoke, pollen, volcanic ash). The sea salt aerosol category is in general characterized by particulate depolarization ratio values of the order of 2-3% at 532 nm, increasing however with decreasing Relative Humidity (RH) to values as high as 10-15% at 532 nm in the Marine Boundary Layer (MBL) – Free Troposphere entrainment zone (Haarinng et al., 2017a). The smoke aerosol category is in general characterized also by low particulate depolarization ratio values, of the order of 1-4% at 532 nm (Müller et al., 2007b; Nicolae et al., 2013). Significantly higher particulate depolarization ratio values are reported for pollen and volcanic ash, of the order of 4–15% and 30-40% at 532 nm, respectively (Ansmann et al., 2010; Gross et al., 2012; Noh et al.; 2013; Sicard et al., 2016; Shang et al., 2020; Bohlmann et al., 2021). However, pollen is usually confined within the Planetary Boundary Layer (PBL),), is characterized by high seasonality, and is observed in high concentrations at high latitudinal bands outside the domain of the study are, the dust belt, and the major dust transport pathways (Prospero et al., 2002). Volcanic ash emissions, despite the high intensity, are significantly less frequently observed than the dust, marine, smoke, and pollen aerosol categories. Thus, an average δ_{nd} effect of 0.05±0.02 at 532 nm is assumed for the broader non-dust aerosol-subtype class in the assumed external aerosol mixtures

(Marinou et al., 2017; Proestakis et al., 2024-). Following the consideration of the $\delta_{\lambda,d}$ and $\delta_{\lambda,nd}$ central parameters, the one-step POLIPHON technique allows decoupling of the pure-dust and non-dust components of an assumed external aerosol mixture, of particulate depolarization ratio lower than $\delta_{\lambda,d}$ and greater than $\delta_{\lambda,nd}$, while cases of $\delta_{\lambda,p}(z) \leq \delta_{\lambda,nd}(z)$ are considered dust-free and cases of $\delta_{\lambda,d}(z) \leq \delta_{\lambda,p}(z)$ are considered composed entirely of dust.

The one-step POLIPHON technique applied to CALIOP L2 optical products at 532 nm results to pure-dust backscatter coefficient profiles at 532nm ($\beta_{\lambda,d}(z)$) along the CALIPSO orbit-path, at uniform horizontal and vertical resolutions of 5 km and 60 m, respectively. Since CALIOP is an elastic backscatter lidar system, to convert the profiles of pure-dust backscatter coefficient at 532 nm (Fig. 2f) into profiles of pure-dust extinction coefficient at 532 nm (Fig. 2g), suitable pure-dust extinction-to-backscatter ratio (Lidar Ratio; LR) values are required (Eq. (2))

$$\alpha_{\lambda,d}(z) = LR_{\lambda,d} * \beta_{\lambda,d}(z) \quad (2)$$

The CALIPSO V4 algorithm assumes a universal LR of 44 sr at 532 nm for dust (Kim et al., 2018). However, recent studies report on the remarkable regional variability of dust LR at 532 nm (Floutsi et al., 2023). More specifically, the broader Atlantic Ocean is affected in the north mainly by intense loads of dust originating from the Saharan Desert (Prospero, 1999; Kanitz et al., 2014; Marinou et al., 2017; Gkikas et al., 2022) and in the south by dust emissions from the desert areas located in South Africa (Bryant et al., 2007) and South America (Gassó and Torres, 2019). Thus, this study applies suitable geographically-dependent dust LR at 532 nm values for the region of interest, towards the development of the atmospheric pure-dust product in terms of extinction coefficient at 532 nm. More specifically, in the domain of the north Atlantic Ocean Saharan dust outflow region a mean LR at 532 nm of 53.1-±-8 sr is used (Tesche et al., 2009; Gross et al., 2011a; Gross et al., 2011b, Tesche et al., 2011; Kanitz et al., 2013; Kanitz et al., 2014; Gross et al., 2015; Weinzierl et al., 2016; Haari~~n~~g et al., 2017b; Rittmeister et al., 2017; Bohlmann~~Bohlmann~~ et al., 2018; Floutsi et al., 2023), in the domain of South America a mean LR at 532 nm of 42 ±-17 sr is used (Kanitz et al., 2013), and the default CALIPSO V4 dust LR of 44 sr at 532 nm is used in the intermediate Atlantic Ocean region (Kim et al., 2018). ~~Finally~~As a next step, regionally-dependent ~~EARLINET-established~~ extinction coefficient at 532 nm (Fig. 2g) to mass concentration conversion factors (Ansmann et al., 2019) and typical particle density of ρ_d: 2.6 g cm^{-3} for dust (Ansmann et al., 2012) are applied towards establishing the final pure-dust mass concentration product (Fig. 2h) along the CALIPSO orbit-path (Eq. (3)). The climatologically representative extinction coefficient-to-mass concentration conversion factors, discussed in detail by Mamouri and Ansmann (2014, 2015, 2016, 2017) and Ansmann et al. (2019) were determined on the basis of

AERONET (Version 3; Level 2.0) long-term observations during atmospheric conditions characterized by dust presence (Ångström exponent <0.3 and AOT > 0.1), synergistically obtained with lidar-provided particle extinction coefficient profiles, allowing eventually provision of extinction-to-volume conversion factors $C_{v,d}$.

$$MC_d(z) = \rho \cdot c_{v,d} \cdot a_d(z) \quad (3)$$

Accordingly, a uniform spatial grid of 2° latitude by 5° longitude is established, for the Atlantic Ocean domain extending between ~~-~~60°S and 40°N. Iteration through all pure-dust mass concentration profiles within each 2°×5° deg^2 grids is performed, to establish for each grid seasonal-mean atmospheric profiles of quality-assured pure-dust mass concentration, grouped by seasons (December-January-February, DJF; March-April-May, MAM; June-July-August, JJA; and September-October-November, SON) and for the period 12/2006-11/2022. The final dataset provides ~~a four-dimensional (4D) reconstruction of~~the atmospheric dust conditions ~~the atmosphere,~~. Figure 3 provides the long-term annual-mean total backscatter coefficient at 532 nm (Fig. 3a), pure-dust backscatter coefficient at 532 nm (Fig. 3b), pure-dust extinction coefficient at 532 nm (Fig. 3c), and pure-dust mass concentration (Fig. 3d), with the later one subsequently implemented with spatial resolution 5°×2° deg^2 grids and temporal resolution of seasonal-mean, towards computation of the atmospheric pure-dust component deposited into the broader Atlantic Ocean. More specifically, the figure constitutes a three-dimensional reconstruction of the atmosphere in the geographical region confined between 100°W and 20°E longitude (x-axis) and 60°S and 40°N latitude (y-axis), and for the altitudinal range 0 to 8 km a.m.s.l (z-axis). Through utilizing parallel slices in the atmosphere for every 20° longitude, each figure provides insight into the three-dimensional total and dust atmospheric aerosol components, in terms of total backscatter coefficient at 532 nm (Fig. 3a), and for the dust component of the total aerosol load in terms of backscatter coefficient at 532 nm (Fig. 3b), extinction coefficient at 532 nm (Fig. 3c), and mass concentration (Fig. 3d), over the broader region covering South America (lower left corner of figures), part of North America (upper left corner of figures), Central-Western Africa (right side of figures), and the broader Atlantic Ocean confined in-between. The state of the atmospheric aerosol load in figure 3 is provided in terms of annual mean EO-based products computed for the period 12/2006-11/2022, to provide visualization of the long-term mean atmospheric dust transport pattern over the region of interest. ~~as shown in Figure 3, in terms of annual mean total backscatter coefficient at 532 nm (Fig. 3a), pure dust backscatter coefficient at 532 nm (Fig. 3b), pure dust extinction coefficient at 532 nm (Fig. 3c), and pure dust mass concentration (Fig. 3d), with the later one subsequently implemented towards computation of the atmospheric pure dust component deposited into the broader Atlantic Ocean.~~

(a) Total Backscatter Coefficient at 532 nm (b) Pure-dust Backscatter Coefficient at 532 nm

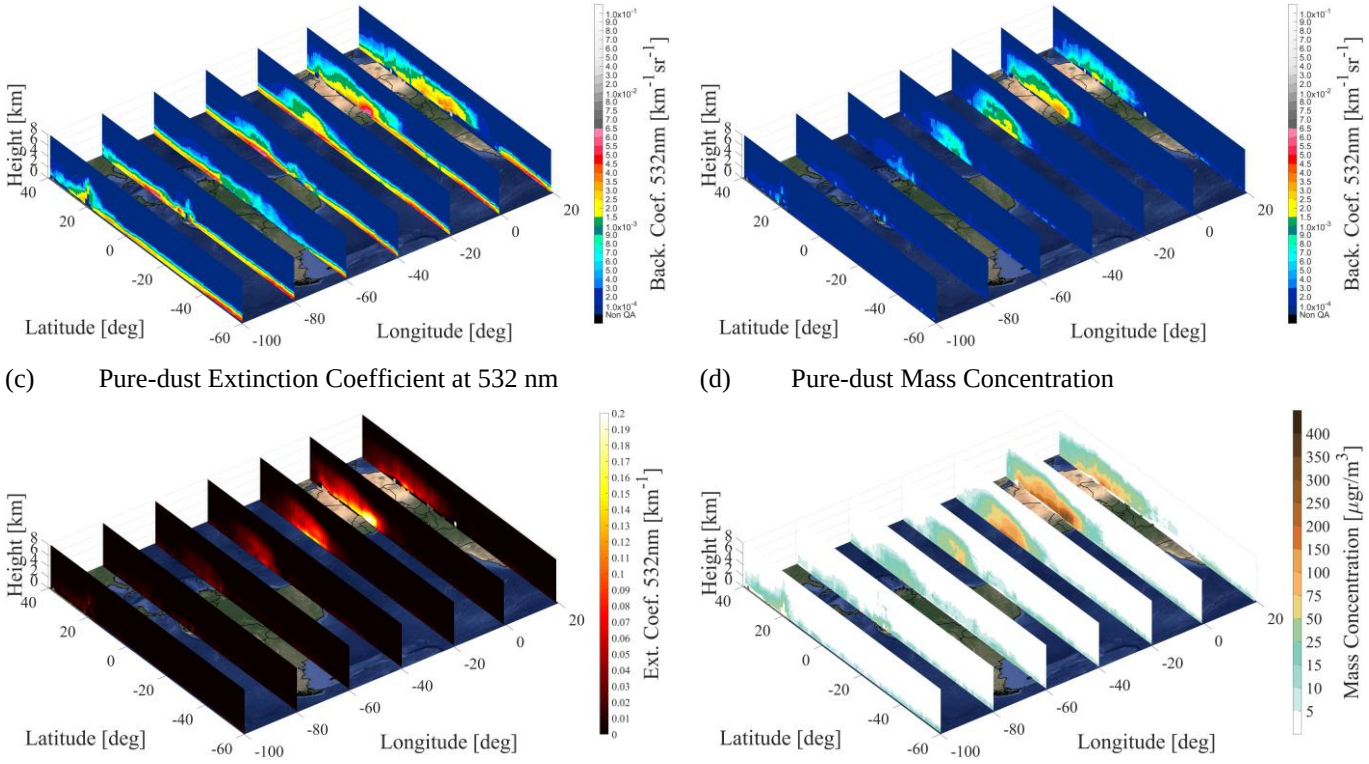

(c) Pure-dust Extinction Coefficient at 532 nm (d) Pure-dust Mass Concentration

Figure 3: Annual-mean ~~four~~three-dimensional (~~4D~~3D) reconstruction of the atmosphere in terms of total backscatter coefficient at 532 nm (Fig. 3a), pure-dust backscatter coefficient at 532 nm (Fig. 3b), pure-dust extinction coefficient at 532 nm (Fig. 3c), and pure-dust mass concentration (Fig. 3d) ~~in 1°×1° spatial resolution and~~based on the ~~for the~~ period 12/2006-11/2022.

Uncertainties in the retrieval of atmospheric dust properties (i.e., backscatter coefficient, extinction coefficient, and mass concentration) originate from multiple sources, primarily (a) the uncertainties in the CALIPSO L2 optical products and aerosol classification flags, (b) the methodology applied towards atmospheric dust decoupling from the total aerosol load, and (c) the assumed constants and conversion factors (i.e., LRs and extinction-to-mass conversion parameters) (Marinou et al., 2017; Proestakis et al., 2018; 2024). CALIPSO L2 retrieval uncertainties, particularly in backscatter coefficient and particulate depolarization ratio at 532 nm, are assumed to be random and uncorrelated (Vaughan et al., 2009; Winker et al., 2009), yet can be significant; particulate depolarization ratio uncertainties often exceed 100%, and the limitations in aerosol subtype classification introduce further biases, especially for mixed or tenuous layers. The aerosol subtype classification algorithm (Omar et al., 2009; Kim et al., 2018) may result in positive or negative biases depending on feature type misclassification, with particularly low accuracy (~35%) in identifying polluted dust layers (Burton et al., 2013). Moreover, CALIOP's limited sensitivity to optically thin layers (Kacenelenbogen et al., 2011; Rogers et al., 2014) leads to systematic underestimation of

AOD, with negative biases of ~0.02 (nighttime) and <0.1 (daytime), primarily due to its detection sensitivity (Toth et al., 2018). The application of dust decoupling methodologies (Shimizu et al., 2004; Tesche et al., 2009; 2011; Ansmann et al., 2019) introduces additional uncertainties, with the depolarization-based separation approach contributing 5%–10% uncertainty during strong dust events and up to 20%–30% in less pronounced cases, primarily linked to variability in assumed dust depolarization ratios (Tesche et al., 2009, 2011; Ansmann et al., 2012; Mamouri et al., 2013). The conversion of decoupled backscatter profiles to extinction coefficients using regional LRs introduces relative uncertainties on the order of 15%–25%, while the final conversion to dust mass concentration profiles introduces further uncertainties of approximately 10%–15% (Tesche et al., 2009; Amiridis et al., 2013; Marinou et al., 2017; Proestakis et al., 2024). Cumulatively, uncertainties propagate and increase with each processing step, resulting in total uncertainties that can reach 10%–30% in backscatter coefficient, 15%–50% in extinction coefficient, and 20%–60% in mass concentration for ground-based lidar observations (Mamouri and Ansmann, 2017; Ansmann et al., 2019). However, in the case of CALIPSO-based retrievals, where the dominant uncertainty sources are the backscatter and depolarization ratio inputs, frequently of the same order of magnitude or even higher than the optical products, total uncertainties in mass concentration retrievals can escalate to as high as 100%–150%, underscoring the challenge of achieving high precision in satellite-based dust mass estimates (Marinou et al., 2017; Proestakis et al., 2018; 2024).

2.2.2 Extracting the atmospheric pure-dust component deposited into the Atlantic Ocean

The present section aims to capitalize on the established ~~4D~~ four-dimensional reconstruction of the pure-dust atmospheric component in terms of mass concentration profiles, based on ERA5 zonal (U) and meridional (V) wind components, to extract a multiyear satellite-based estimation of the atmospheric pure-dust component deposited into the broader Atlantic Ocean, following the approach suggested by Yu et al. (2019). The estimation of pure-dust deposition fluxes is realized through several successive discrete steps, as visualized in Figure 4 for the indicative grid case extending between 20° and 22° latitude and -30° and -25° longitude of JJA 2020.

The first step accounts for the different vertical resolutions of the established LIVAS atmospheric pure-dust aerosol product and ERA5 horizontal wind components. More specifically, the pure-dust mass concentration atmospheric product follows the original high vertical resolution of CALIPSO of 60 m and 180 m resolution for the altitude range of −0.5-20.2 km and 20.2-30 km a.m.s.l., respectively (Sect. 2.1.1), while the ERA5 U and V wind components are provided in 37 pressure levels between 1000 hPa and 1 hPa, converted to height above mean sea level (Sect. 2.1.2). Thus, the first step performs a reconstruction of the LIVAS pure-dust mass concentration product, from the higher vertical resolution of CALIPSO (Fig. 4a) to the lower vertical resolution of ERA5 (Fig. 4c). ~~However, t~~The zonal and meridional atmospheric dust transport and the seasonal transition of atmospheric transport pathways highly depend on meteorological conditions (Prospero et al., 1987), including among others, the wind patterns (Fig. 4b). Thus, the second step accounts for decoupling the pure-dust mass concentration atmospheric product into the zonal (eastward and westward) and meridional (northwards and southward) transported components, on the basis of the (1) magnitude and (2) direction of ERA5 U and V horizontal wind components (Fig. 4c). The

third step, on the basis of (1) the zonal and meridional atmospheric transport components of pure-dust and (2) the U and V wind vector profiles from ERA5 (Fig. 4c), provides the fluxes of pure-dust both in the zonal and meridional directions (Fig. 4d). –More specifically, the mass flux (μg m^{-2} s^{-1}) is computed as the amount of mass transported per unit time (s) across a unit area (m^2) that is perpendicular to the direction of mass transport, thus in the conceptual approach adopted in the framework of the study in meridional and zonal directions, through the implementation of ERA5 U and V wind fields, respectively. The mass fluxes are computed on a seasonal basis, meaning based on seasonal-mean atmospheric dust profiles (Fig. 4a) and seasonal-mean profiles of ERA5 zonal and meridional wind components (Fig. 4c).

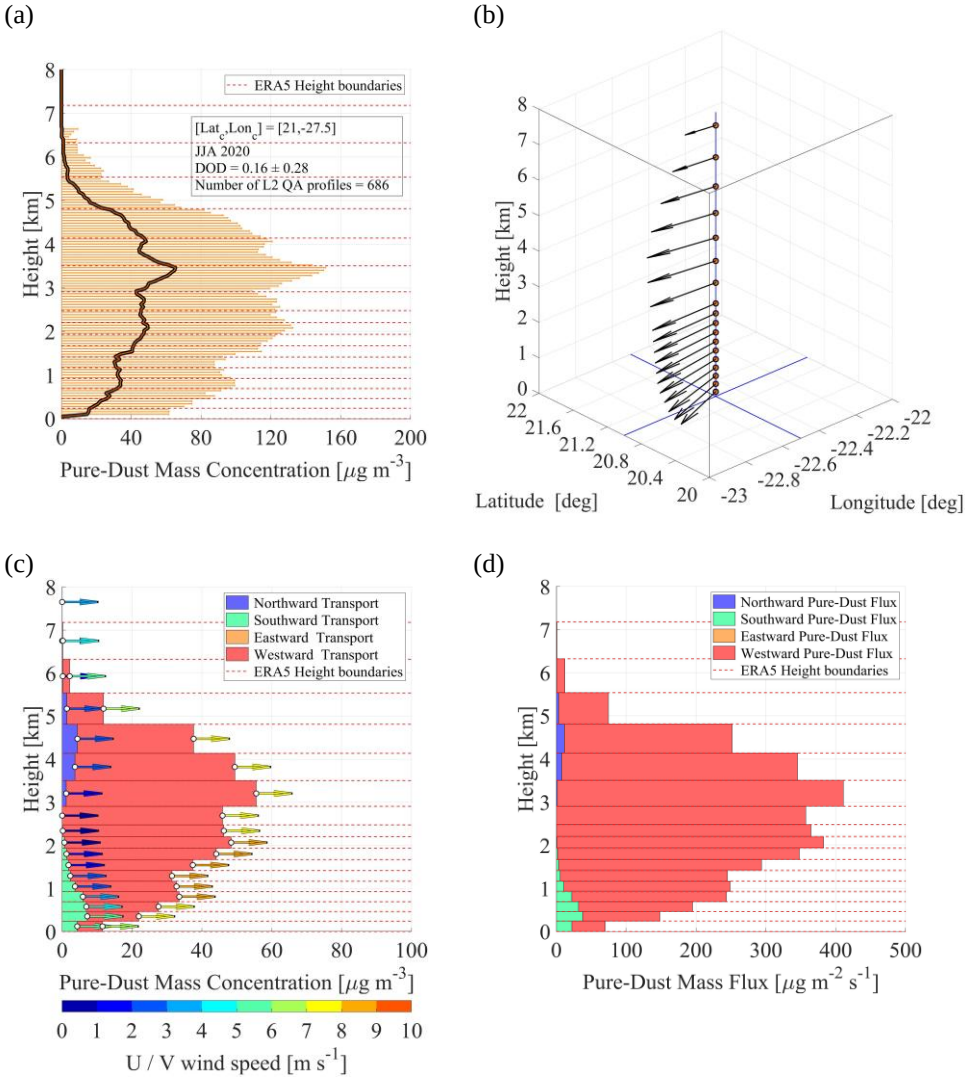

Figure 4: Illustration case of the followed methodology toward the estimation of pure-dust mass fluxes in the zonal and meridional directions for the Atlantic Ocean area extending between 20° and 22° latitude and -30° and -25° longitude and for JJA 2020. From top-left to bottom-right: the ESA-LIVAS mass-concentration pure-dust aerosol product (Fig. 4a), the ERA5 U and V profiles of wind (Fig. 4b), the profile of pure-dust mass concentration decoupled into zonal and meridional atmospheric transport components (Fig. 4c), and the pure-dust mass fluxes in the zonal and meridional directions (Fig. 4d). In Fig. 4c the horizontal arrows indicates the wind speed, according to the colorbar, and the different colours in the legend indicate the dust transport direction.

As a next step, a three-dimensional (3D) closed cuboid surface is assumed, of 5° length (zonal), 2° width (meridional), and 10 km height (vertical), with the base surface at 0 km a.m.s.l. The approach to extract the atmospheric dust component deposited into the Atlantic Ocean is based on the condition that the net input-output mass flux through a Gaussian surface, without dust sources or sinks present in the enclosed volume, should equal zero. Towards this condition, we assume no output or input dust fluxes from the top surface area of the cuboid, and in general -climatologically- no presence of atmospheric dust at heights beyond 10 km a.m.s.l. (Marinou et al., 2017), a hypothesis supported by the CALIPSO-based climatology over the region of interest (not shown). Moreover, we assume no dust sources over the Atlantic Ocean domain, thus no dust input flux from the surface area of the cuboid. To support this assumption the Clouds and Earth's Radiant Energy System (CERES) International Geosphere–Biosphere Programme (IGBP) comprehensive map land classification is implemented (Schneider et al., 2013), and more specifically we consider as Atlantic Ocean grids only surface areas within the domain of interest classified as at least ~~50~~25% covered by “Water Bodies” and no more than 10% classified as “Closed Shrublands”, “Open Shrublands”, or “Bare Soid and Rocks”. Accordingly, the input and output pure-dust mass flow rates from-and-towards all neighbouring ~~3D~~ three-dimensional cuboids through all neighbouring zonal and meridional surfaces are calculated. The total mass flow rates ($\mu g\ s^{-1}$) across the meridional and zonal directions are computed, through the consideration of the mass fluxes and the total surface areas of the conceptual cuboid that atmospheric dust is transported through. Following the conservation of mass and the aforementioned assumptions, the dust flow rate and accordingly the dust flux through the base of the conceptual cuboid column, corresponding to the deposited dust, is derived by subtracting from all input components all output components. The conceptual approach towards the estimating the atmospheric deposited dust component is illustrated in Figure 5, for the Atlantic Ocean area extending between 20° and 22° latitude and -30° and -25° longitude and for JJA 2020, yielding dust deposition rate in this case of 192.8 mg~~/~~ m^{-2} d^{-1}.

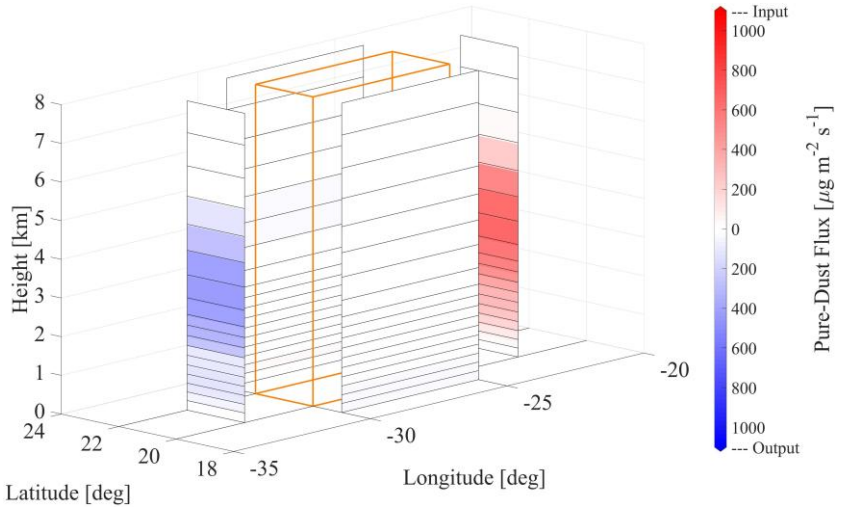

Figure 5: Illustration of the conceptual approach applied towards extracting the pure-dust atmospheric component deposited in the Atlantic Ocean, for the area extending between 20° and 22° latitude and -30° and -25° longitude and for JJA 2020.

The method provides the amount of dust deposited into the ocean based on the estimation of the pure-dust aerosol atmospheric component, however recurrently may result in not physical, either negative or extremely high, values of dust deposition rate. More specifically, the atmospheric dust component deposited into the Atlantic Ocean (Fig. 5) is determined by differentiation of zonal and meridional seasonal-mean profiles of pure-dust mass flow rates from ESA-LIVAS pure-dust climate data record (Fig. 4), and thus the applied method is sensitive to CALIPSO orbital characteristics and CALIOP inherited limitations. Factors that may contaminate the ~~4D~~ four-dimensional atmospheric dust product and subsequently result to not physical retrievals of the dust deposition rate along the dust transport pathways include (1) clouds misclassified as aerosols in terms of feature type classification and dust layers misclassified as non-dust layers and vice versa in terms of aerosol subtype classification, (2) weighting effects resulting from complete attenuation of CALIOP lidar signal due to the presence of optically opaque atmospheric layers and underestimations due to the presence of tenuous and defuse atmospheric layers of signal-to-noise ratio (SNR) below the minimum detection threshold of CALIOP, and (3) high variability in sampling frequency of QA L2 profiles due to CALIPSO revisit frequency over specific grid areas and cloud-coverage variability. To account for dust deposition rate negative values, indicating the ocean surface would act as emission source of dust, values lower than zero are masked as not physical. In addition, to account for unrealistic values of dust deposition rate over areas residing outside the documented atmospheric dust transport pathways (Prospero, 1999; Prospero, 2002; Kanitz et al., 2014; Marinou et al., 2017; Gassó and Torres, 2019; Gkikas et al., 2022), grids of virtually non-presence of dust on a seasonal-mean temporal resolution (DOD at 532 nm $\leq$ 0.01) are considered most probably contaminated by clouds misclassified as aerosols in terms of feature type classification and/or by non-dust layers misclassified as dust layers in terms of aerosol subtype classification (Burton et al., 2013; Haari~~n~~g et al., 2017a), and thus not contributing to dust deposited into the ocean. Finally, in order to reduce noise in the

final grid, a 3×3 uniform filter is applied, which applies a moving window over the data replacing dust deposition rate values with the mean of the dust deposition rate values inside the moving window.

3 Results and Discussion

3.1 Atmospheric Dust and Dust Deposition

~~**3 Atmospheric Dust and Dust Deposition**~~

The present section aims to capitalize on the performed developments ~~towards~~ resulting to decoupling the atmospheric pure-dust component from the total aerosol load (Sect.2.2.1.) and to extracting the atmospheric pure-dust component deposited into the Atlantic Ocean (Sect.2.2.2.) to provide (i) a comprehensive reconstruction of the atmospheric dust aerosol component and (ii) quantification of the atmospheric dust aerosol component deposited into the Atlantic Ocean. The products are generated over the broader Atlantic Ocean, encompassing the dust emission sources of W~~.~~ est Africa and S~~.~~ outh America, the Atlantic Ocean, the Caribbean Sea, and the Gulf of Mexico ~~regions~~, confined between latitudes 40°N to 60°S and of 5° (zonal) x 2° (meridional) spatial resolution, in a seasonal-mean temporal resolution, and of temporal coverage between 12/2006 and 11/2022. Figure 6 provides the annual- and seasonal-~~-~~mean horizontal distributions of the pure-dust atmospheric aerosol component (Fig.6-left column) and the corresponding pure-dust component deposited into the ocean along the trans-Atlantic transport (Fig.6-right column).

The pure-dust atmospheric aerosol load is shown in terms of ~~Dust Optical Depth (~~DOD~~)~~ at 532 nm (Fig.6-left column), computed through vertical integration of the L2 annual-mean and seasonal-mean quality-assured pure-dust extinction coefficient profiles at 532 nm within each grid of spatial resolution 2°×5°, providing the columnar pure-dust atmospheric load under cloud-free sky conditions. The standard deviation of the annual-mean and seasonal-mean of the EO-based products is in addition computed, both for atmospheric dust and dust deposition, providing a metric of the spread of dispersion and variability within each grid of spatial resolution 2°×5°. It should be noted that the variability within each grid is usually large, driven by the large variability of the episodic nature of dust events, highly heterogeneous in both space and time, the large variability in the strength of the emission, atmospheric transport, ~~and~~ the removal processes, and the variability of meteorological conditions (Prospero et al., 1987).

Overall, the horizontal distributions of DOD at 532 nm reveal similar patterns, although the magnitude of atmospheric dust load is characterized by high interannual, spatial, and temporal variability, both over land and ocean. Over land, arid regions of little vegetation and of easily erodible soils contributing to the dust life circle and encompassing the broader Atlantic Ocean include the western Saharan Desert in North Africa (Prospero et al., 2002; Huneuus et al., 2011; Marinou et al., 2017, Gkikas et al., 2022), the Etosha Pan (Namibia), Makgadikgadi Pan (Botswana), Kalahari Desert (Namibia, Botswana, South Africa)

and Namib Desert (Angola and Namibia) in South Africa (Bryant et al., 2007; Vickery et al., 2013; Gkikas et al., 2022), and the Patagonia Desert (Rio Negro and Chubut provinces) in South America (Gassó and Torres, 2019; Gkikas et al., 2022).

Over the western Saharan Desert persistent intense loads of dust aerosol are observed throughout the year, dust emissions that are considered of both anthropogenic and natural origin (Ginoux et al., 2012). Dust emission mechanisms of anthropogenic origin include processing of soils through agricultural activities, such as cultivation and overgrazing (Ginoux et al., 2012). Natural dust emission micro-scale to synoptic-scale mobilization mechanisms, favoured by the development of the Saharan heat low (SHL; Schepanski et al., 2017), include pressure gradients (Tyson et al., 1996; Klose et al., 2010), dust devils (Koch and Renno, 2005), "haboobs" (Knippertz et al., 2007; Ansmann et al., 2009b; 2011), and low-level jets (LLJ; Fiedler et al., 2013). Though inhomogeneous in time, space, and of variable strength (Knippertz et al., 2009, 2011), the emission mechanisms over the western Saharan Desert trigger uplift and accumulation in the atmosphere of several million tonnes of mineral dust each year (Kok et al., 2023). In terms of DOD at 532 nm, on a seasonal-mean basis, and following the annual cycle of dust source activation (Washington et al., 2009), less pronounced dust activity is apparent during DJF (0.159 ± 0.119; Fig. 6c) and higher dust activity during JJA (0.341 ± 0.182; Fig. 6g), with intermediate observed DOD values during SON (0.174 ± 0.066; Fig. 6i) and MAM (0.325 ± 0.133; Fig. 6e).

In South Africa, the observed dust activity over the arid areas is characterized by high spatial and temporal variability, however of lower dust emission strength compared to North Africa arid areas. Activation of the dust sources of Etosha and Makgadikgadi pans is mostly related to lakes' inundation, resulting to high seasonal variability in dust emission strength (Gkikas et al., 2022), while over the Namib Desert and along the broader Namibian coastline, dust emission activity is mainly related to frequent berg winds (katabatic winds) blowing from inland Plateaus and towards the Atlantic Ocean, resulting to low intra-annual variability in dust emission strength throughout the year (Eckardt and Kuring, 2005). Dust activity over the dust source regions of this area is more pronounced primarily during SON (DOD at 532 nm of 0.011 ± 0.007; Fig. 6i), secondarily during JJA (DOD at 532 nm of 0.008 ± 0.003; Fig. 6g) and DJF (DOD at 532 nm of 0.008 ± 0.004; Fig. 6c), and of significantly lower dust activity during MAM (DOD at 532 nm of 0.005 ± 0.002; Fig. 6e). The observed annual-mean DOD at 532 nm is computed at 0.008 ± 0.019 (Fig. 6a).

In South America and the Patagonian Desert, higher strength in dust emissions is observed over the broader arid area extending between the river basins of Rio Negro and Chubut provinces and the southern end of the desert (McConnell, et al., 2007; Mazzonia and Vazquez, 2009). Over this area, annual-mean DOD of 0.014 ± 0.024 (Fig. 6a) are observed. With respect to seasonal dust activity, higher DOD values are recorded during SON (0.017 ± 0.008; Fig. 6i) and DJF (0.014 ± 0.004; Fig. 6c) and lower during JJA (0.013 ± 0.008; Fig. 6g) and MAM (0.009 ± 0.003; Fig. 6e).

The export of dust layers entrained into the atmosphere and transport across the broader Atlantic Ocean is largely controlled by the prevailing wind systems and the regional meteorology, shaping the major dust transport pathways (Adams et al., 2012; Ben-Ami et al., 2012; Amiridis et al., 2013; Marinou et al., 2017; ~~H.~~ Yu et al., 2015b; Proestakis et al., 2024). In the northern hemisphere, the westwards atmospheric transport of Saharan dust layers is largely modulated by the seasonal latitudinal migration of the Intertropical Convergence Zone (ITCZ; Schneider et al., 2014). More specifically, during boreal summer

(JJA), the enhanced cyclonic circulation of the Saharan Heat Low (SHL; Schepanski et al., 2017), positioned between the Hoggar Massif and Atlas Mountains (Lavaysse et al., 2009), increase the strength of the northeasterly Harmattan winds to the west (Lavaysse et al., 2009; Parker et al., 2005a) and of the south-westerly African monsoon flow to the east (Parker et al., 2005b), and vice versa (Schepanski et al., 2017). The increased pressure gradients of the SHL affect the position of the African Easterly Jet (AEJ; Knippertz and Todd, 2012) and the development of the African Easterly Waves (AEW; Jones et al. 2003), modulating the large-scale circulation systems over North Africa and determining the ITCZ position along the 10°-20°N route (Fig. 6g), and in addition enhance dust emission and export towards and over the Atlantic Ocean (Schepanski et al., 2009; Doherty et al., ~~2012~~2014). Exported within the Saharan Air Layer (SAL; Carlson and Prospero 1972; Prospero and Carlson, 1981; Braun 2010; Dunion 2011; Adams et al. 2012; Schepanski et al., 2009; Weinzierl et al., 2016; Rittmeister et al., 2017), the major transport highway for dust layers across the northern Atlantic Ocean, dust plumes during boreal summer are frequently transported as far as the Caribbean Basin and the coast of North America (Prospero, 1999; Prospero et al., 2014; ~~Van~~ van der Does et al., 2018). In the winter season (DJF), the decreasing depth and extent of the SHL and the migration of the center of the cyclonic system southwest of the Hoggar Massif (Schepanski et al., 2017) result in generally lower levels of DOD (Fig. 6c). ~~Moreover, d~~During the winter season, the strong Harmattan winds export plumes of dust south-westward over the Gulf of Guinea (Engelstaedter et al., 2006), mainly within the Marine Boundary Layer and the lower Troposphere (0-3 km a.m.s.l.) (Adams et al., 2012; Stuut et al., 2005; Tsamalis et al., 2013), where the dust plumes are transported westwards, mainly between the equator and 10°N, reaching as far as the Amazon Basin in South America (Huang et al., 2010; Prospero et al., 2014; Yu et al., 2015a). During the intermediate seasons of spring (MAM) and autumn (SON), following the seasonal northward and southward migration of the ITCZ respectively, dust plumes of intermediate depth and intensity between winter and summer are transported along the 5°-15°N latitudinal band across the North Atlantic Ocean (Fig. 6e/i).

In the southern hemisphere and in the case of dust plumes originating from the arid areas of South Africa (Eckardt and Kuring, 2005; Bryant et al., 2007; Ginoux et al., 2012; Vickery et al., 2013; Gkikas et al., 2022), barotropic easterly waves forming between continental high-pressure systems and the South Atlantic anticyclonic systems (Tyson et al., 1996) result in westwards export and transport of short-range and short-lived dust layers (Vickery et al., 2013) across the southern Atlantic Ocean (Gkikas et al., 2022), mainly below 600 hPa and primarily in the latitudinal zone extending between 20°S and 10°S. In contrast, the relatively-weak dust plumes (Fig. 6a) (Foth et al., 2019) originating from the arid areas of South America (McConnell et al., 2007; Mazzonia and Vazquez, 2009; Ginoux et al., 2012), under favourable meteorological conditions related to strong easterly winds (Gassó et al., 2010; Gassó and Torres, 2019) are frequently advected over the South Atlantic Ocean, primarily in the latitudinal zone extending between 50°S and 20°S, where subject to long-range aeolian transport the dust layers may reach as far as 20°W (Fig. 6b). Finally, it should be noted that the presence of low DOD values over the area extending below South Africa and to the east of 5°W (Fig. 6a) most probably results from the extended cloud coverage over the region (Gassó and Torres, 2019) and the presence of cubic-like sea salt emissions in the Marine Boundary Layer – Free Troposphere entrainment zone (Haari~~n~~g et al., 2017a) classified as dust-mixtures due to the increased depolarizing properties in CALIPSO aerosol-

subtype classification scheme (Kim et al., 2018), possible resulting to contaminating effects of the atmospheric dust dataset in this case.

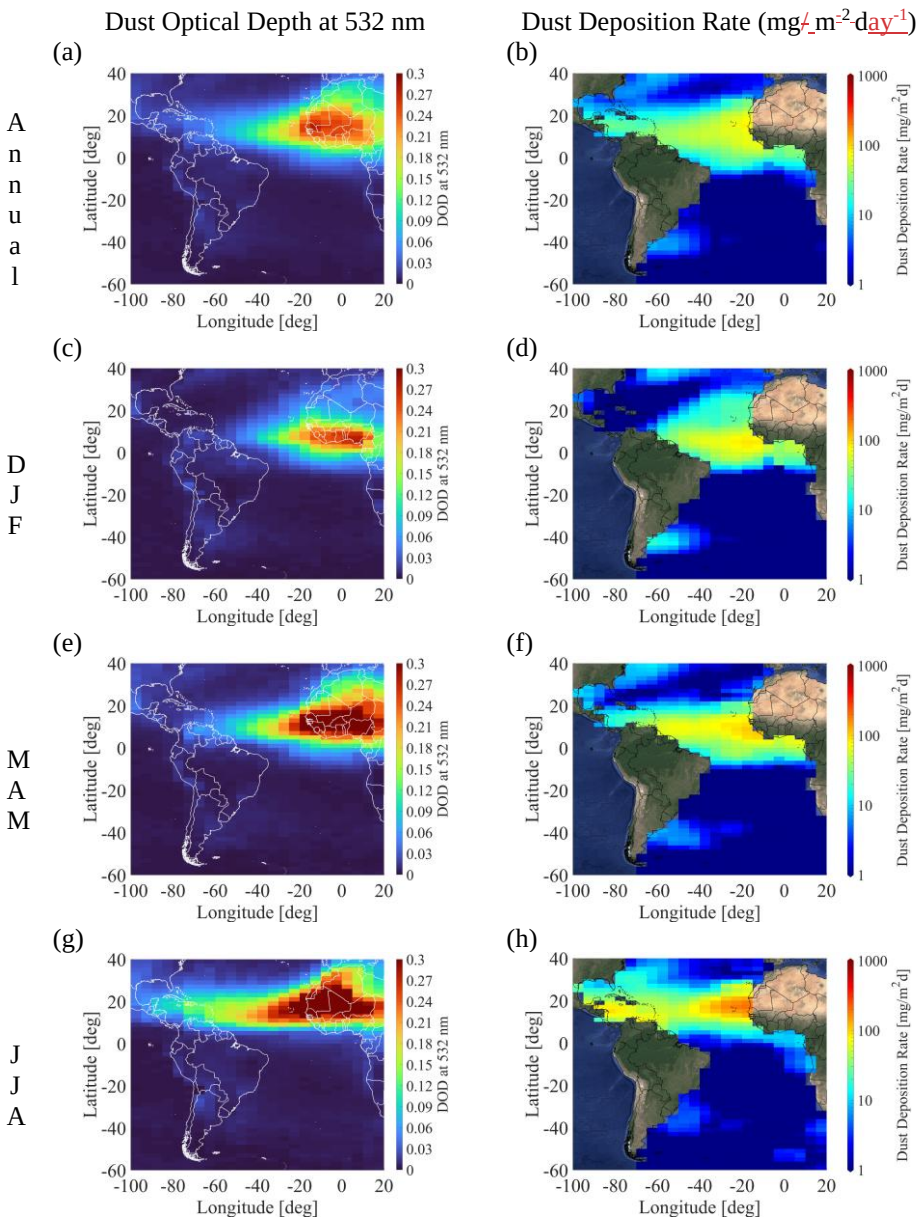

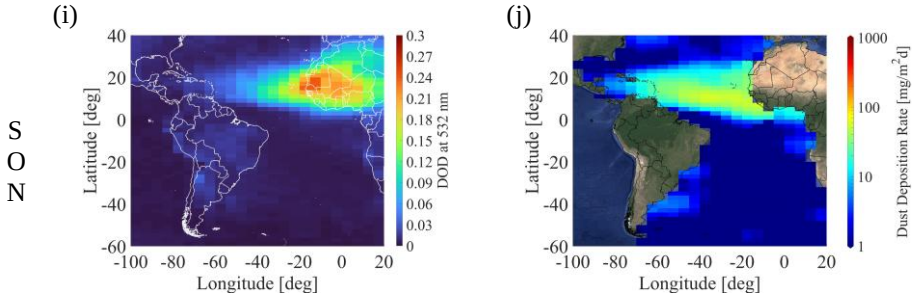

Figure 6: LIVAS Dust Optical Depth at 532 nm (DOD; left column) and Dust Deposition Rate (DDR; right column), provided in annual-mean (a and b), DJF (c and d), MAM (e and f), JJA (g and h), and SON (i and j), estimated for the period 12/2006-11/2022.

The annual and seasonal variations of dust deposition rate (DDR; unit: mg~~·~~ m^{-2}~~·~~ day^{-1}) into the broader Atlantic Ocean, as derived by differentiation of the zonal and meridional pure-dust input/output mass flow rates of the atmospheric pure-dust aerosol component and on the basis of the mass conservation hypothesis (Sect. 2.2.2), are provided in Figure 6-right column. In general, as expected, there is a strong seasonality in dust deposition, with higher estimates of dust deposition rate revealed mainly during the hot seasons of the year and in the proximity of the major arid areas encompassing the broader Atlantic Ocean domain, decreasing with increasing distance from the dust emission sources, subject to both dry and wet deposition (Schepanski et al., 2009; Adler et al., 2018; ~~Van~~ van der Does et al., 2020). More specifically, the observed spatial and temporal patterns of DDR (Fig. 6-right column) follow the seasonal shifts of the major trans-Atlantic dust transport pathways, both in terms of extent and intensity, as shown and discussed in terms of DOD at 532 nm (Fig. 6-left column). It should be emphasized though that DDR and DOD spatiotemporal-patterns are not directly compatible, since DDR depends not only on the three-dimensional structure of atmospheric dust and the horizontal components of the wind profiles, but more importantly, on the zonal and meridional divergence of the dust mass fluxes. Hence, higher DDR values are apparent over areas not necessarily characterized by higher DOD values but over areas where the meridional and zonal gradients towards downwind adjusted areas are larger.

In the northern hemisphere (Table 3; Figure 7), dust deposition is largely modulated by the seasonal migration of the ITCZ (Schneider et al., 2014). In the winter and spring seasons, when the Saharan Desert Harmattan northeasterly trade-winds are stronger (Lavaysse et al., 2009; Parker et al., 2005a) and the trans-Atlantic dust transport route follows the latitudinal migration of ITCZ to the south of 10°N and 15°N respectively (Fig.6c/e), considerable amounts of dust are transported towards and over the Gulf of Guinea (Lons: 10°W-15°E / Lats: 6°S-6°N). In this case, removal of dust particles from the atmosphere is largely controlled by intense rainfall (Schepanski et al., 2009), resulting, mainly through wet deposition, in estimated DDR values as high as 37.24 ~~-~~±~~-~~8.36 mg~~·~~ m^{-2}~~·~~ day^{-1} (Fig. 6d) and 46.49 ~~-~~±~~-~~15.49 mg m^{-2} day^{-1}~~mg·m^{-2}·day^{-1}~~ (Fig. 6f), for DJF and MAM respectively. In the summer and autumn seasons, intersection of the weaken Saharan northeasterly and of the amplified

Southern Africa southeasterly export pathways over the Gulf of Guinea, result to estimated DDR values as high as 8.09 -± 2.59 mg m^{-2} day^{-1}~~mg·m^{-2}·day^{-1}~~ (Fig. 6h) and 8.77 -± -5.61 mg m^{-2} day^{-1}~~mg·m^{-2}·day^{-1}~~ (Fig. 6j), respectively. To the north of the Gulf of Guinea, in the proximity of the western coast of North Africa - Saharan Desert, high presence of dust is apparent throughout the year, which results in significant amounts of dust deposited into the domain of North-East Atlantic Ocean (Lons: 30°W-10°W / Lats: 10°S-40°N). The fluxes of dust deposition show a maximum of 37.94 -± -55.99 mg m^{-2} day^{-1}~~mg·m^{-2}·day^{-1}~~ in summer (Fig. 6h) and a minimum of 17.42 -± -17.91 mg m^{-2} day^{-1}~~mg·m^{-2}·day^{-1}~~ in autumn (Fig. 6j), while during spring (Fig. 6f) and winter (Fig. 6d) seasons intermediate values of 34.01 -± -34.05 mg m^{-2} day^{-1}~~mg·m^{-2}·day^{-1}~~ and 31.96 -± 27.03 mg m^{-2} day^{-1}~~mg·m^{-2}·day^{-1}~~, respectively, are observed. Moving further west, in the middle of the tropical Atlantic Ocean (Lons: 60°W-30°W / Lats: 10°S-40°N), relatively high values of DDR also appear, subject to long-range atmospheric transport of dust (Weinzierl et al., 2016; van der Does et al., 2018; Drakaki et al., 2022) mainly within the SAL (Carlson and Prospero 1972; Prospero and Carlson, 1981; Braun 2010; Dunion 2011; Adams et al. 2012; Schepanski et al., 2009). More specifically, estimated dust deposition fluxes over the NMAO area equal 19.46 -± -18.41 mg m^{-2} day^{-1}~~mg·m^{-2}·day^{-1}~~ in winter (Fig. 6d), 23.16 -± -24.97 mg m^{-2} day^{-1}~~mg·m^{-2}·day^{-1}~~ in spring (Fig. 6f), 24.04 -± -29.31 mg m^{-2} day^{-1}~~mg·m^{-2}·day^{-1}~~ in summer (Fig. 6h), and 14.29 -± -16.31 mg m^{-2} day^{-1}~~mg·m^{-2}·day^{-1}~~ in autumn (Fig. 6j). With respect to the North-West Atlantic Ocean area (Lons: 100°W-60°W / Lats: 10°N-40°N), during summer relatively high dust deposition fluxes are observed mainly in the Caribbean Sea - Southern United States - Gulf of Mexico area, with DDR values as high as 31.67 -± -23.85 mg m^{-2} day^{-1}~~mg·m^{-2}·day^{-1}~~ (Fig. 6h). However, following the seasonal northward and southward migration of the ITCZ and the weaker export of Saharan dust into the SAL (Schepanski et al., 2017) during spring and autumn seasons, significantly lower values of DDR are observed, equalling 8.77 -± -7.88 mg m^{-2} day^{-1}~~mg·m^{-2}·day^{-1}~~ (Fig. 6f) and 4.74 -± -5.74 mg m^{-2} day^{-1}~~mg·m^{-2}·day^{-1}~~ (Fig. 6j), respectively, ~~and~~ reaching a minimum of 1.31-±-2.19 mg m^{-2} day^{-1} in winter (Fig. 6d). However, despite the relatively low amounts of dust reaching the east coast of South America or even beyond over the mainland (Huang et al., 2010; Prospero et al., 2014; Yu et al., 2015a), several studies report on the vital role of the dust-related deposited nutrients (i.e., nitrogen, phosphorus, silica, and iron) to the sustainability of the Amazon rainforest (Koren et al., 2006; Tegen et al., 2006; Ansmann et al., 2009a; Ben-Ami et al., 2010; Abouchami et al., 2013; Gläser et al., 2015).

In the southern hemisphere (Table 3; Figure 7), the amount of dust deposited into the broader south Atlantic Ocean is significantly lower compared to the northern hemisphere. More specifically, the ~~relatively weak~~ dust plumes (Fig. 6a) (Foth et al., 2019) originating from the arid areas of South America (McConnell et al., 2007; Mazzonia and Vazquez, 2009; Ginoux et al., 2012) advected over the ~~South West~~ Atlantic Ocean (Lons: 65°W-35°W / Lats: 50°S-22°S), result in dust deposition fluxes over the southwest Atlantic Ocean area of 3.79 -± -4.02 mg m^{-2} day^{-1}~~mg·m^{-2}·day^{-1}~~ in winter (Fig. 6d), 2.97 -± -2.26 mg m^{-2} day^{-1}~~mg·m^{-2}·day^{-1}~~ in spring (Fig. 6f), 2.17 -± -1.38 mg m^{-2} day^{-1}~~mg·m^{-2}·day^{-1}~~ in summer (Fig. 6h), and 1.41 -± -2.32 mg m^{-2} day^{-1}~~mg·m^{-2}·day^{-1}~~ in fall (Fig. 6j). With respect to dust plumes originating from the arid areas of South Africa (Eckardt and Kuring, 2005; Bryant et al., 2007; Ginoux et al., 2012; Vickery et al., 2013; Gkikas et al., 2022) (Lons: 10°W-15°E / Lats: 14°S-6°S), the westwards export and transport of short-range and short-lived dust layers (Vickery et al., 2013) across the southern Atlantic Ocean (Gkikas et al., 2022) result in relatively low values of dust deposition fluxes, equalling 3.14 -± -3.59

mg m^{-2} day^{-1}~~mg·m^{-2}·day^{-1}~~ in winter (Fig. 6d), 2.61 ± 2.21 mg m^{-2} day^{-1}~~mg·m^{-2}·day^{-1}~~ in spring (Fig. 6f), 4.42 ± 2.79 mg m^{-2} day^{-1}~~mg·m^{-2}·day^{-1}~~ in summer (Fig. 6h), and 2.28 ± 1.28 mg m^{-2} day^{-1}~~mg·m^{-2}·day^{-1}~~ in fall (Fig. 6j).

Table 3: Seasonal DDR averages (in mg m^{-2} day^{-1})~~, representative~~ for the period 12/2006-11/2022, along with the associated variability, for the North-East Atlantic Ocean (NEAO), North-Middle Atlantic Ocean (NMAO), North-West Atlantic Ocean (NWAO), Gulf of Guinea (GG), South-East Atlantic Ocean (SEAO), and South-West Atlantic Ocean (SWAO) sub-domains of the Atlantic Ocean.

	DDR (mg m^{-2} day^{-1})			
	DJF	MAM	JJA	SON
North-East Atlantic Ocean (NEAO) (Lons: 30°W-10°W / Lats: 10°S-40°N)	31.96 ± 27.03	34.01 ± 34.05	37.94 ± 55.99	17.42 ± 17.91
North-Middle Atlantic Ocean (NMAO) (Lons: 60°W-30°W / Lats: 10°S-40°N)	19.46 ± 18.41	23.16 ± 24.97	24.04 ± 29.31	14.29 ± 16.31
North-West Atlantic Ocean (NWAO) (Lons: 100°W-60°W / Lats: 10°N-40°N)	1.31 ± 2.19	8.77 ± 7.88	31.67 ± 23.85	4.74 ± 5.74
Gulf of Guinea (GG) (Lons: 10°W-15°E / Lats: 6°S-6°N)	37.24 ± 8.36	46.49 ±15.49	8.09 ± 2.59	8.77 ± 5.61
South-East Atlantic Ocean (SEAO) (Lons: 10°W-15°E / Lats: 14°S-6°S)	3.14 ± 3.59	2.61 ± 2.21	4.42 ± 2.79	2.28 ± 1.28
South-West Atlantic Ocean (SWAO) (Lons: 65°W-35°W / Lats: 50°S-22°S)	3.79 ± 4.02	2.97 ± 2.26	2.17 ± 1.38	1.41 ± 2.32

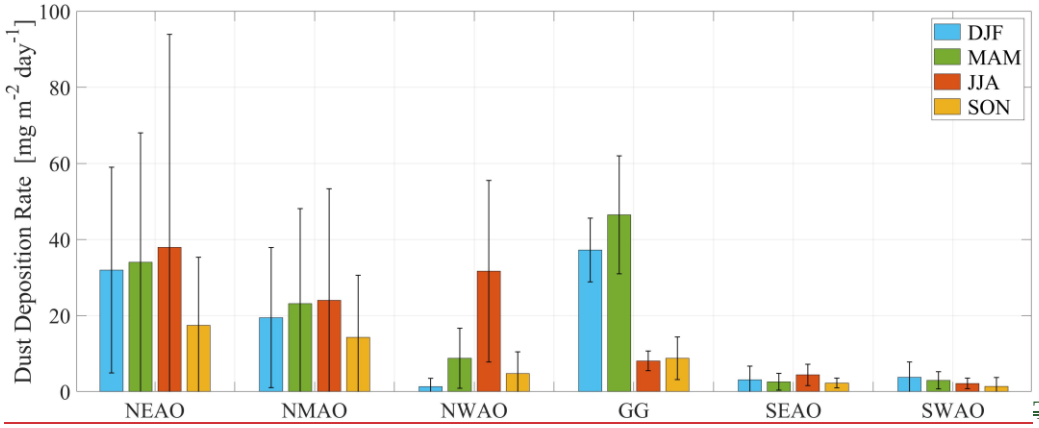

~~Table 3: Seasonal DDR averages (in mg m^{-2} day^{-1}), representative for the period 12/2006-11/2022, along with the associated variability, for the North-East Atlantic Ocean (NEAO), North-Middle Atlantic Ocean (NMAO), North-West Atlantic Ocean (NWAO), Gulf of Guinea (GG), South-East Atlantic Ocean (SEAO), and South-West Atlantic Ocean (SWAO) sub-domains of the Atlantic Ocean.~~

Figure 7: Visualization of seasonal DDR averages (in mg m^{-2} day^{-1}) for the period 12/2006-11/2022, along with the associated variability, for the North-East Atlantic Ocean (NEAO), North-Middle Atlantic Ocean (NMAO), North-West Atlantic Ocean

(NWAO), Gulf of Guinea (GG), South-East Atlantic Ocean (SEAO), and South-West Atlantic Ocean (SWAO) sub-domains of the Atlantic Ocean.

3.2 Evaluation of EO-based Dust Deposition estimates

735

	DDR (mg·m^{-2}·day^{-1})			
	DJF	MAM	JJA	SON
North-East Atlantic Ocean (NEAO) (Lons: 30°W-10°W / Lats: 10°S-40°N)	31.96 ± 27.03	34.01 ± 34.05	37.94 ± 55.99	17.42 ± 17.91
North-Middle-Atlantic Ocean (NMAO) (Lons: 60°W-30°W / Lats: 10°S-40°N)	19.46 ± 18.41	23.16 ± 24.97	24.04 ± 29.31	14.29 ± 16.31
North-West Atlantic Ocean (NWAO) (Lons: 100°W-60°W / Lats: 10°N-40°N)	1.31 ± 2.19	8.77 ± 7.88	31.67 ± 23.85	4.74 ± 5.74
Gulf of Guinea (GG) (Lons: 10°W-15°E / Lats: 6°S-6°N)	37.24 ± 8.36	46.49 ±15.49	8.09 ± 2.59	8.77 ± 5.61
South-East Atlantic Ocean (SEAO) (Lons: 10°W-15°E / Lats: 14°S-6°S)	3.14 ± 3.59	2.61 ± 2.21	4.42 ± 2.79	2.28 ± 1.28
South-West Atlantic Ocean (SWAO) (Lons: 65°W-35°W / Lats: 50°S-22°S)	3.79 ± 4.02	2.97 ± 2.26	2.17 ± 1.38	1.41 ± 2.32

4 Evaluation of EO-based Dust Deposition estimates

Towards verifying the accuracy, ensuring the reliability, and quantifying the uncertainties of the satellite-based estimations of dust deposition rate, implementation of in-situ observations of dust deposition fluxes as reference datasets is essential. However, numerous significant challenges inherent to the complex nature of oceanographic research hamper the feasibility of
740 establishing long-term and continuous in-situ measurements of high spatial coverage over extensive geographical areas and temporal periods, leading to limited availability of observational-reference datasets. In this study, we focus on the Albani et al. (2016$\underline{2014}$) compiled data record of in-situ dust deposition flux measurements, as enriched by Yu et al. (2019) with more recent observations in the region of interest (Table 4). To be more specific, the utilized reference dataset (Albani et al., 2016$\underline{2014}$; Yu et al., 2019) was established through revision and integration of pre-existing in-situ dust deposition flux
745 measurements (Honjo and Manganini, 1993; Kremling and Streu, 1993; Wefer and Fischer, 1993; Fischer et al. 1996; Jickells et al., 1996; 1998; Kuss and Kremling, 1999; Ratmeyer et al., 1999; Bory and Newton, 2000; Friese et al., 2017; Korte et al., 2017) across the broader Atlantic Ocean (Fig. 7$\underline{8}$a), through an effort for homogenization (Albani et al., 2016$\underline{2014}$; Yu et al., 2019), resulting in a robust record suitable to be used for scientific studies related to modern climate deposition of dust aerosols (Ginoux et al., 2001; Tegen et al., 2002; Lawrence and Neff, 2009; Mahowald et al., 2009).

750

Table 4: Compilation of sediment-trap climatologies of dust deposition fluxes.

Site No (##)	Latitude (deg. North)	Longitude (deg. East)	Observational Temporal Period	DDR (mg m^{-2} day^{-1} ~~mg/m^2 d~~)	Reference
1.	21.93	-25.23	1986-1987	18.36	Kremling and Streu, 1993; Jickells et al., 1996
2.	21.15	-20.69	1989-1990	56.11	Ratmeyer et al., 1999; Wefer and Fischer, 1993
3.	21.15	-20.68	1989-1990	53.97	Fischer et al. 1996; Wefer and Fischer, 1993
4.	19	-20.17	1990-1991	59.04	Bory and Newton, 2000
5.	18.5	-21.08	1991	51.34	Bory and Newton, 2000
6.	11.48	-21.02	1992-1993	61.97	Ratmeyer et al., 1999
7.	20.92	-19.75	1988-1989	60.05	Fischer et al., 1996; Wefer and Fischer, 1993
8.	20.92	-19.74	1989-1990	74.52	Jickells et al., 1996; Wefer and Fischer, 1993
9.	20.92	-19.74	1990-1991	31.21	Ratmeyer et al., 1999; Wefer and Fischer, 1993
10.	29.11	-15.45	1991-1992	11.37	Ratmeyer et al., 1999; Wefer and Fischer, 1993
11.	1.79	-11.13	1989-1990	11.78	Wefer and Fischer, 1993
12.	-2.18	-9.9	1989-1990	3.29	Wefer and Fischer, 1993
13.	33.15	-21.98	1993-1994	3.21	Kuss and Kremling, 1999
14.	33.15	-21.98	1993-1994	6.41	Kuss and Kremling, 1999
15.	-20.05	9.16	1989-1990	6.85	Wefer and Fischer, 1993
16.	-20.5	9.16	1989-1990	10.41	Wefer and Fischer, 1993
17.	-20.07	9.17	1989-1990	15.89	Wefer and Fischer, 1993
18.	32.08	-64.25	1981-1991	5.21	Jickells et al., 1998
19.	21.05	-31.17	1991-1992	10.22	Bory and Newton, 2000
20.	24.55	-22.83	1990-1991	14.27	Jickells et al., 1996
21.	28	-21.98	1990-1991	6.58	Jickells et al., 1996
22.	33.82	-21.02	1989-1990	13.01	Honjo and Manganini, 1993
23.	13.81	-37.82	2013	12	Korte et al., 2017
24.	12.39	-38.63	2013	23	Korte et al., 2017
25.	12.06	-49.19	2013	20	Korte et al., 2017
26.	12.02	-57.04	2013	52	Korte et al., 2017
27.	12	-23	2013	47	Korte et al., 2017

This section aims to quantitatively evaluate the ability of the satellite-based derived dust deposition rate product to replicate the characteristics of dust deposition measured by sediment traps, while also quantifying associated uncertainties. However, it should be emphasized that implementation of the in-situ observational dataset as reference record towards a direct and rigorous validation of the satellite-based dust deposition rate product established is not feasible, since most of the sediment-trap measurements date back to the 1980s and 1990s. The assessment follows the methodology ~~of~~ proposed by Yu et al. (2019) ~~applied~~ to account for the different temporal spans of sediment-trap measurements and satellite-based observations. More specifically, under the apparent limitations, the intercomparison is conducted on the basis of long-term climatological means,

evaluating the total dataset of spatially collocated satellite-based dust deposition rates against the correlative in-situ measurements (Fig. ~~7b~~8b), for the Atlantic Ocean sediment-trap sites (Fig. ~~7a~~8a). Overall, the performed evaluation reveals a general tendency of the satellite-based dust deposition rate product to overestimate the dust deposition rate measurements conducted at the sediment-trap observational sites (Table 5). This feature can be attributed to several sources and factors driving the spatially correlative evaluation, as discussed hereinafter, resulting into the observed discrepancies.

Table 5: EO-based Dust Deposition Rate product overall evaluation metrics established on the basis of reference dust deposition rate measurements conducted at sediment-trap observational sites, including absolute biases, relative biases, Root Mean Square Error (RMSE), Correlation Coefficient, Slope (S_{fit}) and Interception (I_{fit}) of liner regression fit.

Cor. Coef.	RMSE (mg m^{-2} day^{-1} ~~mg/m^2d~~)	Relative Bias (%)	Mean Bias (mg/m^2d)	S_{fit}	I_{fit} (mg m^{-2} day^{-1} ~~mg/m^2d~~)
0.79	15.97	19.82	5.42	0.85	9.49

First, with respect to CALIPSO-CALIOP observations, issues contaminating the dust deposition rate product resulting in the apparent overestimations can be attributed, among others, to misclassification of cloud layers (i.e., cirrus fringes) as aerosol layers (Liu et al., 2009; 2019) even under strict quality assurance criteria (Tackett et al., 2018) and to further erroneous subclassification of the classified layers as aerosol (Omar et al., 2009; Kim et al., 2018; Kar et al., 2019). For instance, marine aerosol layers (i.e., sea salt emissions) in the Marine Boundary Layer (MBL) - Free Troposphere (FT) entrainment zone characterized of low relative humidity (RH) conditions tend to obtain a crystal cubic-like shape (Haarig et al., 2017a), leading due to increased depolarizing capacity to aerosol subtype classification distinction ambiguities (Burton et al., 2013).

Second, the application of the atmospheric dust decoupling technique on optical products of the CALIPSO mission (Winker et al., 2010), namely the one-step POLIPHON (Tesche et al., 2009), is performed on the basis of several assumptions with respect to the depolarizing properties of the dust (Esselborn et al., 2009; Freudenthaler et al., 2009; Ansmann et al., 2011; ~~Groß~~ Gross et al., 2011a, 2015; Tesche et al., 2011; Veselovskii et al., 2016; Haarig et al., 2017b) and non-dust aerosol layers (Müller et al., 2007b; Ansmann et al., 2010; ~~Groß~~ Gross et al., 2012; Nicolae et al., 2013; Noh et al., 2013; Haarig et al., 2017a; Bohlmann et al., 2021; Veselovskii et al., 2022), introducing further uncertainties in the final near-global atmospheric dust aerosol product (Amiridis et al., 2013; Marinou et al., 2017; Proestakis et al., 2018; 2024; Aslanoğlu et al., 2022). More significant is considered the impact of incorrect implementation of dust lidar ratio values for the layers classified as dust aerosol, allowing to convert backscatter coefficient at 532 nm profiles to extinction coefficient at 532 nm profiles and accordingly to mass concentration profiles (Ansmann et al., 2019). For instance, implementation of the CALIPSO-default Version 4 (V4) dust aerosol subtype lidar ratio of 44 sr (Kim et al., 2018) and not of the updated in the present study for Saharan dust ~~lidar ratio~~LR of 53.1 sr for the North Atlantic Ocean dust outflow region (Floutsi et al., 2023) would reduce the rate of dust deposition and the estimate of the total deposited dust in the North Atlantic Ocean region up to ~20.7%. However, several studies and extensive experimental campaigns report significantly higher Saharan dust lidar ratio values for the West

Saharan Desert and the North Atlantic Ocean dust outflow region (Tesche et al., 2009; 2011; ~~Groß~~ Gross et al., 2011a; 2011b; 2015; Kanitz et al., 2013; 2014; Weinzierl et al., 2016; Haarig et al., 2017b; Rittmeister et al., 2017; Bohlmann et al., 2018; Floutsi et al., 2023) than the CALIPSO V4 default (Kim et al., 2018), attributed mainly to the different mineralogy of dust particles emitted from different dust sources into the atmosphere (Castellanos et al., 2024).

Third, marine sediment trap observations of atmospheric dust deposition into the ocean are challenging to interpret (e.g., Kohfeld and Harrison 2001) as the provided measurements do not necessarily represent the true atmospheric dust deposition to the surface of the ocean at the monitoring locations of the mooring sites (Siegel and Deuser 1997, Bory et al. 2002). One of the main sources of uncertainties in the intercomparison of satellite-based dust deposition products and sediment trap records is the time lag between dust emission and export towards and over the broader Atlantic Ocean, related to the EO-based estimation of dust deposition, and the arrival time at the depth of the operated sediment traps. More specifically, it is estimated that the Saharan dust layers leaving the African continent are transported westward at a speed of approximately 1000 km day^{-1}, needing about 5 to 7 days to cross as far as the eastern coast of the United States or the Gulf of Mexico (Huang et al. 2010; Prospero et al., 2014; Weinzierl et al., 2016). Upon deposition, the atmospheric dust layers release into the ocean dust particles characterized by a size distribution spanning over several orders of magnitude, extending between 0.1 μm and more than 100 μm in diameter (Weinzierl et al., 2016; Ryder et al., 2018; van der Does et al., 2018). ~~However, t~~The different size of the deposited dust particles ~~is related to~~are characterized by different dust transport pathways through the water column, since finer particles are characterized by slower settling speed (~~Van~~ van der Jagt et al., 2018; Guerreiro et al., 2021). More specifically, it is estimated that finer dust particles, with sinking speeds of about 1 to 35 m day^{-1} would have a lateral transport range during this period ~~of more than~~possible as far as ~500 km from the oceanic surface deposition area, depending also on the sampling depth (Siegel et al. 1990). Overall, it is estimated that the sinking speed of deposited particles towards the installed collectors operated at ~1200m leads to a transit period of ~5 days, while for deeper depth collectors the transit period ranges between 10 to 20 days (Fischer et al., 1996; Ratmeyer et al, 1999; ~~Van~~ van der Does et al., 2016), introducing uncertainties on the temporal intercomparison process of the satellite-based dust deposition products and sediment trap records.

It should be emphasized that ~~W~~with respect to the spatial intercomparison, during the transit period between atmospheric deposition and the collection by the sediment traps, deposited dust layers are subject to currents of variable pathways. For instance, upon deposition of Saharan dust to the proximity of the western coast of the Saharan desert, off Cape Blanc, the oceanic circulation carries the deposited layers thousands of kilometers southwards where the Canary Current meets either the westward North Equatorial Current (NEC) or the eastward North Equatorial Counter Current (NECC), possible resulting not only to extended diffusion of the deposited layers but also to different oceanic transport pathways, thus to collection of the deposited atmospheric dust particles over a relatively well-specified area by sediment traps established and operated over distances of hundreds of kilometers apart (Ratmeyer et al, 1999).

During this period, deposited dust particles may be subject to several mechanic and chemical alteration processes, of hydrodynamic nature (i.e., fractionation and sorting; McCave et al., 1995), remineralization, coagulation or aggregation, disaggregation or decomposition (Duce et al., 1991; Jickells et al., 2005; Ratmeyer et al, 1999; Korte et al., 2017) or dissolution

and microbiological partial disintegration (Alldredge et al., 1990). The temporal intercomparison may be further affected by the oceanic seasonality, as reported by time-series of lithogenic fluxes in sediment traps, which is substantially different to the seasonality of atmospheric dust emission, transport, and deposition (Amiridis et al., 2013; Gkikas et al., 2022; Proestakis et al., 2024). More specifically, on the basis of an array of five moorings deployed below the SAL, ~~Van~~ van der Does et al. (2016) and Korte et al. (2017) reported that several of the installed moorings demonstrated a clear seasonality in lithogenic fluxes, mainly during summer and autumn (~~Van~~ van der Does et al., 2016), while in other cases of sediment traps no clear seasonality was evident (Korte et al., 2017). The outcomes of oceanic medium to weak seasonality support documented findings as reported by Ratmeyer et al. (1999) on the basis of lithogenic samples collected by several sediment traps operated in the Cape-Verde - Cape Blanc - ~~Cape~~ Cabo Verde Islands broader area.

Another source of uncertainties arises by the variable methods used to extract the dust-related component of the total mass collected by the sediment traps, containing quartz, clay minerals, and feldspars parts, the so called lithogenic fraction (Wefer and Fischer, 1993; Fischer and Wefer, 1996; Neuer et al., 2002; Fischer and Karakas, 2009; Fischer et al., 2016). As discussed by McCave et al. (1995) and Ratmeyer et al. (1999), the comparison between different methods, also on the basis of the different applied instrumentation, is especially challenging, mainly due to the complexity of the analysis techniques and the detectable size ranges. Moreover, the detectable sensitivity may result to substantial differences (underestimation) against the EO-based dust deposition rate product established in the framework of the present study. Since a sufficient overlap of the sediment trap lithogenic fraction sizes and the atmospheric dust PSD reported on the basis of extensive experimental campaigns over the Atlantic Ocean ~~on the basis of~~conducted with airborne in situ measurements is not accounted for, a more direct and accurate comparison is not feasible. More specifically, while measured atmospheric dust PSDs range between 0.1 and 100 μm in terms of diameter (Weinzierl et al., 2016; Ryder et al., 2018), frequently measurements of so broad PSDs with sediment trap techniques, especially during the past decades, was particularly challenging. For instance, Ratmeyer et al. (1999) volume distribution spectra analysis and grain size statistics were performed only for the fraction 6-63 μm, in order of the provided sediment trap record to be comparable with previously established grain size distributions with surface sediments in the proximity of the northwest Africa (Koopmann, 1981; Sarnthein et al., 1982; McCave et al., 1995).

Moreover, oceanic conditions are not always favourable, with strong currents (> 12 cm s^{-1}) and deep eddy penetration resulting to vertical displacement of mooring line possible contaminating the unbiased collection of settling particles (Knauer and Asper, 1989; Korte et al., 2017). It should be mentioned that though dust sedimentation measurements are frequently used to support quantitatively evaluation efforts of model outputs or satellite-based products, time-series of records are frequently partially interrupted or incomplete (Ratmeyer et al., 1999). Due to the highly episodic nature of dust (Prospero et al. 1987; Mahowald et al. 2003), evidence suggests that in some cases the available records are based on a relatively small number of dust events (Avila et al., 1997). It should be noted that temporal and spatial sampling limitations of dust deposition rate measurements conducted at the sediment-trap observational sites, related to inherent challenges of oceanic research, may result to lack of observations over extensive geographical areas or to not full-year coverage, thus to records not fully representative of dust deposition patterns (Yu et al., 2019).

Finally, the sediment-trap observations record and the EO-based dust deposition product refer to different time spans. More specifically, the majority of the performed sediment-trap measurements were carried out in the 1980s and 1990s, approximately a decade before CALIPSO optical products became available. Thus, the performed intercomparison serves more as an indirect evaluation of the satellite-based product of dust deposition rate against the sediment-trap observations rather than a rigorous validation.

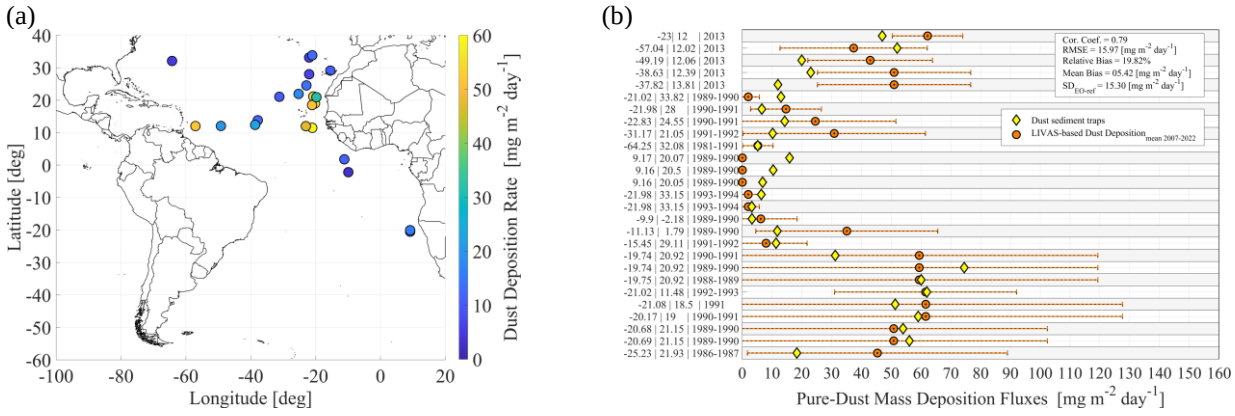

Figure ~~7~~8: In-situ dust deposition flux measurements and locations of sediment-sites (Table 4) (a). Long-term evaluation of the satellite lidar-based Dust Deposition Rate product against the corresponding in-situ dust deposition fluxes climatology (mg m^{-2} day^{-1} ~~$mg/m^2/d$~~) (b).

Overall, considering the several sources of uncertainties and the methodological factors driving the observed discrepancies, the EO-based dust deposition rate product and the sediment-trap observations are in rather good agreement (slope of 0.85, intercept of 9.49 mg m^{-2} day^{-1} ~~$mg/m^2/day$~~, and Pearson correlation coefficient ~0.79). The ~~general~~ apparent ~~trend~~ feature of satellite-based dust deposition is to overestimate those from the in situ provided observations (mean bias of 5.42 mg m^{-2} day^{-1} ~~$mg/m^2/day$~~, relative bias of 19.82%, and RMSE of 30.3 mg m^{-2} day^{-1} ~~$mg/m^2/day$~~). However, it is notable that the satellite-based dust deposition rate product consistently reproduces the dust deposition spatial patterns recorded by the sediment traps

installed and operated across the broader Atlantic Ocean, with a positional accuracy and magnitude generally within a factor of 2 compared to sediment trap measurements (Table 5).

3.3 Total Dust Deposited into the broader Atlantic Ocean

~~**5 EO-based Dust Deposition Rate and ESMs**~~

~~The present section aims to compare the EO-based dust deposition rate products and estimates of dust deposition provided by Earth System Models (ESM). The objective of the comparison lies in identifying common dust spatial and seasonal patterns, addressing whether the EO-based dust deposition rate product shares similar characteristics in terms of spatio-temporal variability with model-based deposition estimates, implemented in AeroVal (https://aeroval.met.no/; last access: 21 January 2025). As an intermediate step, the EO-based atmospheric dust product of the ESA-LIVAS-CDR in terms of DOD at 532 nm is compared against AErosol RObotic NETwork (AERONET; https://aeronet.gsfc.nasa.gov/; last access: 3 January 2025; Holben et al., 1998) coarse-mode AOD optical product derived via the Spectral Deconvolution Algorithm (SDA; Eck et al., 1999; O'Neill et al., 2001a, b, 2003). This step is applied since the capacity of the ESA-LIVAS-CDR to provide accurately the spatiotemporal variability of the atmospheric dust conditions is a crucial cornerstone for quantitatively and qualitatively quantifying the dust deposited component across the dust transport over the ocean. The objective of the comparison lies in identifying common dust spatial and seasonal patterns, addressing whether the EO-based dust deposition rate product shares similar characteristics in terms of spatio-temporal variability with model-based deposition estimates, implemented in AeroVal. AeroVal is a web-based platform, developed at the Norwegian Meteorological Institute, designed for the evaluation of climate and air quality models. The platform employs the pyaerocom library (a successor of AeroCom evaluation and visualization tool) to collocate model data with observations from a variety of sources, including ground-based observation networks (EBAS, EEA, AERONET) and satellites (MODIS, AATSR etc). AeroVal allows for the computation of statistics, such as biases and correlations, and provides an interactive web interface to facilitate easy exploration of data, models intercomparison, and evaluation statistics. It is utilized in several projects, including among others, the CMIP (Mortier et al., 2020), AeroCom (e.g. Gliß et al., 2021), CAMS, and EMEP (https://aeroval.met.no/pages/evaluation/?project=domos&experiment=Dust_AOD; last visit: 20/10/2024).~~

~~In this work, the Aeroval tool is used for consistency checks by comparing LIVAS-DOD at 532 nm and Dust Deposition Rate with simulation results from three atmospheric transport models, i.e. EMEP MSC-W (hereafter EMEP; Sect.2.1.4), EC-Earth3-Iron (EC-Earth3; Sect.2.1.3), and MONARCH (Sect.2.1.5) for the year 2020. As the accuracy of dust deposition calculations relies on the accuracy of the estimates of the dust load in the atmosphere, DODs from LIVAS and EMEP, EC-Earth3, and MONARCH models are as a first step evaluated against AERONET coarse-mode AOD (Dubovik et al., 2006), update September 2024. The comparison is made on a basis of monthly mean DOD and deposition fluxes. Note that while model~~

results are produced at a daily resolution, LIVAS data are provided in the framework of the study at seasonal temporal resolution, so that all three months within a season are assigned the same value.

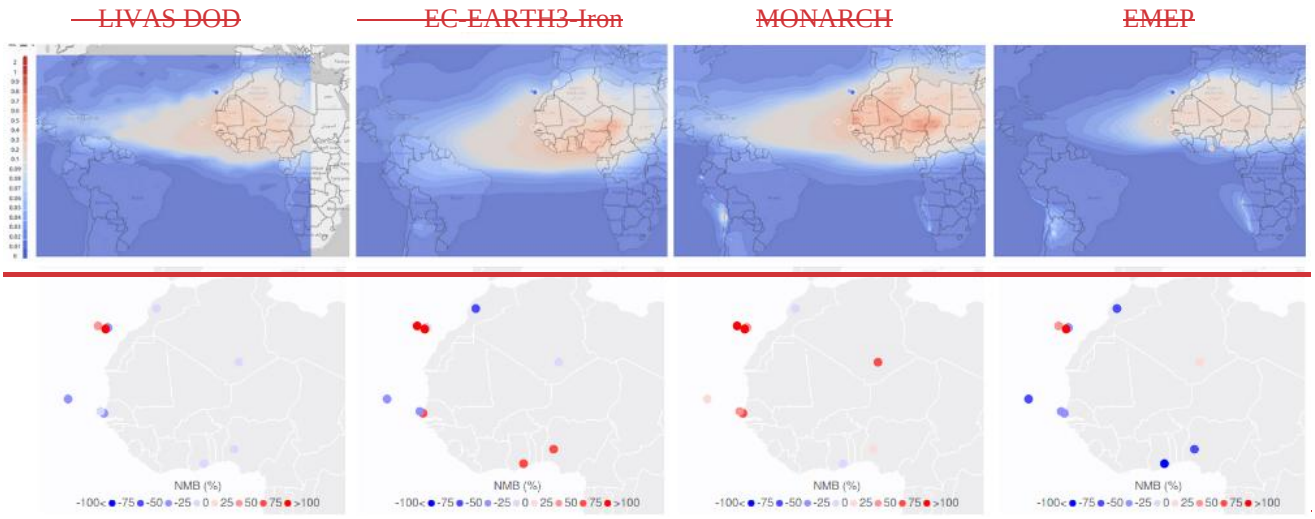

Figure 8: Yearly mean DOD (upper panels) and Normalized Mean Bias with respect to AERONET coarse-mode AOD (lower panels) for LIVAS, EC Earth3, MONARCH, and EMEP for the year 2020. On the upper maps, AERONET data is also presented by the circles.

The maps of yearly mean DOD from LIVAS product and simulated by EC-Earth3, EMEP, and MONARCH model presented in Figure 8 (upper panels), show similar patterns of spatial distribution, representing the emissions of dust in the African deserts and its westward transport over the Atlantic Ocean. EC-Earth3 simulates the largest values of DOD, followed by MONARCH, LIVAS, and EMEP. The lower panels in Figure 8 show yearly Normalized Mean Biases of LIVAS and modelled DOD with respect to AERONET coarse mode AOD. The observations with acceptable time coverage (over 50%) within LIVAS estimated area were available at twelve AERONET sites: six continental and six sites west of the African coast (i.e. on Tenerife, Cape Verde, and La Palma). LIVAS DOD is around 20-30% lower compared to AERONET coarse mode AOD at the continental sites and in Cape Verde while it is 47% higher on La Palma. For the sites on Tenerife, we see both under- and over- estimation by LIVAS. LIVAS DOD is higher than AERONET coarse mode AOD at the mountain sites Izaña (2410 m above sea level) by 44% and at Teide (3555m asl) by a factor of 5.5, where the greatest overestimation is for in October through December months (the only available observations at Teide). On the other hand, LIVAS underestimates by around 45% observations at La Laguna and Santa Cruz de Tenerife (observations only available for January-June and December), with the largest bias in June-July.

The largest difference among the models is that MONARCH, and especially EC-Earth3, simulate larger dust emissions from the Sahel desert compared to EMEP. DOD from MONARCH is the closest to AERONET coarse mode AOD south of Sahel; EC-Earth3 overestimates it by 60-70%, while EMEP underestimates by 70-80%. The agreement is better between EMEP DOD

and AERONET at one site in Sahara, whereas EC-Earth3 underestimates and MONARCH overestimates AERONET coarse-mode AOD at this site, respectively. MONARCH overestimates AERONET coarse-mode AOD at the African coastal sites and the islands. At the low-altitude sites on Tenerife and Cape Verde, DOD from LIVAS and EC Earth3 are closer to AERONET, while EMEP underestimates and MONARCH overestimates those. LIVAS and all three ESMs are biased rather high for all high-elevations AERONET sites (i.e., Tenerife and La Palma). The monthly variation of DOD and the scatterplot of LIVAS and models vs AERONET coarse-mode AOD at all considered sites are shown in Figure 8 (right and middle panels). However, it should be noted that LIVAS DOD at 523 nm and ESM dust outputs include both the fine-mode and coarse-mode dust components while the AERONET AOD at 550 nm component constitutes of the coarse-mode fraction of dust, possible resulting to increasing comparison uncertainties.

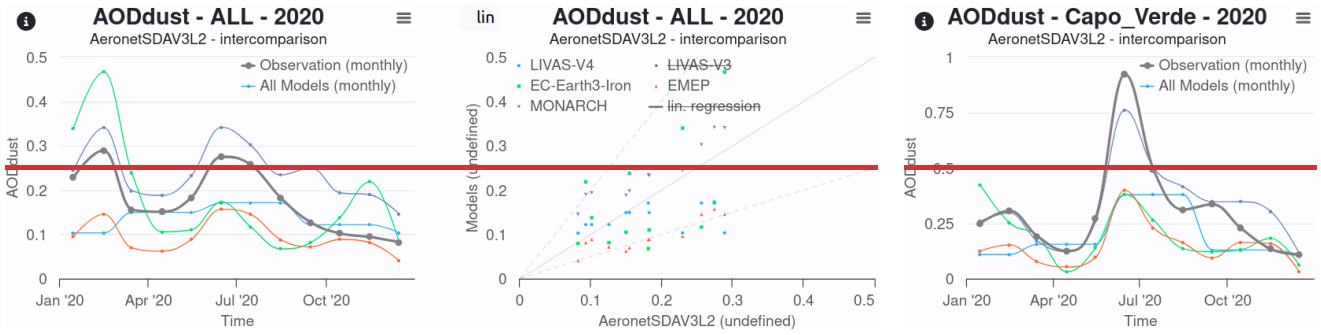

Figure 9: Monthly series (left) and scatterplot (middle) comparing DOD from LIVAS (seasonal mean) and simulated by the models (EC EARTH3 Iron, MONARCH, and EMEP) with AERONET coarse-mode AOD at the sites shown in Fig. 8; and the monthly series for Cape Verde (right) for the year 2020.

In general, LIVAS and ESMs describe quite well the observed monthly cycle of AERONET coarse-mode AOD observed. LIVAS underestimates coarse-mode AOD for January-February, and also June-July. EC-Earth3 overestimates coarse-mode AOD for January to March and for November, while underestimates for April through September. MONARCH shows an overestimation of AERONET (larger in the autumn), whereas EMEP, showing a general underestimation, corresponds AERONET observations relatively well for the autumn months. In Figure 9 (right panel), we also present the monthly time series of calculated DOD and coarse-mode AOD at Cape Verde. This site can be considered representative of the dust plume transported westward off the African deserts over the subtropical eastern North Atlantic. The best agreement with AERONET coarse-mode AOD is seen for DOD from MONARCH. LIVAS DOD is quite like that from EMEP and EC-Earth3, and is lower compared to AERONET coarse-mode AOD, especially in the summer months. The overall evaluation statistics (bias and spatial correlation) for LIVAS and modelled DOD with respect to AERONET coarse-mode AOD are summarized in Fig 10.

(a)

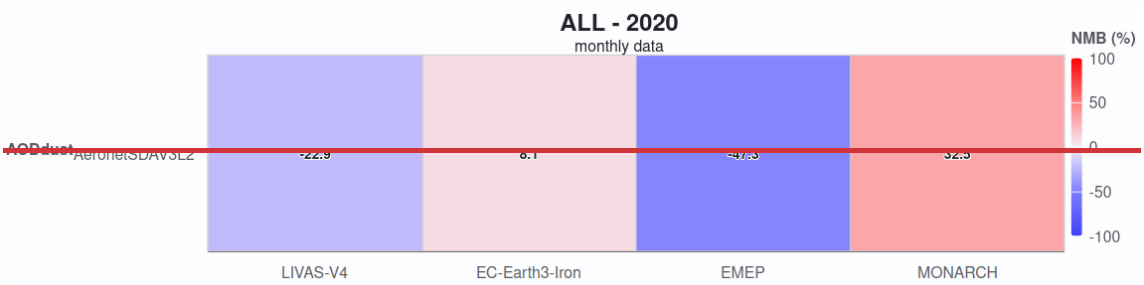

(b)

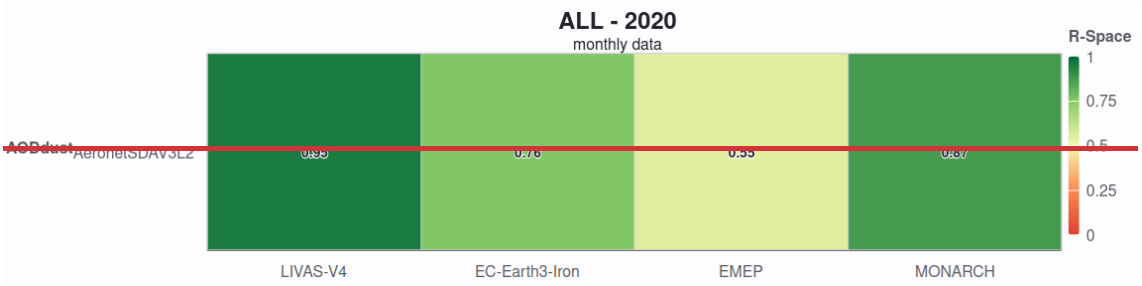

Figure 10: Overall evaluation statistics in terms of relative bias (NMB%; Fig.10a) and spatial correlation (R_Space; Fig.10b) for the LIVAS DOD at 532 nm and the modelled DOD with respect to AERONET coarse mode AOD (SDAVL2).

Table 6. Overall evaluation statistics in terms of normalized bias and spatial correlation for the LIVAS DOD at 532 nm and the modelled DOD with respect to AERONET coarse mode AOD (SDAVL2).

	LIVAS DOD	EC Earth3 Iron	MONARCH	EMEP
NMB (%)	-22.9	8.1	32.5	-47.3
R Space	0.95	0.76	0.87	0.55

In further comparison (referred to as LIVAS_as_obs), we assess models' results against the ESA LIVAS DOD at 532nm data. The comparison is done on the monthly basis at 2°x2° grid cells with available ESA-LIVAS DOD at 532 nm data. Figure 11 presents the maps of normalized mean biases with respect to LIVAS for EC_Earth3, MONARCH, and EMEP. Over the African deserts, MONARCH (which includes dust particles up to 20 μm in diameter) overestimates LIVAS DOD, while EC_Earth3 and EMEP have relatively smaller biases (especially EC-Earth3), i.e. positive in eastern-southeastern parts of Sahara and slightly negative in central/western parts. MONARCH also simulates DOD higher than LIVAS over the subtropical North Atlantic and in the east of South Atlantic Ocean. EC_Earth3 has quite small (positive and negative respectively) biases compared to LIVAS DOD in the grid cells over North Atlantic Ocean, while overestimating over its equatorial part and South Atlantic Ocean. EMEP results are quite close to LIVAS DOD over the Atlantic north of equator, but underestimates over the South Atlantic Ocean. It should be noted that due to a rather simplified description of AOD in the EMEP model, the uncertainties in DOD modelling are associated with both dust three-dimensional concentrations and assumptions for dust specific extinction.

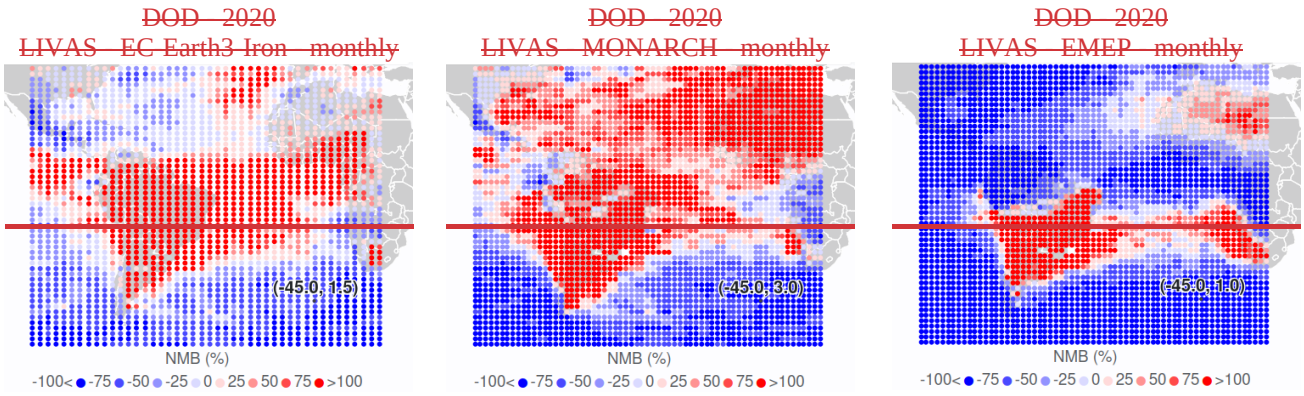

Figure 11: Normalized mean bias of modelled DOD compared with LIVAS data for EC-Earth3 (left), MONARCH (middle), and EMEP (right).

The maps of yearly mean dust total (dry and wet) deposition rate established on the basis of LIVAS and simulated with the EC-Earth3-Iron, EMEP, and MONARCH models are shown in Figure 12. The general pattern of dust deposition over the Atlantic Ocean is quite similar, though the models simulated dust deposition rates smaller compared to the EO-based dust deposition rate estimates, with MONARCH results being closer to those and EC-Earth3-Iron providing the lowest dust deposition rates in terms of magnitude. Figure 13 presents the maps of relative biases for dust deposition rate from the three ESMs with respect to the estimates of the present study. Along the dust plume core, EC-Earth3-Iron has the largest negative bias (mostly around -65 to -80%), EMEP mostly underestimates (with bias varying mostly between 30 and 60%), while MONARCH has the lowest bias (an order of 15-40%). Zonally, the models' biases remain quite similar across the Atlantic Ocean almost as far as the Caribbean Sea, indicating similar east-to-west dust deposition gradients. However, over the Caribbean Sea, the models' underestimation of LIVAS dust deposition increases. To the north and south of the main dust plume, the models' results show smaller negative and positive biases with respect to LIVAS dust deposition, respectively.

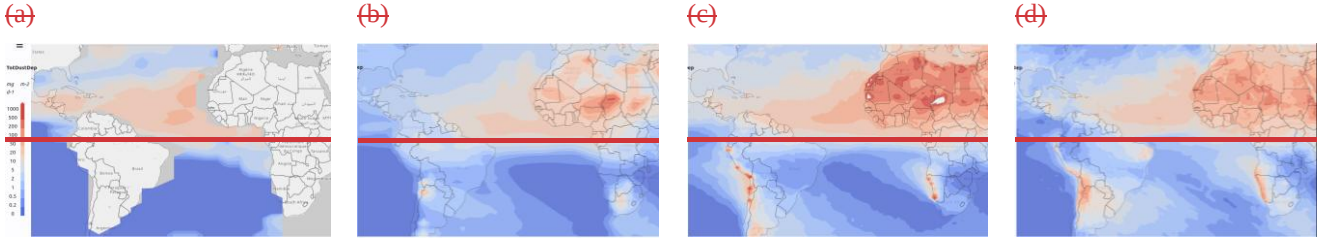

Figure 12: Yearly mean dust deposition rate (mg m^{-2} d^{-1}) from LIVAS (a) and simulated with EC-Earth3-Iron (b), MONARCH (c), and EMEP (d). Year: 2020.

(a) (b) (c)

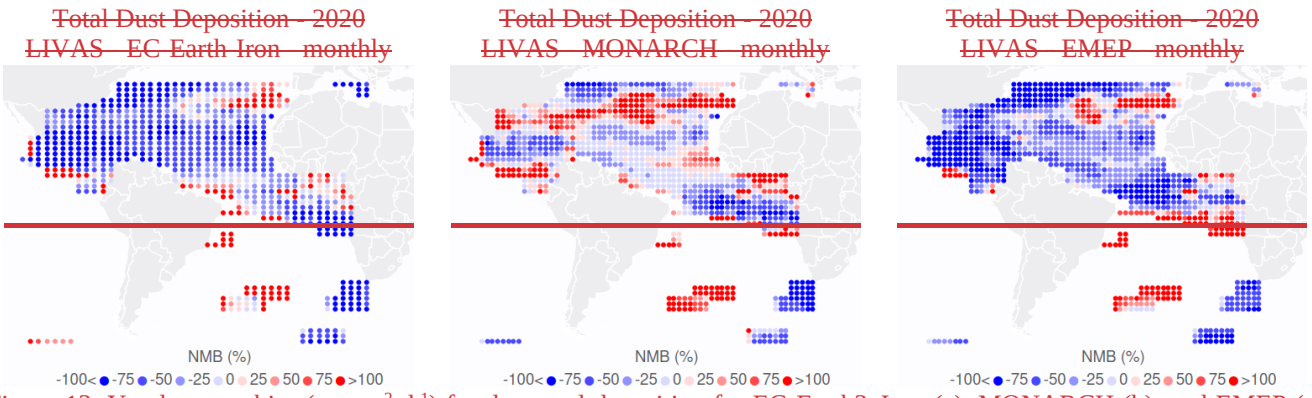

Figure 13: Yearly mean bias (mg m^{-2} d^{-1}) for dust total deposition for EC-Earth3_Iron (a), MONARCH (b), and EMEP (c) with respect to LIVAS data. Year: 2020. Here, the empty grid cells are those without LIVAS data (corresponding to zeroes in Fig. 12).

The timeseries in Figure 14 compare profiles of DOD (a) and deposition rate (b), simulated by the three models and those produced by LIVAS. The profiles are the averages over all of 2°x2° grid cells with LIVAS data (Fig. 13). The EMEP model shows better agreement with LIVAS DOD, slightly underestimating it. EC-Earth3-Iron overestimates LIVAS DOD for January to March, showing quite good correspondence otherwise. MONARCH simulated DOD higher than LIVAS through the year. For dust deposition, no one of the models manage to reproduce LIVAS summer maximum, with EC-Earth3-Iron underestimating LIVAS the most and simulating winter/autumn maxima instead. The reported higher dust deposition by LIVAS compared to ESMs more probably relates to the of the historic "Godzilla" dust intrusion over the Atlantic Ocean in June 2020, with atmospheric dust load substantially underestimated by dust models (Yu et al., 2021), with dust removal processes more efficiently removed from the atmosphere (Yu et al., 2019; Kim et al., 2014). For the other seasons, MONARCH overestimates LIVAS dust deposition, while EMEP and Earth3-Iron dust deposition rates are quite close to LIVAS.

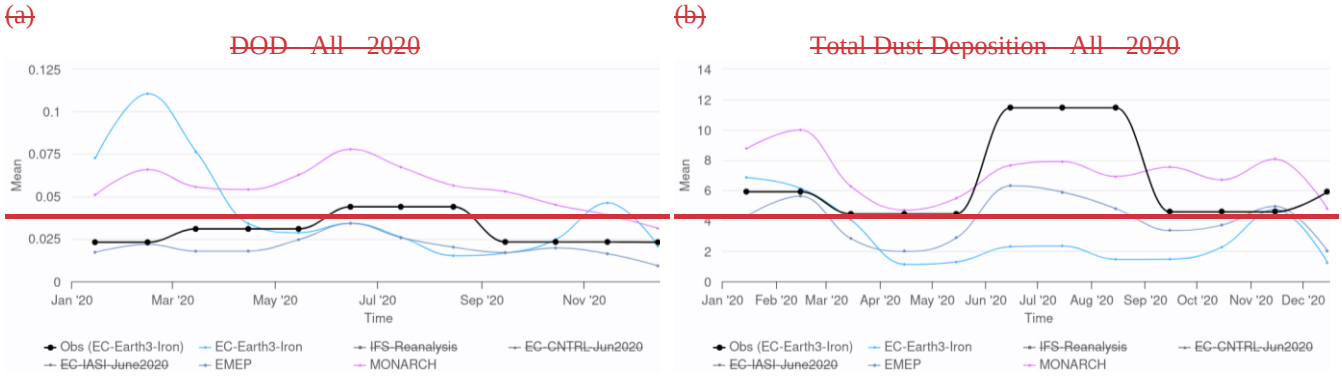

Figure 14: Monthly series of DOD and dust total deposition from LIVAS (Obs, black line), EC-Earth3, MONARCH, and EMEP (models' results are collocated with LIVAS data at grid cells of 2°x2°).

~~The overall evaluation statistics (bias and spatial correlation) for model simulated DOD and deposition rate with respect to LIVAS data are summarized in the heatmaps (Fig. 15). Those are yearly mean statistics, averaged over all grid cells of 2°x2° where LIVAS data available (i.e. coloured cells in Fig. 13). The spatial correlation between the models and LIVAS is quite high (between 0.7 and 0.94). The EMEP model underestimates both DOD and deposition by about 35%, which partly could be due to somewhat lower African dust emissions compared with LIVAS (as seen from comparison with AERONET coarse mode AOD (Figs. 8-9). EC-Earth3_Iron overestimates by 42% LIVAS DOD, but underestimates by 55% LIVAS dust deposition. The largest positive bias with respect to LIVAS data is seen for DOD from MONARCH (81%), while its dust deposition is quite close to that from LIVAS.~~

~~(a)~~ ~~(b)~~

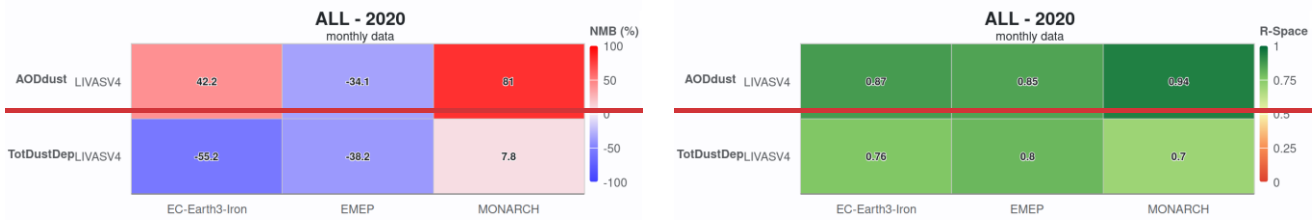

~~Figure 15: Summary statistics (relative bias, NMB% — Fig15.a, and spatial correlation, R Space — Fig15.b) of models' comparison with LIVAS DOD and total deposition.~~

~~6 Total Dust Deposited into the broader Atlantic Ocean~~

Figure ~~16~~ 9 provides ~~a~~ the quantification of the total annual- (Fig. ~~16a~~9a) and ~~the~~ seasonal-mean (Fig. ~~16b~~9b) dust deposition (Tg, 1 Tg = 10^{12} g) into the broader Atlantic Ocean (60°S-40°N, 100°W-20°E) per year. On the basis of sixteen full years of CALIPSO observations (12/2006-11/2022) it is estimated that on a basin scale the yearly-average dust deposition accounts to 274.79 ±31.64 Tg (Fig. ~~16~~9-left panel). With respect to the intrannual-seasonal variability (Fig. ~~16~~9-right panel), dust deposition into the ocean is generally highest in summer and lowest in autumn, estimated to 93.10 ±11.65 Tg and 40.62 ± 11.44 Tg for JJA and SON respectively. In spring and winter seasons, intermediate activity of dust deposition into the ocean is observed, estimated to 77.3 ±19.93 Tg and 63.78 ±12.03 Tg for MAM and DJF respectively. The apparent seasonal variability, subject to the high variability of dust emission, transport, and removal processes, propagates into the observed inter-annual fluctuations of the amount of dust deposited into the Atlantic Ocean, resulting to high year-to-year heterogeneity. Moreover, a negative statistically significant trend in dust deposition at the significance level of 0.05 is observed, characterized by slope -13.35 Tg yr^{-1} and offset 306.97 Tg. In addition, with respect to the year-to-year variability, it is estimated that the total dust deposition on basin scale ranges between as low as ~221.1 Tg (2019) to as high as ~324.6 Tg (2008). As indicator to the interannual and seasonal-intrannual variability of dust deposition the normalized standard deviation (NSD) is provided, calculated as the ratio of the standard deviation of the seasonal dust deposition of each year to the mean seasonal dust deposition

of each year and as the ratio of the standard deviation of the seasonal dust deposition for all seasons to the mean seasonal dust deposition for all seasons over the 12/2006-11/2022 period, respectively. The larger the NSD, the greater the variability of dust deposition. With respect to the year-to-year amount of dust deposited into the Atlantic Ocean basin, NSD shows mean intrannual variability about ~36.03%. With respect to the seasonal amount of dust deposited on basin scale, NSD shows largest and lowest variability in spring (MAM) and summer (JJA) season, of ~25.78% and ~12.52% respectively. In autumn and winter seasons, dust deposition into the ocean is slightly lower than in spring, estimated to ~28.16% and ~18.87% for SON and DJF respectively.

Table ~~7~~6: Annual-mean and seasonal-mean dust deposition (Tg, 1 Tg = 10^{12} g) and Normalized Standard Deviation (%) into the broader Atlantic Ocean (60°S-40°N, 100°W-20°E) on the basis of sixteen full years of CALIPSO observations (12/2006-11/2022).

	Dust Deposition (Tg)	NSD (%)
Annual	274.79 ± 31.64	~36.03%
DJF	63.78 ± 12.03	~18.87%
MAM	77.3 ± 19.93	~25.78%
JJA	93.10 ± 11.65	~12.52%
SON	40.62 ± 11.44	~28.16%

	~~Annual~~	~~DJF~~	~~MAM~~	~~JJA~~	~~SON~~
~~Dust Deposition (Tg)~~	~~274.79 ± 31.64~~	~~63.78 ± 12.03~~	~~77.3 ± 19.93~~	~~93.10 ± 11.65~~	~~40.62 ± 11.44~~
~~NSD (%)~~	~~~36.03%~~	~~~18.87%~~	~~~25.78%~~	~~~12.52%~~	~~~28.16%~~

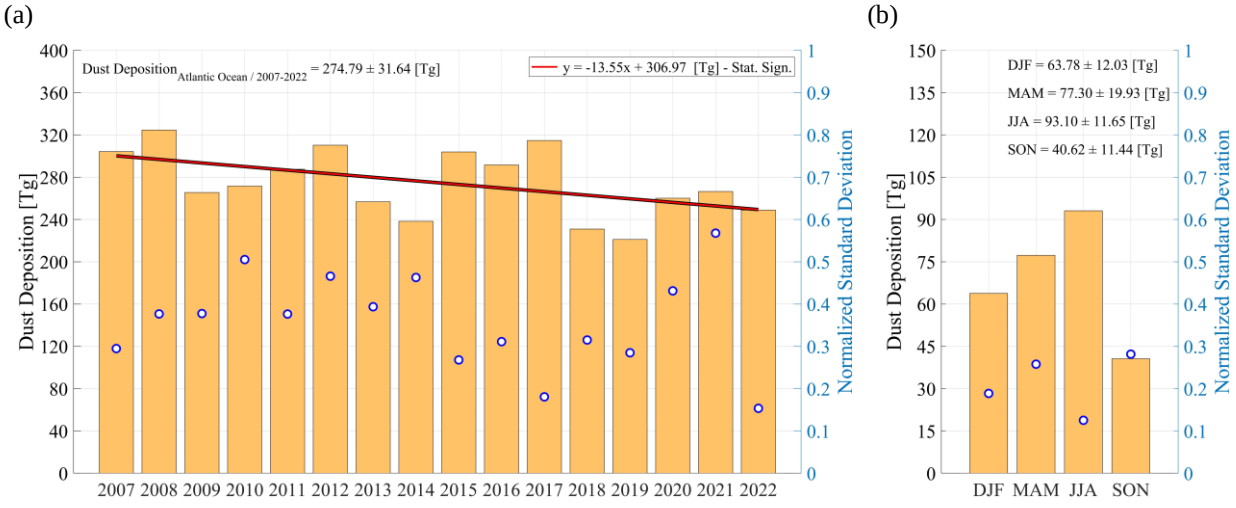

Figure ~~16~~9: Quantification of the (a) total annual-mean and (b) seasonal-mean dust deposition (Tg yr^{-1}, 1 Tg = 10^{12} g) into the broader Atlantic Ocean (60°S-40°N, 100°W-20°E) on the basis of 16-years of CALIPSO observations (12/2006-11/2022). Open circles in blue colour denote the annual-mean (left) and seasonal-mean (right) Normalized Standard Deviation (NSD).

Despite the vital role of atmospheric deposited lithogenic material for ocean biogeochemistry and for understanding environmental impact of the atmospheric dust cycle, the availability of direct mineral dust deposition measurements is limited. Thus, in order to connect these sparse in-situ observations and gain insight into the highly heterogeneous both in time and space influx of dust particles into the broader ocean several efforts have been undertaken (Table ~~8~~7), primarily relying on numerical model simulations (i.e., Duce et al., 1991; Prospero et al., 1996; Ginoux et al., 2001; Zender et al., 2003; Luo et al., 2003; Ginoux et al., 2004; Tegen et al., 2004; Jickells et al., 2005; Johnson et al., 2010; Kim et al., 2014; Kok et al., 2023) but also following the unprecedented increase in the range, quality, and frequency of satellite-based observations on remote sensing of dust (i.e., Kaufman et al., 2005; Foltz, 2014; Yu et al., 2015; 2019). Figure ~~17~~ 10 compares the satellite-based estimates of dust deposition of the present study (12/2006-11/2022 average) across the broader Atlantic Ocean (AO), North Atlantic Ocean (NAO), and South Atlantic Ocean (SAO) with documented estimates of dust deposition by other studies. This approach serves more as cross-assessment rather than a rigorous evaluation since the majority of the reported estimates rely on highly variable approaches, assumptions, parametrizations, considered meteorology, temporal periods, and domains.

As examples on the variability of the methods used, the numerical model simulations of Ginoux et al. (2001) on the sources and distributions of dust aerosols, reporting dust deposition rate of ~184 Tg yr^{-1}, ~20 Tg yr^{-1}, and ~204 Tg yr^{-1} across the North Atlantic Ocean, South Atlantic Ocean, and the broader Atlantic Ocean, respectively, averaged over a five-year period (1987-1990 and 1996), were based on the Georgia Global Ozone Chemistry Aerosol Radiation and Transport (GOCART) model, implementing input assimilated meteorology fields from the Goddard Earth Observing System Data Assimilation System (GEOS DAS; Schubert et al., 1993), ~~and a~~ dust size distribution of seven modes between 0.1 and 6 μm (radius), and dust density of 2.5 g m^{-3} (Chin et al., 2000). The 1990s climatology of Zender et al. (2003), based on the Dust Entrainment and Deposition (DEAD) model driven by the National Center for Environment Prediction (NCEP) meteorology (Kalnay, 1996), reports dust deposition rate of ~178 Tg yr^{-1}, ~29 Tg yr^{-1}, and ~207 Tg yr^{-1} across the North Atlantic Ocean, South Atlantic Ocean, and the broader Atlantic Ocean, respectively, accounting though for larger dust particles of size 0.1 to 10 μm in terms of diameter. A few years later, the dust deposition estimates of Johnson et al. (2010) were based on simulations with the global chemical transport model GEOS-Chem for the period extending between October 2006 and September 2007, distributing dust in four modes between 0.2 and up to 12.0 μm in terms of diameter (Fairlie et al., 2007). The study reported dust deposition of ~22 Tg yr^{-1}, slightly lower than the dust deposition estimates provided by Gaiero et al. (2003) of ~30 Tg yr^{-1}, focusing ~~both~~ on the South Atlantic Ocean domain and more specifically on the Patagonian dust source regions. The corresponding total South Atlantic Ocean total dust deposition, upon accounting in addition to South America arid areas (McConnell et al., 2007; Mazzonia and Vazquez, 2009; Ginoux et al., 2012) the major dust sources of South Africa (Eckardt and Kuring, 2005; Bryant et al., 2007; Ginoux et al., 2012; Vickery et al., 2013; Gkikas et al., 2022), was estimated significantly higher to ~86 Tg yr^{-1}

by Kok et al. (2023). Kaufman et al. (2005), on the basis not of model simulations but on ~~EOs~~ satellite-based observations of ~~dust~~ aerosols provided by Terra - ~~Moderate Resolution Imaging Spectroradiometer (~~MODIS~~;~~ (Remer et al., 2005) ~~observations~~ in 2001 estimated dust emitted from Africa and deposited to the Atlantic Ocean as far as the Caribbean approximately ~190 Tg yr^{-1} for the year 2001. Yu et al. (2019) implemented CALIPSO-CALIOP (Winker et al., 2010) dust profiles on synergy with DOD products established on the basis of observations provided by MODIS (Remer et al., 2005), MISR (Garay et al., 2020), and IASI (Capelle et al., 2014) radiometers, over the Tropical Atlantic Ocean domain. On the basis of a ten-year period (2007-2016) and basin-scale average (5°S-35°N), Yu et al. (2010) reported ~151.6 Tg yr^{-1} on the basis of CALIOP, and ~221.5 Tg yr^{-1} on the basis of CALIOP-MODIS, ~168 Tg yr^{-1} on the basis of CALIOP-MISR, and ~136 Tg yr^{-1} on the basis of CALIOP-IASI synergies. These provided indicative examples of performed studies highlight the discrepancies between reported dust deposition quantification estimates on the basis of highly variable approaches applied, assumptions and parametrizations considered, meteorology fields used, and temporal periods and regions of interest of each study.

Table ~~8~~7: Documented numerical model simulations and satellite-based estimates of dust deposition across the broader Atlantic Ocean (AO), North Atlantic Ocean (NAO), and South Atlantic Ocean (SAO).

Reference	Domain	Deposition (Tg yr^{-1}) Partial Deposition		Total Deposition
Duce et al. (1991)	NAO	220		244
	SAO	24		
Prospero et al. (1996)	NAO	220		225
	SAO	5		
Ginoux et al. (2001)	NAO	184		204
	SAO	20		
Zender et al. (2003)	NAO	178		207
	SAO	29		
Gaiero et al. (2003)	SAO - Patagonian	30		
Luo et al. (2003)	NAO	230		260
	SAO	30		
Ginoux et al. (2004)	NAO	161		181
	SAO	20		
Tegen et al. (2004)	NAO	259		294
	SAO	35		
Kaufman et al. (2005)	20°S - 30°N	190		
Jickells et al. (2005)	NAO	193.5		211.5
	SAO	18		
Johnson et al. (2010)	SAO - Patagonian	22		
Mahowald et al. (2010)	NAO	276		311.8
	SAO	35.8		
Foltz (2014)	(0°-25°N)	224		
Kim et al. (2014)	(90°W–17°W, 0°N–35°N)	GOCART: GISS: SPRINTARS:	349 196 105	

		ECHAM5: HadGEM2:	158 70	
Yu et al. (2015)	10°S - 30°N	154		
Yu et al. (2019)	5°S - 35°N	CALIOP: CALIOP-MODIS: CALIOP-MISR: CALIOP-IASI:	151.6 221.5 168 136	
Kok et al. (2023)	NAO	230		316
	SAO	86		
The present study	NAO	243.98 ± 23.89		274.79 ± 31.64
	SAO	30.81 ± 10.49		

Figure ~~17~~ 10 shows the comparison between the documented dust deposition estimates (Table ~~8~~7) and our estimates of dust deposition across the broader Atlantic Ocean (Fig. ~~17a~~10a), North Atlantic Ocean (Fig. ~~17b~~10b), and South Atlantic Ocean (Fig. ~~17c~~10c). Overall, on the basis of CALIOP observations between 12/2006 and 11/2022 the annual-mean deposited dust into the broader Atlantic Ocean is estimated 274.79 ± 31.64 Tg yr^{-1}, of which 243.98 ± 23.89 Tg yr^{-1} of dust is deposited across the North Atlantic Ocean and 30.81 ± 10.49 Tg yr^{-1} of dust is deposited across the South Atlantic Ocean. These satellite-derived estimates of dust deposition lie within the much larger documented range of dust deposition rates (Table 7), varying by a factor of two and ranging from 181 Tg yr^{-1} (Ginoux et al., 2004) to 316 Tg yr^{-1} (Kok et al., 2023) for the case of the broader Atlantic Ocean, by a factor of five ranging ~~and~~ from 70 to 349 Tg yr^{-1} for the case of the North Atlantic Ocean (Kim et al., 2014), and by a factor of seventeen ranging ~~and~~ from 5 Tg yr^{-1} (Prospero et al., 1996) to 86 Tg yr^{-1} for the case of the South Atlantic Ocean (Kok et al., 2023). More specifically, on a basis of average of all documented dust deposition estimates ~~(Table 8), the various approaches~~by previous studies (Table 7) yield annual dust deposition of 245.43 ± 48.16 Tg yr^{-1} into the broader Atlantic Ocean, 194.30 ± 59.39 Tg yr^{-1} into the North Atlantic Ocean or Tropical Atlantic Ocean, and 29.57 ± 19.68 Tg yr^{-1} into the South Atlantic Ocean. The present study reports ~~The apparent~~ larger quantified dust deposition estimates ~~of our study~~ with respect to the average of all documented dust deposition estimates, of 29.36 Tg yr^{-1} (11.96%) across the broader Atlantic Ocean, of 49.68 Tg yr^{-1} (25.57%) across the North Atlantic Ocean, and of 1.24 Tg yr^{-1} (4.21%) across the South Atlantic Ocean. However, the dust deposition estimates of our study fall well within the variability of the reported dust deposition outcomes, within one standard deviation. These satellite-derived estimates of dust deposition are rather promising, given that the documented quantifications of dust deposition used ~~as~~ in the inter~~cross-evaluation~~comparison framework were performed over different time spans and spatial scales, the significant variability in model representations of emission and transport processes which are highly heterogeneous in both space and time, the parameterizations of the vertical structure of dust in the atmosphere and of dry and wet dust deposition, the substantial disparity in the size range, distribution, and density of dust in model simulations, and the different utilized satellite-based sensors and applied techniques.

(a) Broader Atlantic Ocean

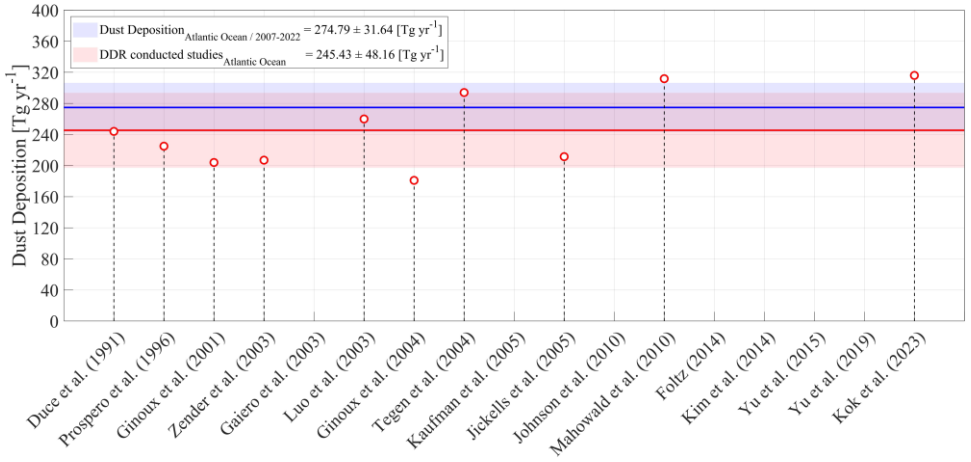

(b) North Atlantic Ocean or Tropical Atlantic Ocean

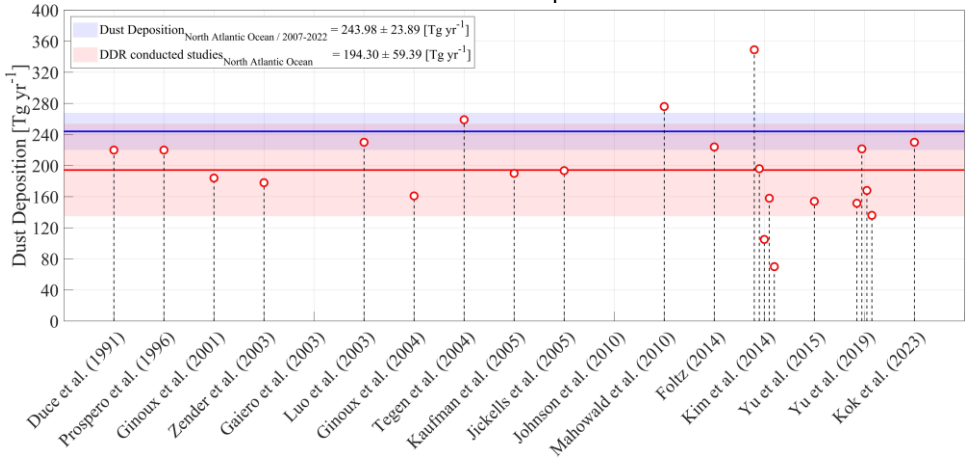

(c) South Atlantic Ocean

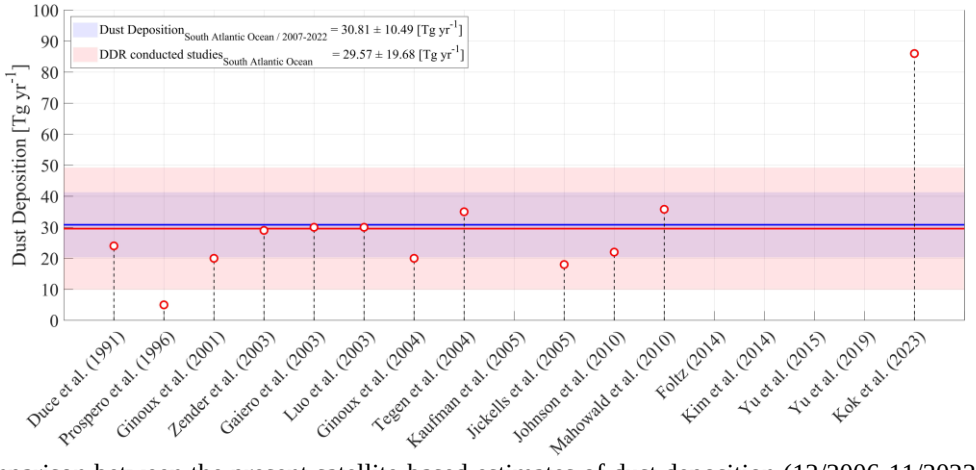

Figure ~~17~~10: Comparison between the present satellite-based estimates of dust deposition (12/2006-11/2022 average) across (a) the broader Atlantic Ocean (AO), (b) North Atlantic Ocean (NAO), and (c) South Atlantic Ocean (SAO) with documented

estimates of dust deposition. In each sub-figure, the horizontal blue and red lines correspond to the EO-based long-term mean dust deposition and the reported in relevant scientific studies mean dust deposition, respectively, while the light blue and light red shaded enveloped areas correspond to their standard deviation. The open circles in red colour provide the quantified dust deposition within the Atlantic Ocean region reported by relevant studies.

3.4 EO-based Dust Deposition Rate vs respective ESM results

The present section aims to intercompare the EO-based dust deposition rate products and estimates of dust deposition provided by Earth System Models (ESM). The objective of the comparison lies in identifying common dust spatial and seasonal patterns, addressing whether the EO-based dust deposition rate product shares similar characteristics in terms of spatio-temporal variability with model-based deposition estimates, implemented in AeroVal (https://aeroval.met.no/; last access: 21 January 2025). AeroVal is a web-based platform, developed at the Norwegian Meteorological Institute, designed for the evaluation of climate and air quality models. The platform employs the pyaerocom library (a successor of AeroCom evaluation and visualization tool) to collocate model data with observations from a variety of sources, including ground-based observation networks (EBAS, EEA, AERONET) and satellites (MODIS, AATSR etc). AeroVal allows for the computation of statistics, such as biases and correlations, and provides an interactive web interface to facilitate easy exploration of data, models intercomparison, and evaluation statistics. It is utilized in several projects, including among others, the CMIP (Mortier et al., 2020), AeroCom (e.g. Gliß et al., 2021), CAMS, and EMEP (https://aeroval.met.no/pages/evaluation/?project=domos-paper; last visit: 20/05/2025). The comparison is performed for only one year of 2020, however we believe that the presented AeroVal consistency check between EO-based and model simulated dust AOD and deposition rates for 2020 provides a good indication of reasonable data correspondence.

As an initial step, the EO-based atmospheric dust product of the ESA-LIVAS climate data record in terms of DOD at 532 nm is compared against AErosol RObotic NETwork (AERONET; https://aeronet.gsfc.nasa.gov/; last access: 3 January 2025; Holben et al., 1998) coarse-mode AOD optical product derived via the Spectral Deconvolution Algorithm (SDA; Eck et al., 1999; O'Neill et al., 2001a, b, 2003) as well as against DOD at 550 nm from the models. This step is applied since the capacity of the EO-based climate data record to provide the spatiotemporal variability of the atmospheric dust conditions with high accuracy is a crucial cornerstone for accordingly quantitatively and qualitatively quantifying the dust deposited component across the dust transport pathways into the ocean. More specifically, since the accuracy of dust deposition calculations relies on the accuracy of the estimates of the dust load in the atmosphere, DODs from LIVAS and EMEP, EC-Earth3, and MONARCH models are as a first-step evaluated against AERONET coarse-mode AOD (Dubovik et al., 2006) and in addition intercompared in AeroVal. The coarse-mode AOD was selected for the evaluation since it ensures a more consistent dust signal, minimizing contamination from fine-mode aerosols such as biomass burning or anthropogenic pollution, though it may underestimate the total dust AOD by ~20-30% (Mamouri and Ansmann, 2014). Note that while model results are produced at a daily resolution, the EO-based DOD and DDR climate data records are provided in the framework of the study at seasonal temporal resolution. As a first approach, all three months within a season are assigned the seasonal value, i.e. the seasonal

mean, in AeroVal intercomparison. It should be emphasized that implementation of AERONET coarse-mode AODs may underestimate the total dust AERONET (fine- and coarse-mode) by ~20-30% (Mamouri and Ansmann, 2014). Accordingly, the AeroVal tool is used for consistency checks by comparing the EO-based DDR climate data record with simulation results from three ESMs, i.e. EMEP MSC-W (hereafter EMEP; Sect.2.1.4), EC-Earth3-Iron (EC-Earth3; Sect.2.1.3), and MONARCH (Sect.2.1.5).

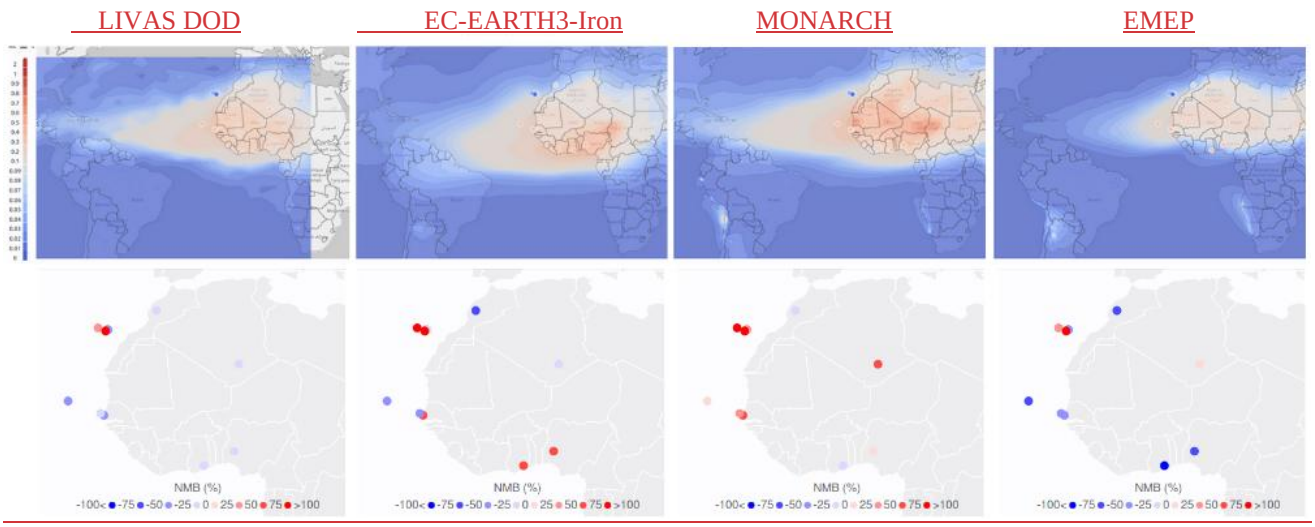

Figure 11: Yearly mean DOD (upper panels) and Normalized Mean Bias with respect to AERONET coarse-mode AOD (lower panels) for LIVAS, EC-Earth3, MONARCH, and EMEP for the year 2020. On the upper maps, AERONET data is also presented by the circles.

The maps of yearly mean DOD from LIVAS product and simulated by EC-Earth3, EMEP, and MONARCH model presented in Figure 11 (upper panels), show similar patterns of spatial distribution, representing the emissions of dust in the African deserts and its westward outflow over the Atlantic Ocean. EC-Earth3 simulates the largest values of DOD, followed by MONARCH, LIVAS, and EMEP. The lower panels in Figure 11 show yearly Normalized Mean Biases of LIVAS and modelled DOD with respect to AERONET coarse-mode AOD. The observations with acceptable time coverage (over 50%) within LIVAS estimated area were available at twelve AERONET sites: six continental and six sites west of the African coast (i.e. on Tenerife, Cabo Verde, and La Palma). LIVAS DOD is around 20-30% lower compared to AERONET coarse-mode AOD at the continental sites and in Cabo Verde while it is 47% higher on La Palma. For the sites on Tenerife, we see both under- and over- estimation by LIVAS. LIVAS DOD is higher than AERONET coarse-mode AOD at the mountain sites Izaña (2410 m above sea level) by 44% and at Teide (3555m above sea level) by a factor of 5.5, where the greatest overestimation is for in October through December months (the only available observations at Teide). On the other hand, LIVAS

underestimates by around 45% observations at La Laguna and Santa Cruz de Tenerife (observations only available for January-June and December), with the largest bias in June-July.

The largest difference among the models is that MONARCH, and especially EC-Earth3, simulate larger dust emissions from the Sahel desert compared to EMEP. DOD from MONARCH is the closest to AERONET coarse-mode AOD south of Sahel; EC-Earth3 overestimates it by 60-70%, while EMEP underestimates by 70-80%. The agreement is better between EMEP DOD and AERONET at the site located in Sahara, whereas EC-Earth3 underestimates and MONARCH overestimates AERONET coarse-mode AOD at this site, respectively. MONARCH overestimates AERONET coarse-mode AOD at the African coastal sites and the islands. At the low-altitude sites on Tenerife and Cabo Verde, DOD from LIVAS and EC-Earth3 are closer to AERONET, while EMEP underestimates and MONARCH overestimates those. LIVAS and all three ESMs are biased rather high at all high-elevations AERONET sites (i.e., Tenerife and La Palma).

The monthly variation of EO-based DOD and modelled DOD vs AERONET coarse-mode AOD at all considered sites are shown in Figure 12 (left panel). As it is described above, the EO-based DOD at 523 nm and ESM dust outputs include both the fine-mode and coarse-mode dust components while the AERONET AOD at 550 nm component represents the coarse-mode fraction of dust, which probably contributes to increasing comparison uncertainties.

Figure 12: Monthly series (left) comparing the EO-based DOD, the simulated by the models (EC-EARTH3-Iron, MONARCH, and EMEP), and the AERONET coarse-mode AOD at all the sites shown in Fig. 11; and the monthly series for Cabo Verde (right), for the year 2020.

The monthly timeseries of LIVAS and modelled DOD, compared on Figure 12, reflect the seasonality in African dust emissions, transport and deposition. Figure 12-left panel shows that averaged over the 12 AERONET sites, the observed temporal pattern of coarse dust AOD is reasonably well reproduced by the models (with EMEP and MONARCH being consistently biased low and high, respectively, while EC-Earth3-Iron shifting from overestimation in the cold season to underestimation in the warm season). The monthly profile from LIVAS lies well within the modelled spread of monthly DODs, though it looks smoother because seasonal mean DOD was used for all three months within the season. LIVAS tends to underestimate DOD for January-February, which is particularly pronounced at two sites in Tenerife (La Laguna and Santa

Cruz), which could to some extent be explained by using DJF seasonal mean. Similar to EC-Earth3-Iron and EMEP, LIVAS also underestimates in June-July (which is mostly driven by underestimation beyond the main dust emission regions, i.e. at the coastal and island-type sites). Figure 12 (right panel) compares the monthly time series of EO-based and modelled DOD and coarse-mode AOD at Cabo Verde - the location, representative of the dust plume transported westward off the African deserts over the subtropical eastern North Atlantic. LIVAS DOD variation is very close to those simulated by EC-Earth3-Iron and EMEP, underestimating AERONET data, especially in June 2020. The overall evaluation statistics (bias and spatial correlation) for LIVAS and modelled DOD with respect to AERONET coarse-mode AOD are summarized in Table 8.

Table 8. Overall evaluation statistics in terms of normalized bias and spatial correlation for the LIVAS DOD at 532 nm and the modelled DOD with respect to AERONET coarse-mode AOD (SDA V3 L2), for the year 2020.

	LIVAS DOD	EC-Earth3-Iron	MONARCH	EMEP
NMB (%)	-22.9	8.1	32.5	-47.3
R-Space	0.95	0.76	0.87	0.55

In further comparison, we assess models' results against the LIVAS DOD at 532 nm data. The comparison is done on the monthly basis at 2°x2° grid cells with available LIVAS DOD at 532 nm data. Figure 13 presents the maps of normalized mean biases with respect to LIVAS for EC-Earth3, MONARCH, and EMEP. Over the African deserts, MONARCH (which includes dust particles up to 20 μm in diameter). EC-Earth3 and EMEP have relatively small biases (especially EC-Earth3), i.e. positive in eastern-southeastern parts of Sahara and slightly negative in central/western parts. MONARCH also simulates DOD higher than LIVAS over the subtropical North Atlantic and in the east of South Atlantic Ocean. EC-Earth3 has quite small (positive and negative respectively) biases compared to LIVAS DOD in the grid cells over North Atlantic Ocean, while overestimating over its equatorial part and South Atlantic Ocean. EMEP results are quite close to LIVAS DOD over the Atlantic north of equator, but underestimates over the South Atlantic Ocean. It should be noted that due to a rather simplified description of AOD in the EMEP model, the uncertainties in DOD modelling are associated with both dust three-dimensional concentrations and assumptions for dust specific extinction.

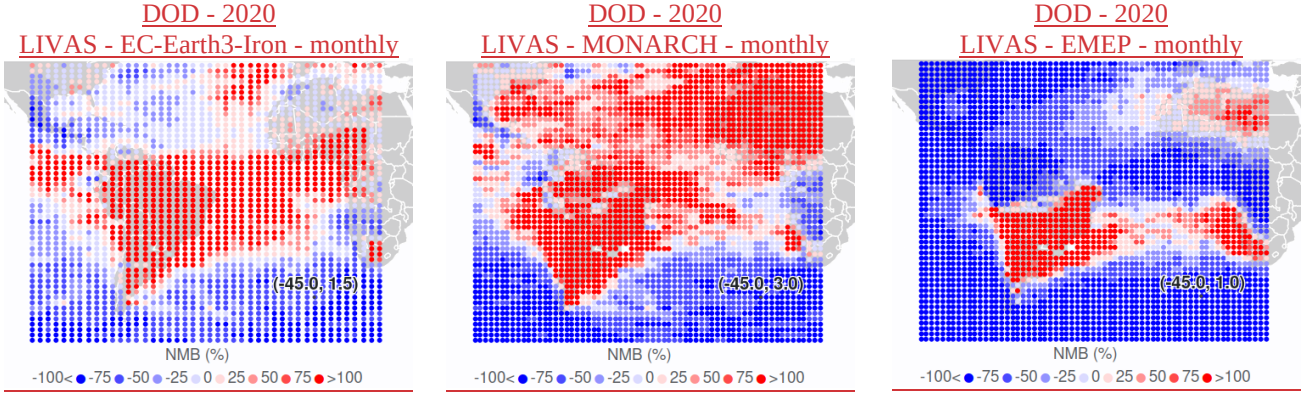

Figure 13: Normalized mean bias of modelled DOD compared with LIVAS data for EC-Earth3 (left), MONARCH (middle), and EMEP (right).

The maps of yearly mean dust total (dry and wet) deposition rate established on the basis of LIVAS and simulated with the EC-Earth3-Iron, EMEP, and MONARCH models are shown in Figure 14. The general pattern of dust deposition over the Atlantic Ocean is quite similar, though the models simulated dust deposition rates smaller compared to the EO-based dust deposition rate estimates, with MONARCH results being closer to those and EC-Earth3-Iron providing the lowest dust deposition rates in terms of magnitude. Figure 15 presents the maps of relative biases for dust deposition rate from the three ESMs with respect to the estimates of the present study. Along the dust plume core, EC-Earth3-Iron has the largest negative bias (mostly around -65 to -80%), EMEP mostly underestimates (with bias varying mostly between 30 and 60%), while MONARCH has the lowest bias (an order of 15-40%). Zonally, the models' biases remain quite similar across the Atlantic Ocean almost as far as the Caribbean Sea, indicating similar east-to-west dust deposition gradients. However, over the Caribbean Sea, the models' underestimation of LIVAS dust deposition increases. To the north and south of the main dust plume, the models' results show smaller negative and positive biases with respect to LIVAS dust deposition, respectively.

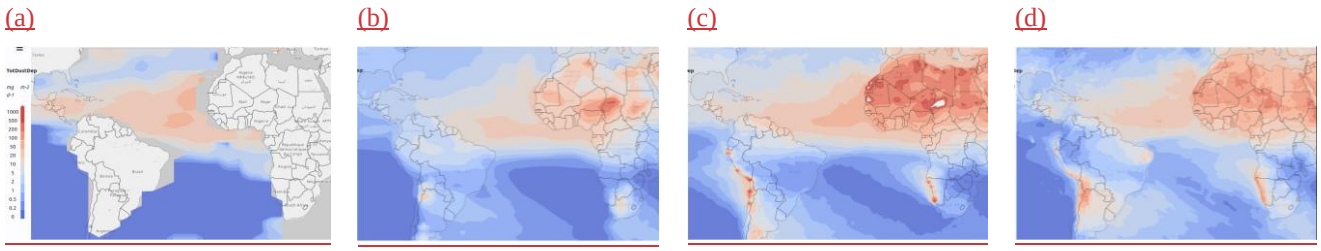

Figure 14: Yearly mean dust deposition rate (mg m^{-2} day^{-1}) from LIVAS (a) and simulated with EC-Earth3-Iron (b), MONARCH (c), and EMEP (d). Year: 2020.

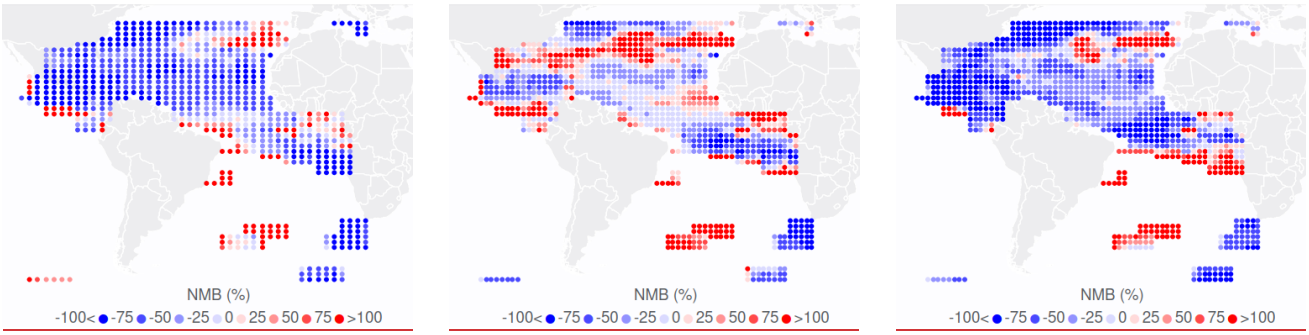

Figure 15: Yearly mean bias (mg m^{-2} day^{-1}) for dust total deposition for EC-Earth3_Iron (a), MONARCH (b), and EMEP (c) with respect to LIVAS data. Year: 2020. Here, the empty grid cells are those without LIVAS data (corresponding to zeroes in Fig. 15).

The timeseries in Figure 16 compare profiles of DOD (a) and deposition rate (b), simulated by the three models and those produced by LIVAS. The profiles are the averages over all of 2°x2° grid cells with LIVAS data. The EMEP model shows better agreement with LIVAS DOD, slightly underestimating it. EC-Earth3-Iron overestimates LIVAS DOD for January to March, showing quite good correspondence otherwise. MONARCH simulated DOD higher than LIVAS through the year. For dust deposition, no one of the models manage to reproduce LIVAS summer maximum, with EC-Earth3-Iron underestimating LIVAS the most and simulating winter/autumn maxima instead. The reported higher dust deposition by LIVAS compared to ESMs relates, among others, to the historic "Godzilla" dust intrusion over the Atlantic Ocean in June 2020, with atmospheric dust load substantially underestimated by dust models (Yu et al., 2021), with dust removal processes more efficiently removing dust layers from the atmosphere (Yu et al., 2019; Kim et al., 2014). For the other seasons, MONARCH overestimates LIVAS dust deposition, while EMEP and Earth3-Iron dust deposition rates are quite close to LIVAS.

(a)

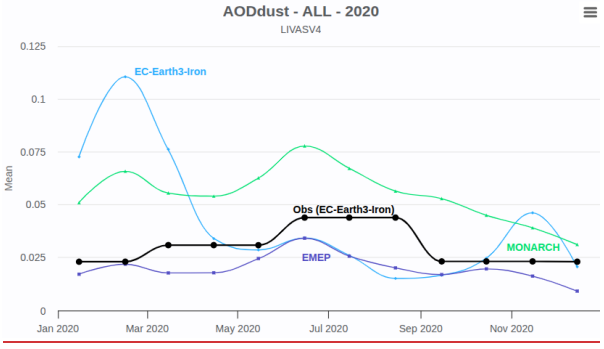

(b)

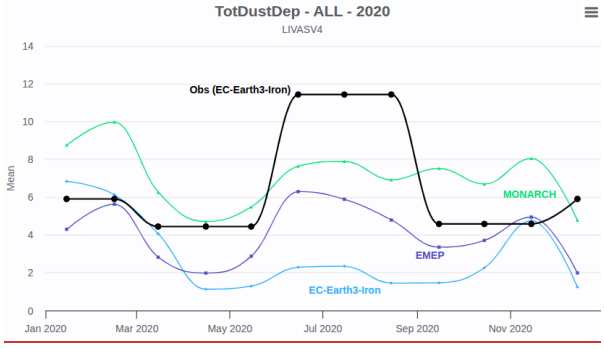

Figure 16: Monthly series of EO-based DOD and dust total deposition (Obs, black line), EC-Earth3, MONARCH, and EMEP (models' results are collocated with LIVAS data at grid cells of 2°x2°).

The overall evaluation statistics (bias and spatial correlation) for model simulated DOD and deposition rate with respect to LIVAS data are summarized in the heatmaps (Fig. 17). Those are yearly mean statistics, averaged over all grid cells of 2°x2° where LIVAS data available. The spatial correlation between the models and LIVAS is quite high (between 0.7 and 0.94). The EMEP model underestimates both DOD and deposition by about 35%, which partly could be due to somewhat lower African dust emissions compared with LIVAS (as seen from comparison with AERONET coarse-mode AOD (Figs. 11-12). EC-Earth3-Iron overestimates by 42% LIVAS DOD, but underestimates by 55% LIVAS dust deposition. The largest positive bias with respect to LIVAS data is seen for DOD from MONARCH (81%), while its dust deposition is quite close to that from LIVAS.

(a) (b)

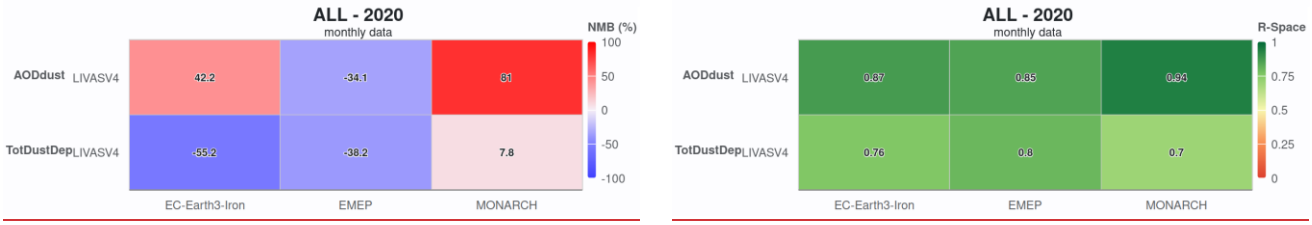

Figure 17: Summary statistics (relative bias, NMB% - Fig. 17.a, and spatial correlation, R-Space - Fig. 17.b) of models' comparison with LIVAS DOD and total deposition.

~~7~~4 Summary and conclusions

Atmospheric dust deposition across the open ocean fertilizes marine ecosystems with essential nutrients (e.g., N, P, SiO_2, Fe), regulating phytoplankton growth and modulating marine productivity, ocean colour, the global carbon cycle, eventually affecting weather and climate. However, despite the vital role of atmospheric deposited lithogenic material for the ocean biogeochemistry and for dust cycle-related processes, the amount of atmospheric dust that is actually deposited into the open ocean remains poorly quantified. Significant challenges related to the complexity of oceanographic research prevent long-term, high-coverage in-situ measurements, while numerical model simulations rely on highly parameterized dust processes and variable assumptions, with few constraints.

This study provides and discusses a novel satellite-based climate data record of dust deposition rate estimates (mg m^{-2} day^{-1}) for the broader Atlantic Ocean region, confined between 60°S and 40°N, at 5° (zonal) × 2° (meridional) spatial resolution,

seasonal-mean temporal resolution, and for the period 12/2006–11/2022. Dust deposition rates are derived from atmospheric dust fluxes using two central enabling components: (1) the four-dimensional structure of dust aerosols in the atmosphere in terms of mass concentration (μg m^{-3}) provided by the ESA-LIVAS climate data record, established based on the one-step POLIPHON technique applied to CALIPSO-CALIOP observations at 532 nm, and (2) the eastward and northward wind components (m s^{-1}) provided by the ECMWF ERA5 reanalysis. Synergistic implementation of the two datasets provides the capacity to estimate dust mass fluxes (mg m^{-2} day^{-1}) into the ocean by differentiating zonal and meridional input/output dust fluxes across conceptual cuboid atmospheric columns, and on the basis of the mass conservation principle.

To verify accuracy, ensure reliability, and quantify uncertainties of the satellite-based dust deposition rate estimates, sediment-trap observations were used as reference datasets. Despite inherent uncertainties and methodological discrepancies, good agreement is found between satellite-based estimates and sediment-trap data (slope 0.85, intercept 9.49 mg m^{-2} day^{-1}, Pearson correlation coefficient 0.79), although the satellite-based estimates tend to overestimate in situ observations (mean bias 5.42 mg m^{-2} day^{-1}, relative bias 19.82%, RMSE 30.3 mg m^{-2} day^{-1}). Since the capacity of the ESA-LIVAS climate data record to accurately provide the spatiotemporal variability of the atmospheric dust is crucial to quantify the dust deposited component across the dust transport pathways over the open ocean, the DOD at 532 nm product was additionally evaluated against AERONET SDA coarse-mode AOD at 500 nm, showing high quality (normalized mean bias 0.4%, Pearson's correlation coefficient 0.77). AeroVal intercomparisons between the satellite-based dust deposition product and MONARCH, EMEP MSC-W, and EC-Earth3-Iron ESMs for the year 2020 revealed strong consistency, with normalized mean biases of 9.2%, -50.2%, and 38.1%, and Pearson's correlation coefficient of 0.87, 0.85, and 0.93, respectively. Cross-comparison of dust deposition rates showed reasonable agreement, within a factor of two. Overall, the satellite product reliably reproduces spatiotemporal dust deposition patterns across the Atlantic Ocean, aligning with sediment-trap measurements and ESM outputs, while capturing seasonal dust source activation and migration of transport pathways.

The study reports annual-mean amount of dust deposition into the broader Atlantic Ocean of 274.79 ± 31.64 Tg yr^{-1}, of which 243.98 ± 23.89 Tg yr^{-1} of dust is deposited into the North Atlantic Ocean and 30.81 ± 10.49 Tg yr^{-1} of dust is deposited into the South Atlantic Ocean, each year. Seasonally, deposition peaks in summer (93.10 ± 11.65 Tg, JJA) and is lowest in autumn (40.62 ± 11.44 Tg, SON), with intermediate levels in spring (77.3 ± 19.93 Tg) and winter (63.78 ± 12.03 Tg). Comparison of the satellite-based estimates of dust deposition (12/2006-11/2022 average) with the average of documented model-based and satellite-based estimates of dust deposition over the broader Atlantic Ocean, the North Atlantic Ocean, and the South Atlantic Ocean is performed. The intercomparison reveals larger dust deposition estimates of our satellite-based dust deposition product with respect to the average of all documented dust deposition estimates, of 29.36 Tg yr^{-1} (11.96%) across the broader Atlantic Ocean, of 49.68 Tg yr^{-1} (25.57%) across the North Atlantic Ocean, and of 1.24 Tg yr^{-1} (4.21%) across the South Atlantic Ocean, falling though well within each-others variability, within one standard deviation. It should be noted that the EO-based outcomes on the basis of observations between 12/2006 and 11/2022 reveal a negative statistically significant trend in the Atlantic Ocean dust deposition, characterized by slope -13.35 Tg yr^{-1} and offset 306.97 Tg.

The satellite-based dust deposition climate data record is considered unique with respect to a diverse range of potential applications. These include filling spatial and temporal gaps in sediment-trap observational datasets thus extending their limited coverage, evaluating model simulations, and elucidating physical processes involved in the dust cycle from emission to transport and eventually deposition. The dust deposition estimates can further be used to address major knowledge gaps in marine sciences and advance our capacity to better understand, describe and predict complex and poorly understood processes including the impact of deposited dust nutrients on the sustainability of the Atlantic Ocean biogeochemistry, and in this way to enhance science-based effective adaptation and mitigation strategies to preserve the oceans under the ongoing climate change.~~Deposition of atmospheric dust across the surface of the open ocean fertilizes marine ecosystems with essential nutrients, such as nitrogen (N), phosphorus (P), silica (SiO_2), and iron (Fe), critical for regulating phytoplankton growth, and consequently modulating marine productivity, ocean colour, the global carbon cycle through the ocean's capacity to absorb CO_2, weather and eventually climate. However, despite the vital role of atmospheric deposited lithogenic material for the ocean biogeochemistry and for understanding physical processes linked to the dust cycle, the amount of atmospheric dust that is actually deposited into the open ocean is still not well quantified. Numerous significant challenges inherent to the complex nature of oceanographic research hamper the feasibility of establishing long-term and continuous in-situ measurements of high spatial coverage over extensive geographical areas and temporal periods while numerical model simulations depend on highly parameterized representations of dust processes and on highly variable approaches and assumptions, including among others consideration on meteorology, the dust particle size distribution, and temporal periods and domains, with few constraints.~~

~~This study provides a novel satellite based climate data record (CDR) of dust deposition rate (mg/m^2d) estimates for the broader area encompassing the dust emission sources of West Africa and South America with focus on the Atlantic Ocean, the Caribbean Sea, and the Gulf of Mexico regions, confined between latitudes 60°S to 40°N and of 5° (zonal) x 2° (meridional) spatial resolution, in a seasonal-mean temporal resolution, and of sixteen-year temporal coverage, extending between 12/2006 and 11/2022. The product of dust deposition rate estimates into the ocean is established on the basis of atmospheric dust fluxes over the ocean and relies on two central enabling components. First, on the 4D structure of dust aerosols in the atmosphere in terms of mass concentration ($\mu g/m^3$), provided by the ESA LIVAS CDR, established through the one-step POLIPHON technique applied to CALIPSO-CALIOP aerosol observations at 532 nm. Second, on the eastward and northward components of wind (m/s), provided at different pressure levels by the ECMWF reanalysis dataset ERA5. Synergistic implementation of the two datasets provides the capacity to estimate dust mass fluxes ($\mu g/m^2s$) into the ocean by means of differentiation of the zonal and meridional dust input/output atmospheric dust mass fluxes through the areas of conceptual cuboid atmospheric columns lying over the ocean surface and on the basis of the mass conservation hypothesis.~~

~~Towards verifying the accuracy, ensuring the reliability, and quantifying the uncertainties of the satellite-based estimations of dust deposition rate, includes implementation of sediment trap observations of dust deposition fluxes as reference datasets. Despite the several sources of uncertainties and the several methodological factors driving the observed discrepancies, the satellite-based dust deposition rate product and the sediment trap observations, a rather good agreement between the two datasets (slope of 0.85, intercept of 9.49 $mg/m^2/day$, and Pearson correlation coefficient 0.79) is revealed, though the general~~

trend of satellite-based dust deposition is to overestimate those from the in-situ provided observations (mean bias of 5.42 mg/m²/day, relative bias of 19.82%, and RMSE of 30.3 mg/m²/day). In addition, the EO based atmospheric dust product of the ESA LIVAS CDR in terms of DOD at 532 nm is evaluated against AERONET SDA coarse mode AOD, as a significant intermediate step since the capacity of the LIVAS to accurately provide the spatiotemporal variability of the atmospheric dust conditions is crucial towards quantification of the dust deposited component across the dust transport over the ocean. The evaluation activities performed in the framework of AeroVal between the two datasets reveals the high quality of the ESA-LIVAS atmospheric dust product, characterized by Normalized Mean Bias (NMB) of 0.4% and Pearson's correlation coefficient of 0.77. Accordingly, AeroVal intercomparison of the EO based dust deposition product against the atmospheric dust outputs in terms of optical depth and the corresponding dust deposition fields provided by MONARCH, EMEP MSC-W, EC-Earth3-Iron ESMs for the year 2020 is performed. The intercomparison reported high agreement between the ESA LIVAS atmospheric dust product and EC-Earth3-Iron (NMB of 9.2%, Pearson's correlation coefficient of 0.87), EMEP (NMB of -50.2%, Pearson's correlation coefficient of 0.85), and MONARCH (NMB of 38.1%, Pearson's correlation coefficient of 0.93), corroborating the high quality of the ESA LIVAS atmospheric dust product. In terms of the AeroVal performed cross-comparison between the satellite-based estimates of dust deposition rate and the ESM dust deposition outputs relatively good agreement between the satellite-based estimates of dust deposition and EC-Earth3-Iron (NMB of -68.9%, Pearson's correlation coefficient of 0.69), EMEP (NMB of -57.1%, Pearson's correlation coefficient of 0.75), and MONARCH (NMB of -25%, Pearson's correlation coefficient of 0.66) is revealed, with the satellite-based estimates within a factor of 2 from the corresponding ESMs dust deposition fields. Overall, it is notable that the satellite-based dust deposition rate product consistently reproduces the dust deposition patterns recorded by the sediment traps installed and operated across the broader Atlantic Ocean, with a positional accuracy and magnitude generally within a factor of 2 compared to sediment trap measurements, and in addition the spatiotemporal characteristics of ESMs dust deposition as demonstrated through the AeroVal intercomparison. The performed evaluation reveals the capacity of the satellite-based product to quantitatively provide the amount of dust deposited into the broader Atlantic Ocean, consistent with the seasonal activation of the dust source regions, revealing the seasonal four-dimensional migration of dust transport pathways, and in good agreement with features reported by sediment-traps' in-situ measurements of lithogenic material and ESMs.

The annual mean amount of dust deposition into the broader Atlantic Ocean is quantified at 274.79 ± 31.64 Tg, of which 243.98 ± 23.89 Tg of dust is deposited into the North Atlantic Ocean and 30.81 ± 10.49 Tg of dust is deposited into the South Atlantic Ocean, each year. With respect to the intrannual seasonal variability, dust deposition into the ocean is generally highest in summer and lowest in autumn, estimated at 93.10 ± 11.65 Tg and 40.62 ± 11.44 Tg, for JJA and SON respectively. In spring and winter seasons, intermediate activity of dust deposition into the ocean is observed, estimated to 77.3 ± 19.93 Tg and 63.78 ± 12.03 Tg, respectively. Furthermore, comparison of the satellite-based estimates of dust deposition (12/2006-11/2022 average) with the average of documented model-based and satellite-based estimates of dust deposition over the broader Atlantic Ocean (245.43 ± 48.16 Tg yr^{-1}), North Atlantic Ocean (194.30 ± 59.39 Tg yr^{-1}), and South Atlantic Ocean (29.57 ± 19.68 Tg yr^{-1}) is performed. The intercomparison reveals larger dust deposition estimates of our satellite-based dust

deposition product with respect to the average of all documented dust deposition estimates, of 29.36 Tg yr^{-1} (11.96%) across the broader Atlantic Ocean, of 49.68 Tg yr^{-1} (25.57%) across the North Atlantic Ocean, and of 1.24 Tg yr^{-1} (4.21%) across the South Atlantic Ocean, falling though well within each others variability, within one standard deviation. It should be noted that the performed intercomparisons serves more as cross-assessment of the satellite-based dust deposition estimates rather than as a rigorous evaluation since the majority of the reported estimates rely on highly variable approaches, sensors, models, assumptions, parametrizations, meteorology, temporal periods, and domains.

The satellite-based dust deposition climate data record is considered unique with respect to a diverse range of potential applications. These include filling spatial and temporal gaps in sediment trap observational datasets thus extending their limited coverage, evaluating model simulations, and elucidating physical processes involved in the dust cycle from emission to transport and eventually deposition. The dust deposition estimates can further be used to address major knowledge gaps in marine sciences and advance our capacity to better understand, describe and predict complex and poorly understood processes including the impact of deposited dust nutrients on the sustainability of the Atlantic Ocean biogeochemistry, and in this way to enhance science-based effective adaptation and mitigation strategies to preserve the oceans under the ongoing climate change.

Data availability

The CALIPSO Level 2 data products are publicly available from the Atmospheric Science Data Center at NASA Langley Research Center (https://earthdata.nasa.gov/eosdis/daacs/asdc, EARTHDATA; last visit: 23/11/2023). The ESA-LIVAS climate data recordCDR in terms of Level 2 and Level 3 pure-dust products (i.e., backscatter coefficient at 532 nm, extinction coefficient at 532 nm, mass concentration profiles and DOD at 532 nm) is available upon personal communication with Emmanouil Proestakis (proestakis@noa.gr) and/or Vassilis Amiridis (vamoir@noa.gr). The data from AERONET can be freely obtained from https://aeronet.gsfc.nasa.gov (last visit: 23/11/2023). The satellite-based dust deposition climate data recordCDR is available through the Zenodo repository: 10.5281/zenodo.14608538. (Proestakis et al., 2025).

Author contributions

Emmanouil Proestakis: Conceptualization, Methodology, Software, Data Curation, Formal analysis. Vassilis Amiridis: Methodology, Supervision, Conceptualization. Carlos Pérez García-Pando: Methodology, Supervision, Conceptualization. Svetlana Tsyro: Software, Formal analysis, Visualization. Jan Griesfeller: Software, Formal analysis, Visualization. Antonis Gkikas: Methodology, Formal analysis, Conceptualization. Thanasis Georgiou: Software. María Gonçalves Ageitos: Software, Methodology, Formal analysis. Elisa Bergas Masso: Software, Methodology, Formal analysis. Stelios Myriokefalitakis: Software, Methodology, Formal analysis. Enza Di Tomaso: Software, Methodology, Formal analysis. Sara Basart: Project

administration. Jan-Berend Stuut: Validation, Investigation, Data Curation. Jerónimo Escribano: Software, Methodology, Formal analysis. Angela Benedetti: Project administration, Supervision, Conceptualization.

Competing interests.

The authors declare that they have no conflict of interest.

Acknowledgements

~~Emmanouil Proestakis acknowledges support by the AXA Research Fund for postdoctoral researchers under the project entitled "Earth Observation for Air-Quality – Dust Fine-Mode (EO4AQ-DustFM)".~~ This research was supported by the Dust Observation and Modelling Study (DOMOS) under ESA contract number 4000135024/21/I-NB. Emmanouil Proestakis acknowledges support by the AXA Research Fund for postdoctoral researchers under the project entitled "Earth Observation for Air-Quality – Dust Fine-Mode (EO4AQ-DustFM)". The support of the scientific project officer Dr Simon Pinnock is gratefully acknowledged. We would like to thank the NASA CALIPSO team and NASA/LaRC/ASDC for making the CALIPSO products available, which have been used to build the LIVAS products, and ESA, who funded the LIVAS project (contract no. 4000104106/11/NL/FF/fk). We thank AERONET (https://aeronet.gsfc.nasa.gov/, last access: 7th of January 2024), and AERONET-Europe for the data collection, calibration, processing, and dissemination. We thank ECMWF for providing fifth-generation ERA5 Reanalysis data and Marenostrum5 support team and Computational Earth Sciences team of BSC for their support in maintaining and using the HPC infrastructure. We would like to thank the anonymous reviewers, who were very helpful and who provided constructive comments that improved the paper.

Financial support

~~EP has been supported by the AXA Research Fund (Earth Observation for Air-Quality – Dust Fine-Mode (EO4AQ-DustFM).~~ CPGP, EBM, MGA, JE and EdT were funded by the ESA-DOMOS contract, and acknowledge the funding received through the AXA-Chair in Sand and Dust Storms. EP has been supported by the AXA Research Fund (Earth Observation for Air-Quality - Dust Fine-Mode (EO4AQ-DustFM). JBS was funded by NWO with the TRAFFIC project 822.01.008 and the ERC with starting grant 311152: DUSTTRAFFIC. MGA acknowledges the support of the BIOTA Spanish I+D+i Grant PID2022-139362OB-I00 funded by MICIU/AEI/10.13039/501100011033 and by ERDF, EU.

References

Abouchami, W., Näthe, K., Kumar, A., Galer, S. J. G., Jochum, K. P., Williams, E., Horbe, A. M. C., Rosa, J. W. C., Balsam, W., Adams, D., Mezger, K., and Andreae, M. O.: Geochemical and isotopic characterization of the Bodélé Depression dust

source and implications for transatlantic dust transport to the Amazon Basin, Earth and Planetary Science Letters, 380, 112–123, https://doi.org/10.1016/j.epsl.2013.08.028, 2013.

Adams, A. M., Prospero, J. M., and Zhang, C.: CALIPSO-Derived Three-Dimensional Structure of Aerosol over the Atlantic Basin and Adjacent Continents, Journal of Climate, 25, 6862–6879, https://doi.org/10.1175/JCLI-D-11-00672.1, 2012.

Adebiyi, A., Kok, J. F., Murray, B. J., Ryder, C. L., Stuut, J.-B. W., Kahn, R. A., Knippertz, P., Formenti, P., Mahowald, N. M., Pérez García-Pando, C., Klose, M., Ansmann, A., Samset, B. H., Ito, A., Balkanski, Y., Di Biagio, C., Romanias, M. N., Huang, Y., and Meng, J.: A review of coarse mineral dust in the Earth system, Aeolian Research, 60, 100849, https://doi.org/10.1016/j.aeolia.2022.100849, 2023.

Adler, R. F., Sapiano, M. R. P., Huffman, G. J., Wang, J.-J., Gu, G., Bolvin, D., Chiu, L., Schneider, U., Becker, A., Nelkin, E., Xie, P., Ferraro, R., and Shin, D.-B.: The Global Precipitation Climatology Project (GPCP) Monthly Analysis (New Version 2.3) and a Review of 2017 Global Precipitation, Atmosphere, 9, 138, https://doi.org/10.3390/atmos9040138, 2018.

Albani, S., Mahowald, N. M., Perry, A. T., Scanza, R. A., Zender, C. S., Heavens, N. G., Maggi, V., Kok, J. F., and Otto-Bliesner, B. L.: Improved dust representation in the Community Atmosphere Model, Journal of Advances in Modeling Earth Systems, 6, 541–570, https://doi.org/10.1002/2013MS000279, 2014.

Alfaro, S. D. and Gomes, L.: Modeling mineral aerosol production by wind erosion: Emission intensities and aerosol size distributions in source areas., J. Geophys. Res., 106, 18075–18084, doi:10.1029/2000jd900339, 2001.

Alldredge, A. L., Granata, T. C., Gotschalk, C. C., and Dickey, T. D.: The physical strength of marine snow and its implications for particle disaggregation in the ocean, Limnology and Oceanography, 35, 1415–1428, https://doi.org/10.4319/lo.1990.35.7.1415, 1990.

Amiridis, V., Wandinger, U., Marinou, E., Giannakaki, E., Tsekeri, A., Basart, S., Kazadzis, S., Gkikas, A., Taylor, M., Baldasano, J. and Ansmann, A.: Optimizing CALIPSO Saharan dust retrievals, Atmos. Chem. Phys., 13(23), 12089–12106, doi:10.5194/acp-13-12089-2013, 2013.

~~Amiridis, V., Wandinger, U., Marinou, E., Giannakaki, E., Tsekeri, A., Basart, S., Kazadzis, S., Gkikas, A., Taylor, M., Baldasano, J., and Ansmann, A.: Optimizing CALIPSO Saharan dust retrievals, Atmos. Chem. Phys., 13, 12089–12106, https://doi.org/10.5194/acp-13-12089-2013, 2013.~~

Amiridis, V., Marinou, E., Tsekeri, A., Wandinger, U., Schwarz, A., Giannakaki, E., Mamouri, R., Kokkalis, P., Binietoglou, I., Solomos, S., Herekakis, T., Kazadzis, S., Gerasopoulos, E., Proestakis, E., Kottas, M., Balis, D., Papayannis, A., Kontoes, C., Kourtidis, K., Papagiannopoulos, N., Mona, L., Pappalardo, G., Le Rille, O. and Ansmann, A.: LIVAS: a 3-D multi-wavelength aerosol/cloud database based on CALIPSO and EARLINET, Atmos. Chem. Phys., 15(13), 7127–7153, doi:10.5194/acp-15-7127-2015, 2015.

Anav, A., Friedlingstein, P., Kidston, M., Bopp, L., Ciais, P., Cox, P., Jones, C., Jung, M., Myneni, R., and Zhu, Z.: Evaluating the Land and Ocean Components of the Global Carbon Cycle in the CMIP5 Earth System Models, https://doi.org/10.1175/JCLI-D-12-00417.1, 2013.

Ansmann, A., Wandinger, U., Rille, O. L., Lajas, D., and Straume, A. G.: Particle backscatter and extinction profiling with the spaceborne high-spectral-resolution Doppler lidar ALADIN: methodology and simulations, Appl. Opt., AO, 46, 6606–6622, https://doi.org/10.1364/AO.46.006606, 2007.

Ansmann, A., Baars, H., Tesche, M., Müller, D., Althausen, D., Engelmann, R., Pauliquevis, T., and Artaxo, P.: Dust and smoke transport from Africa to South America: Lidar profiling over ~~Cape Verde~~Cabo Verde and the Amazon rainforest, Geophysical Research Letters, 36, https://doi.org/10.1029/2009GL037923, 2009a.

Ansmann, A., Tesche ,Matthias, Knippertz ,Peter, Bierwirth ,Eike, Althausen ,Dietrich, MüLLER ,Detlef, and and Schulz, O.: Vertical profiling of convective dust plumes in southern Morocco during SAMUM, Tellus B: Chemical and Physical Meteorology, 61, 340–353, https://doi.org/10.1111/j.1600-0889.2008.00384.x, 2009b.

Ansmann, A., Tesche, M., ~~Groß~~Gross, S., Freudenthaler, V., Seifert, P., Hiebsch, A., Schmidt, J., Wandinger, U., Mattis, I., Müller, D. and Wiegner, M.: The 16 April 2010 major volcanic ash plume over central Europe: EARLINET lidar and AERONET photometer observations at Leipzig and Munich, Germany, Geophysical Research Letters, 37(13), doi:10.1029/2010GL043809, 2010.

Ansmann, A., Petzold, A., Kandler, K., Tegen, I., Wendisch, M., Müller, D., Weinzierl, B., Müller, T. and Heintzenberg, J.: Saharan Mineral Dust Experiments SAMUM–1 and SAMUM–2: what have we learned?, Tellus B: Chemical and Physical Meteorology, 63(4), 403–429, doi:10.1111/j.1600-0889.2011.00555.x, 2011.

Ansmann, A., Seifert, P., Tesche, M. and Wandinger, U.: Profiling of fine and coarse particle mass: case studies of Saharan dust and Eyjafjallajökull/Grimsvötn volcanic plumes, Atmospheric Chemistry and Physics, 12(20), 9399–9415, doi:https://doi.org/10.5194/acp-12-9399-2012, 2012.

Ansmann, A., Mamouri, R.-E., Hofer, J., Baars, H., Althausen, D. and Abdullaev, S. F.: Dust mass, cloud condensation nuclei, and ice-nucleating particle profiling with polarization lidar: updated POLIPHON conversion factors from global AERONET analysis, Atmos. Meas. Tech., 12(9), 4849–4865, doi:10.5194/amt-12-4849-2019, 2019.

Aslanoğlu, S. Y., Proestakis, E., Gkikas, A., Güllü, G., and Amiridis, V.: Dust Climatology of Turkey as a Part of the Eastern Mediterranean Basin via 9-Year CALIPSO-Derived Product, Atmosphere, 13, 733, https://doi.org/10.3390/atmos13050733, 2022.

Aumont, O., Ethé, C., Tagliabue, A., Bopp, L., and Gehlen, M.: PISCES-v2: an ocean biogeochemical model for carbon and ecosystem studies, Geoscientific Model Development, 8, 2465–2513, https://doi.org/10.5194/gmd-8-2465-2015, 2015.

Avila, A., Queralt-Mitjans, I., and Alarcón, M.: Mineralogical composition of African dust delivered by red rains over northeastern Spain, Journal of Geophysical Research: Atmospheres, 102, 21977–21996, https://doi.org/10.1029/97JD00485, 1997.

Baars, H., Kanitz, T., Engelmann, R., Althausen, D., Heese, B., Komppula, M., Preissler, J., Tesche, M., Ansmann, A., Wandinger, U., Lim, J.-H., Ahn, J. Y., Stachlewska, I. S., Amiridis, V., Marinou, E., Seifert, P., Hofer, J., Skupin, A., Schneider, F., Bohlmann, S., Foth, A., Bley, S., Pfuller, A., Giannakaki, E., Lihavainen, H., Viisanen, Y., Hooda, R. K., Pereira, S. N., Bortoli, D., Wagner, F., Mattis, I., Janicka, L., Markowicz, K. M., Achtert, P., Artaxo, P., Pauliquevis, T., Souza, R. A.

F., Sharma, V. P., van Zyl, P. G., Beukes, J. P., Sun, J., Rohwer, E. G., Deng, R., Mamouri, R.-E. and Zamorano, F.: An overview of the first decade of Polly(NET): an emerging network of automated Raman-polarization lidars for continuous aerosol profiling, Atmos. Chem. Phys., 16(8), 5111–5137, doi:10.5194/acp-16-5111-2016, 2016.

Behrenfeld, M. J., O'Malley, R. T., Siegel, D. A., McClain, C. R., Sarmiento, J. L., Feldman, G. C., Milligan, A. J., Falkowski, P. G., Letelier, R. M., and Boss, E. S.: Climate-driven trends in contemporary ocean productivity, Nature, 444, 752–755, https://doi.org/10.1038/nature05317, 2006.

Ben-Ami, Y., Koren, I., Rudich, Y., Artaxo, P., Martin, S. T., and Andreae, M. O.: Transport of North African dust from the Bodélé depression to the Amazon Basin: a case study, Atmos. Chem. Phys., 10, 7533–7544, https://doi.org/10.5194/acp-10-7533-2010, 2010.

Ben-Ami, Y., Koren, I., Altaratz, O., Kostinski, A., and Lehahn, Y.: Discernible rhythm in the spatio/temporal distributions of transatlantic dust, Atmos. Chem. Phys., 12, 2253–2262, https://doi.org/10.5194/acp-12-2253-2012, 2012.

Bergas-Massó, E., Gonçalves Ageitos, M., Myriokefalitakis, S., Miller, R. L., van Noije, T., Le Sager, P., Montané Pinto, G., and Pérez García-Pando, C.: Pre-Industrial, Present and Future Atmospheric Soluble Iron Deposition and the Role of Aerosol Acidity and Oxalate Under CMIP6 Emissions, Earth's Future, 11, e2022EF003353, https://doi.org/10.1029/2022EF003353, 2023.

Berrisford P, Dee DP, Fielding K, Fuentes M, Kållberg P, Kobayashi S, Uppala SM. 2009. 'The ERA-Interim Archive'. ERA Report Series, No.1. ECMWF: Reading, UK.

Bohlmann, S., Baars, H., Radenz, M., Engelmann, R. and Macke, A.: Ship-borne aerosol profiling with lidar over the Atlantic Ocean: from pure marine conditions to complex dust-smoke mixtures, Atmos. Chem. Phys., 18(13), 9661–9679, doi:10.5194/acp-18-9661-2018, 2018.

Bohlmann, S., Shang, X., Vakkari, V., Giannakaki, E., Leskinen, A., Lehtinen, K. E. J., Pätsi, S., and Komppula, M.: Lidar depolarization ratio of atmospheric pollen at multiple wavelengths, Atmos. Chem. Phys., 21, 7083–7097, https://doi.org/10.5194/acp-21-7083-2021, 2021.

Bory, A. J.-M. and Newton, P. P.: Transport of airborne lithogenic material down through the water column in two contrasting regions of the eastern subtropical North Atlantic Ocean, Global Biogeochemical Cycles, 14, 297–315, https://doi.org/10.1029/1999GB900098, 2000.

Bory, A., Dulac, F., Moulin, C., Chiapello, I., Newton, P. P., Guelle, W., Lambert, C. E., and Bergametti, G.: Atmospheric and oceanic dust fluxes in the northeastern tropical Atlantic Ocean: how close a coupling?, Annales Geophysicae, 20, 2067–2076, https://doi.org/10.5194/angeo-20-2067-2002, 2002.

Boyd, P. W. and Ellwood, M. J.: The biogeochemical cycle of iron in the ocean, Nature Geoscience, 3, 675–682, https://doi.org/10.1038/ngeo964, 2010.

Braun, S. A.: Reevaluating the Role of the Saharan Air Layer in Atlantic Tropical Cyclogenesis and Evolution, Monthly Weather Review, 138, 2007–2037, https://doi.org/10.1175/2009MWR3135.1, 2010.

Bryant, R. G., Bigg, G. R., Mahowald, N. M., Eckardt, F. D., and Ross S. G.: Dust emission response to climate in southern Africa, J. Geophys. Res., 112, D09207, https://doi.org/10.1029/2005JD007025, 2007.

Burton, S. P., Ferrare, R. A., Vaughan, M. A., Omar, A. H., Rogers, R. R., Hostetler, C. A., and Hair, J. W.: Aerosol classification from airborne HSRL and comparisons with the CALIPSO vertical feature mask, Atmos. Meas. Tech., 6, 1397–1412, https://doi.org/10.5194/amt-6-1397-2013, 2013.

Capelle, V., Chédin, A., Siméon, M., Tsamalis, C., Pierangelo, C., Pondrom, M., Crevoisier, C., Crepeau, L., and Scott, N. A.: Evaluation of IASI-derived dust aerosol characteristics over the tropical belt, Atmospheric Chemistry and Physics, 14, 9343–9362, https://doi.org/10.5194/acp-14-9343-2014, 2014.

Carlson, T. N. and Prospero, J. M.: The Large-Scale Movement of Saharan Air Outbreaks over the Northern Equatorial Atlantic, Journal of Applied Meteorology and Climatology, 11, 283–297, https://doi.org/10.1175/1520-0450(1972)011, 1972.

Carr, M.-E., Friedrichs, M. A. M., Schmeltz, M., Noguchi Aita, M., Antoine, D., Arrigo, K. R., Asanuma, I., Aumont, O., Barber, R., Behrenfeld, M., Bidigare, R., Buitenhuis, E. T., Campbell, J., Ciotti, A., Dierssen, H., Dowell, M., Dunne, J., Esaias, W., Gentili, B., Gregg, W., Groom, S., Hoepffner, N., Ishizaka, J., Kameda, T., Le Quéré, C., Lohrenz, S., Marra, J., Mélin, F., Moore, K., Morel, A., Reddy, T. E., Ryan, J., Scardi, M., Smyth, T., Turpie, K., Tilstone, G., Waters, K., and Yamanaka, Y.: A comparison of global estimates of marine primary production from ocean color, Deep Sea Research Part II: Topical Studies in Oceanography, 53, 741–770, https://doi.org/10.1016/j.dsr2.2006.01.028, 2006.

Castellanos, P., Colarco, P., Espinosa, W. R., Guzewich, S. D., Levy, R. C., Miller, R. L., Chin, M., Kahn, R. A., Kemppinen, O., Moosmüller, H., Nowottnick, E. P., Rocha-Lima, A., Smith, M. D., Yorks, J. E., and Yu, H.: Mineral dust optical properties for remote sensing and global modeling: A review, Remote Sensing of Environment, 303, 113982, https://doi.org/10.1016/j.rse.2023.113982, 2024.

Chin, M., Ginoux, P., Kinne, S., Torres, O., Holben, B. N., Duncan, B. N., Martin, R. V., Logan, J. A., Higurashi, A., and Nakajima, T.: Tropospheric Aerosol Optical Thickness from the GOCART Model and Comparisons with Satellite and Sun Photometer Measurements, 2002.

Chin, M., Rood, R. B., Lin, S.-J., Müller, J.-F., and Thompson, A. M.: Atmospheric sulfur cycle simulated in the global model GOCART: Model description and global properties, Journal of Geophysical Research: Atmospheres, 105, 24671–24687, https://doi.org/10.1029/2000JD900384, 2000.

Chin, M., Ginoux, P., Kinne, S., Torres, O., Holben, B. N., Duncan, B. N., Martin, R. V., Logan, J. A., Higurashi, A., , and Nakajima, T.: Tropospheric Aerosol Optical Thickness from the GOCART Model and Comparisons with Satellite and Sun Photometer Measurements, J. Atmospheric Sciences, 59, 461–483, 2002.

Cuevas-Agulló, E., Barriopedro, D., García, R. D., Alonso-Pérez, S., González-Alemán, J. J., Werner, E., Suárez, D., Bustos, J. J., García-Castrillo, G., García, O., Barreto, Á., and Basart, S.: Sharp increase of Saharan dust intrusions over the Western Mediterranean and Euro-Atlantic region in winters 2020–2022 and associated atmospheric circulation, EGUsphere [preprint], https://doi.org/10.5194/egusphere-2023-1749, 2023.

Cvetkovic, B., Dagsson-Waldhauserová, P., Petkovic, S., Arnalds, Ó., Madonna, F., Proestakis, E., Gkikas, A., Vukovic Vimic, A., Pejanovic, G., Rosoldi, M., Ceburnis, D., Amiridis, V., Lisá, L., Nickovic, S., and Nikolic, J.: Fully Dynamic High–Resolution Model for Dispersion of Icelandic Airborne Mineral Dust, Atmosphere, 13, 1345, https://doi.org/10.3390/atmos13091345, 2022.

Dee, D. P., Källén, E., Simmons, A. J., and Haimberger, L.: Comments on "Reanalyses Suitable for Characterizing Long-Term Trends," https://doi.org/10.1175/2010BAMS3070.1, 2011.

Doherty, O. M., Riemer, N., and Hameed, S.: Role of the convergence zone over West Africa in controlling Saharan mineral dust load and transport in the boreal summer, Tellus B: Chemical and Physical Meteorology, 66, 23191, https://doi.org/10.3402/tellusb.v66.23191, 2014.

Döscher, R., Acosta, M., Alessandri, A., Anthoni, P., Arsouze, T., Bergman, T., Bernardello, R., Boussetta, S., Caron, L.-P., Carver, G., Castrillo, M., Catalano, F., Cvijanovic, I., Davini, P., Dekker, E., Doblas-Reyes, F. J., Docquier, D., Echevarria, P., Fladrich, U., Fuentes-Franco, R., Gröger, M., v. Hardenberg, J., Hieronymus, J., Karami, M. P., Keskinen, J.-P., Koenigk, T., Makkonen, R., Massonnet, F., Ménégoz, M., Miller, P. A., Moreno-Chamarro, E., Nieradzik, L., van Noije, T., Nolan, P., O'Donnell, D., Ollinaho, P., van den Oord, G., Ortega, P., Prims, O. T., Ramos, A., Reerink, T., Rousset, C., Ruprich-Robert, Y., Le Sager, P., Schmith, T., Schrödner, R., Serva, F., Sicardi, V., Sloth Madsen, M., Smith, B., Tian, T., Tourigny, E., Uotila, P., Vancoppenolle, M., Wang, S., Wårlind, D., Willén, U., Wyser, K., Yang, S., Yepes-Arbós, X., and Zhang, Q.: The EC-Earth3 Earth system model for the Coupled Model Intercomparison Project 6, Geosci. Model Dev., 15, 2973–3020, https://doi.org/10.5194/gmd-15-2973-2022, 2022.

Drakaki, E., Amiridis, V., Tsekeri, A., Gkikas, A., Proestakis, E., Mallios, S., Solomos, S., Spyrou, C., Marinou, E., Ryder, C. L., Bouris, D., and Katsafados, P.: Modeling coarse and giant desert dust particles, Atmos. Chem. Phys., 22, 12727–12748, https://doi.org/10.5194/acp-22-12727-2022, 2022.

Dubovik, O., Sinyuk, A., Lapyonok, T., Holben, B. N., Mishchenko, M., Yang, P., Eck, T. F., Volten, H., Munõz, O., Veihelmann, B., van der Zande, W. J., Leon, J.-F., Sorokin, M., and Slutsker, I.: Application of spheroid models to account for aerosol particle nonsphericity in remote sensing of desert dust. Journal of Geophysical Research: Atmospheres, 111(D11), 2006.

Duce, R. A., Liss, P. S., Merrill, J. T., Atlas, E. L., Buat-Menard, P., Hicks, B. B., Miller, J. M., Prospero, J. M., Arimoto, R., Church, T. M., Ellis, W., Galloway, J. N., Hansen, L., Jickells, T. D., Knap, A. H., Reinhardt, K. H., Schneider, B., Soudine, A., Tokos, J. J., Tsunogai, S., Wollast, R., and Zhou, M.: The atmospheric input of trace species to the world ocean, Global Biogeochemical Cycles, 5, 193–259, https://doi.org/10.1029/91GB01778, 1991.

Duncan Fairlie, T., Jacob, D. J., and Park, R. J.: The impact of transpacific transport of mineral dust in the United States, Atmospheric Environment, 41, 1251–1266, https://doi.org/10.1016/j.atmosenv.2006.09.048, 2007.

Dunion, J. P.: Rewriting the Climatology of the Tropical North Atlantic and Caribbean Sea Atmosphere, Journal of Climate, 24, 893–908, https://doi.org/10.1175/2010JCLI3496.1, 2011.

Eck, T. F., Holben, B. N., Reid, J. S., Dubovik, O., Smirnov, A., O'Neill, N. T., Slutsker, I., and Kinne, S.: Wavelength dependence of the optical depth of biomass burning, urban and desert dust aerosols, J. Geophys. Res., 104, 31333–31350, 1999.

Eckardt, F. D. and Kuring, N.: SeaWiFS identifies dust sources in the Namib Desert, Int. J. Remote Sens., 26, 4159–4167, 2005.

Engelstaedter, S., Tegen, I., and Washington, R.: North African dust emissions and transport, Earth-Science Reviews, 79, 73–100, https://doi.org/10.1016/j.earscirev.2006.06.004, 2006.

Escribano, J., Di Tomaso, E., Jorba, O., Klose, M., Gonçalves Ageitos, M., Macchia, F., Amiridis, V., Baars, H., Marinou, E., Proestakis, E., Urbanneck, C., Althausen, D., Bühl, J., Mamouri, R.-E., and Pérez García-Pando, C.: Assimilating spaceborne lidar dust extinction can improve dust forecasts, Atmos. Chem. Phys., 22, 535–560, https://doi.org/10.5194/acp-22-535-2022, 2022.

Escribano, J., Di Tomaso, E., Jorba, O., Gonçalves Ageitos, M., Klose, M., Basart, S., and Pérez García-Pando, C.: Constraining spatio-temporal variations in dust emission at global scale with ensemble data assimilation of satellite optical depth retrievals, EGU General Assembly 2023, Vienna, Austria, 24–28 Apr 2023, EGU23-9569, https://doi.org/10.5194/egusphere-egu23-9569, 2023.

Esselborn, M., Wirth, M., Fix, A., Weinzierl, B., Rasp, K., Tesche, M. and Petzold, A.: Spatial distribution and optical properties of Saharan dust observed by airborne high spectral resolution lidar during SAMUM 2006, Tellus Ser. B-Chem. Phys. Meteorol., 61(1), 131–143, doi:10.1111/j.1600-0889.2008.00394.x, 2009.

Falkowski, P., Scholes, R. J., Boyle, E., Canadell, J., Canfield, D., Elser, J., Gruber, N., Hibbard, K., Högberg, P., Linder, S., Mackenzie, F. T., Moore III, B., Pedersen, T., Rosenthal, Y., Seitzinger, S., Smetacek, V., and Steffen, W.: The Global Carbon Cycle: A Test of Our Knowledge of Earth as a System, Science, 290, 291–296, https://doi.org/10.1126/science.290.5490.291, 2000.

Fiedler, S., Schepanski, K., Heinold, B., Knippertz, P. and Tegen, I.: Climatology of nocturnal low-level jets over North Africa and implications for modeling mineral dust emission, J. Geophys. Res.-Atmos., 118(12), 6100–6121, doi:10.1002/jgrd.50394, 2013.

Filioglou, M., Giannakaki, E., Backman, J., Kesti, J., Hirsikko, A., Engelmann, R., O'Connor, E., Leskinen, J. T. T., Shang, X., Korhonen, H., Lihavainen, H., Romakkaniemi, S. and Komppula, M.: Optical and geometrical aerosol particle properties over the United Arab Emirates, Atmospheric Chemistry and Physics Discussions, 1–26, doi:https://doi.org/10.5194/acp-2020-133, 2020.

Fischer, G., Donner, B., Ratmeyer, V., Davenport, R., Wefer, G.,: Distinct year-to-year particle flux variations o! Cape Blanc during 1988-1991: relation to d18O-deduced sea-surface temperatures and trade winds. Journal of Marine Research 54, 73-98, doi: 10.1357/0022240963213484, 1996.

Fischer, G. and Karakaş, G.: Sinking rates and ballast composition of particles in the Atlantic Ocean: implications for the organic carbon fluxes to the deep ocean, Biogeosciences, 6, 85–102, https://doi.org/10.5194/bg-6-85-2009, 2009.

Fischer, G., Romero, O., Merkel, U., Donner, B., Iversen, M., Nowald, N., Ratmeyer, V., Ruhland, G., Klann, M., and Wefer, G.: Deep ocean mass fluxes in the coastal upwelling off Mauritania from 1988 to 2012: variability on seasonal to decadal timescales, Biogeosciences, 13, 3071–3090, https://doi.org/10.5194/bg-13-3071-2016, 2016.

Fischer, G. and Wefer, G.: Long-term observations of particle fluxes in the Eastern Atlantic: seasonality, changes of flux with depth and comparison with the sediment record, in: The South Atlantic: Present and Past Circulation, edited by: Wefer, G., Berger, W. H., Siedler, G., and Webb, D. J., Springer, Berlin, Germany, 325–344, 1996.

Floutsi, A. A., Baars, H., Engelmann, R., Althausen, D., Ansmann, A., Bohlmann, S., Heese, B., Hofer, J., Kanitz, T., Haarig, M., Ohneiser, K., Radenz, M., Seifert, P., Skupin, A., Yin, Z., Abdullaev, S. F., Komppula, M., Filioglou, M., Giannakaki, E., Stachlewska, I. S., Janicka, L., Bortoli, D., Marinou, E., Amiridis, V., Gialitaki, A., Mamouri, R.-E., Barja, B., and Wandinger, U.: DeLiAn – a growing collection of depolarization ratio, lidar ratio and Ångström exponent for different aerosol types and mixtures from ground-based lidar observations, Atmos. Meas. Tech., 16, 2353–2379, https://doi.org/10.5194/amt-16-2353-2023, 2023.

Foltz, R., G.: Satellite and in situ estimates of dust deposition in the tropical North Atlantic, Pp 156-161, Conference Proceedings, 1st International Conference on Atmospheric Dust – DUST2014, ISSN: 2283-5954, vol. 1, DOI:10.14644/dust.2014.025.

Foth, A., Kanitz, T., Engelmann, R., Baars, H., Radenz, M., Seifert, P., Barja, B., Fromm, M., Kalesse, H., and Ansmann, A.: Vertical aerosol distribution in the southern hemispheric midlatitudes as observed with lidar in Punta Arenas, Chile (53.2∘ S and 70.9∘ W), during ALPACA, Atmos. Chem. Phys., 19, 6217–6233, https://doi.org/10.5194/acp-19-6217-2019, 2019.

Freudenthaler, V., Esselborn, M., Wiegner, M., Heese, B., Tesche, M., Ansmann, A., Mueller, D., Althausen, D., Wirth, M., Fix, A., Ehret, G., Knippertz, P., Toledano, C., Gasteiger, J., Garhammer, M. and Seefeldner, A.: Depolarization ratio profiling at several wavelengths in pure Saharan dust during SAMUM 2006, Tellus Ser. B-Chem. Phys. Meteorol., 61(1), 165–179, doi:10.1111/j.1600-0889.2008.00396.x, 2009.

Friese, C. A., van Hateren, J. A., Vogt, C., Fischer, G., and Stuut, J.-B. W.: Seasonal provenance changes in present-day Saharan dust collected in and off Mauritania, Atmospheric Chemistry and Physics, 17, 10163–10193, https://doi.org/10.5194/acp-17-10163-2017, 2017.

Gaiero, D. M., Probst, J.-L., Depetris, P. J., Bidart, S. M., and Leleyter, L.: Iron and other transition metals in Patagonian riverborne and windborne materials: geochemical control and transport to the southern South Atlantic Ocean, Geochimica et Cosmochimica Acta, 67, 3603–3623, https://doi.org/10.1016/S0016-7037(03)00211-4, 2003.

Gao, Y., Fan, S.-M., and Sarmiento, J. L.: Aeolian iron input to the ocean through precipitation scavenging: A modeling perspective and its implication for natural iron fertilization in the ocean, Journal of Geophysical Research: Atmospheres, 108, https://doi.org/10.1029/2002JD002420, 2003.

Garay, M. J., Witek, M. L., Kahn, R. A., Seidel, F. C., Limbacher, J. A., Bull, M. A., Diner, D. J., Hansen, E. G., Kalashnikova, O. V., Lee, H., Nastan, A. M., and Yu, Y.: Introducing the 4.4 km spatial resolution Multi-Angle Imaging

SpectroRadiometer (MISR) aerosol product, Atmospheric Measurement Techniques, 13, 593–628, https://doi.org/10.5194/amt-13-593-2020, 2020.

Garnier, A., Scott, N. A., Pelon, J., Armante, R., Crépeau, L., Six, B. and Pascal, N.: Long-term assessment of the CALIPSO Imaging Infrared Radiometer (IIR) calibration and stability through simulated and observed comparisons with MODIS/Aqua and SEVIRI/Meteosat, Atmospheric Measurement Techniques, 10(4), 1403–1424, doi:https://doi.org/10.5194/amt-10-1403-2017, 2017.

~~Gassó, S. and Stein, A. F.: Does dust from Patagonia reach the sub-Antarctic Atlantic Ocean?, Geophys. Res. Lett., 34, L01801, https://doi.org/10.1029/2006GL027693, 2007.~~

Gassó, S., Stein, A., Marino, F., Castellano, E., Udisti, R., and Ceratto, J.: A combined observational and modeling approach to study modern dust transport from the Patagonia desert to East Antarctica, Atmos. Chem. Phys., 10, 8287–8303, https://doi.org/10.5194/acp-10-8287-2010, 2010.

Gassó, S. and Torres, O.: Temporal characterization of dust activity in the Central Patagonia desert (years 1964–2017), J. Geophys. Res.-Atmos., 124, 3417–3434, https://doi.org/10.1029/2018JD030209, 2019.

~~Garnier, A., Scott, N. A., Pelon, J., Armante, R., Crépeau, L., Six, B. and Pascal, N.: Long-term assessment of the CALIPSO Imaging Infrared Radiometer (IIR) calibration and stability through simulated and observed comparisons with MODIS/Aqua and SEVIRI/Meteosat, Atmospheric Measurement Techniques, 10(4), 1403–1424, doi:https://doi.org/10.5194/amt-10-1403-2017, 2017.~~

~~Gassó, S. and Torres, O.: Temporal characterization of dust activity in the Central Patagonia desert (years 1964–2017), J. Geophys. Res.-Atmos., 124, 3417–3434, https://doi.org/10.1029/2018JD030209, 2019.~~

Gates, W. L., Boyle, J. S., Covey, C., Dease, C. G., Doutriaux, C. M., Drach, R. S., Fiorino, M., Gleckler, P. J., Hnilo, J. J., Marlais, S. M., Phillips, T. J., Potter, G. L., Santer, B. D., Sperber, K. R., Taylor, K. E., and Williams, D. N.: An Overview of the Results of the Atmospheric Model Intercomparison Project (AMIP I), 1999.

Getzewich, B. J., Vaughan, M. A., Hunt, W. H., Avery, M. A., Powell, K. A., Tackett, J. L., Winker, D. M., Kar, J., Lee, K.-P. and Toth, T. D.: CALIPSO lidar calibration at 532nm: version 4 daytime algorithm, Atmospheric Measurement Techniques, 11(11), 6309–6326, doi:https://doi.org/10.5194/amt-11-6309-2018, 2018.

Gidden, M. J., Riahi, K., Smith, S. J., Fujimori, S., Luderer, G., Kriegler, E., van Vuuren, D. P., van den Berg, M., Feng, L., Klein, D., Calvin, K., Doelman, J. C., Frank, S., Fricko, O., Harmsen, M., Hasegawa, T., Havlik, P., Hilaire, J., Hoesly, R., Horing, J., Popp, A., Stehfest, E., and Takahashi, K.: Global emissions pathways under different socioeconomic scenarios for use in CMIP6: a dataset of harmonized emissions trajectories through the end of the century, Geoscientific Model Development, 12, 1443–1475, https://doi.org/10.5194/gmd-12-1443-2019, 2019.

Ginoux, P., Chin, M., Tegen, I., Prospero, J. M., Holben, B., Dubovik, O., and Lin, S.-J.: Sources and distributions of dust aerosols simulated with the GOCART model, Journal of Geophysical Research: Atmospheres, 106, 20255–20273, https://doi.org/10.1029/2000JD000053, 2001.

Ginoux, P., Prospero, J. M., Torres, O., and Chin, M.: Long-term simulation of global dust distribution with the GOCART model: correlation with North Atlantic Oscillation, Environmental Modelling & Software, 19, 113–128, https://doi.org/10.1016/S1364-8152(03)00114-2, 2004.

Ginoux, P., Prospero, J. M., Gill, T. E., Hsu, N. C., and Zhao, M.: Global-scale attribution of anthropogenic and natural dust sources and their emission rates based on MODIS Deep Blue aerosol products, Rev. Geophys., 50, RG3005, https://doi.org/10.1029/2012RG000388, 2012.

Gittings, J. A., Dall'Olmo, G., Tang, W., Llort, J., Jebri, F., Livanou, E., Nencioli, F., Darmaraki, S., Theodorou, I., Brewin, R. J. W., Srokosz, M., Cassar, N., and Raitsos, D. E.: An exceptional phytoplankton bloom in the southeast Madagascar Sea driven by African dust deposition, PNAS Nexus, 3, pgae386, https://doi.org/10.1093/pnasnexus/pgae386, 2024.

Gkikas, A., Proestakis, E., Amiridis, V., Kazadzis, S., Di Tomaso, E., Marinou, E., Hatzianastassiou, N., Kok, J. F., and García-Pando, C. P.: Quantification of the dust optical depth across spatiotemporal scales with the MIDAS global dataset (2003–2017), Atmos. Chem. Phys., 22, 3553–3578, https://doi.org/10.5194/acp-22-3553-2022, 2022.

Gkikas, A., Houssos, E. E., Lolis, C. J., Bartzokas, A., Mihalopoulos, N., and Hatzianastassiou, N.: Atmospheric circulation evolution related to desert-dust episodes over the Mediterranean, Q. J. Roy. Meteor. Soc., 141, 1634–1645, https://doi.org/10.1002/qj.2466, 2015.

Gkikas, A., Proestakis, E., Amiridis, V., Kazadzis, S., Di Tomaso, E., Marinou, E., Hatzianastassiou, N., Kok, J. F., and García-Pando, C. P.: Quantification of the dust optical depth across spatiotemporal scales with the MIDAS global dataset (2003–2017), Atmos. Chem. Phys., 22, 3553–3578, https://doi.org/10.5194/acp-22-3553-2022, 2022.

Gläser, G., Wernli, H., Kerkweg, A., and Teubler, F.: The transatlantic dust transport from North Africa to the Americas—Its characteristics and source regions, Journal of Geophysical Research: Atmospheres, 120, 11,231-11,252, https://doi.org/10.1002/2015JD023792, 2015.

Gliß, J., Mortier, A., Schulz, M., Andrews, E., Balkanski, Y., Bauer, S. E., Benedictow, A. M. K., Bian, H., Checa-Garcia, R., Chin, M., Ginoux, P., Griesfeller, J. J., Heckel, A., Kipling, Z., Kirkevåg, A., Kokkola, H., Laj, P., Le Sager, P., Lund, M. T., Lund Myhre, C., Matsui, H., Myhre, G., Neubauer, D., van Noije, T., North, P., Olivié, D. J. L., Rémy, S., Sogacheva, L., Takemura, T., Tsigaridis, K., and Tsyro, S. G.: AeroCom phase III multi-model evaluation of the aerosol life cycle and optical properties using ground- and space-based remote sensing as well as surface in situ observations, Atmos. Chem. Phys., 21, 87–128, https://doi.org/10.5194/acp-21-87-2021, 2021.

Gnanadesikan, A., Emanuel, K., Vecchi, G. A., Anderson, W. G., and Hallberg, R.: How ocean color can steer Pacific tropical cyclones, Geophysical Research Letters, 37, https://doi.org/10.1029/2010GL044514, 2010.

Gomes, L., Rajot, J. L., Alfaro, S. C., and Gaudichet, A.: Validation of a dust production model from measurements performed in semi-arid agricultural areas of Spain and Niger, Catena, 52, 257–271, 2003.

~~Groß~~Gross, S., Tesche, M., Freudenthaler, V., Toledano, C., Wiegner, M., Ansmann, A., Althausen, D., and Seefeldner, M.: Characterization of Saharan dust, marine aerosols and mixtures of biomass-burning aerosols and dust by means of multi-

wavelength depolarization and Raman lidar measurements during SAMUM 2, Tellus B, 63, 706–724, https://doi.org/10.1111/j.1600-0889.2011.00556.x, 2011a.

~~Groß~~Gross, S., Wiegner, M., Freudenthaler, V., and Toledano, C.: Lidar ratio of Saharan dust over ~~Cape Verde~~Cabo Verde Islands: Assessment and error calculation, J. Geophys. Res.-Atmos., 116, D15203, https://doi.org/10.1029/2010JD015435, 2011b.

Groß, S., Freudenthaler, V., Wiegner, M., Gasteiger, J., Geiss, A., and Schnell, F.: Dual-wavelength linear depolarization ratio of volcanic aerosols: Lidar measurements of the Eyjafjallajokull plume over Maisach, Germany, Atmos. Environ., 48, 85–96, https://doi.org/10.1016/j.atmosenv.2011.06.017, 2012.

~~Gross, S., Wiegner, M., Freudenthaler, V. and Toledano, C.: Lidar ratio of Saharan dust over Cape Verde Islands: Assessment and error calculation, J. Geophys. Res. Atmos., 116, D15203, doi:10.1029/2010JD015435, 2011.Gross, S., Freudenthaler, V., Wiegner, M., Gasteiger, J., Geiss, A. and Schnell, F.: Dual-wavelength linear depolarization ratio of volcanic aerosols: Lidar measurements of the Eyjafjallajokull plume over Maisach, Germany, Atmos. Environ., 48, 85–96, doi:10.1016/j.atmosenv.2011.06.017, 2012.~~

Gross, S., Freudenthaler, V., Schepanski, K., Toledano, C., Schaefler, A., Ansmann, A. and Weinzierl, B.: Optical properties of long-range transported Saharan dust over Barbados as measured by dual-wavelength depolarization Raman lidar measurements, Atmos. Chem. Phys., 15(19), 11067–11080, doi:10.5194/acp-15-11067-2015, 2015.

Guerreiro, C. V., Baumann, K.-H., Brummer, G.-J. A., Korte, L. F., Sá, C., and Stuut, J.-B. W.: Transatlantic gradients in calcifying phytoplankton (coccolithophore) fluxes, Progress in Oceanography, 176, 102140, https://doi.org/10.1016/j.pocean.2019.102140, 2019.

Guerreiro, C. V., Baumann, K.-H., Brummer, G.-J. A., Valente, A., Fischer, G., Ziveri, P., Brotas, V., and Stuut, J.-B. W.: Carbonate fluxes by coccolithophore species between NW Africa and the Caribbean: Implications for the biological carbon pump, Limnology and Oceanography, 66, 3190–3208, https://doi.org/10.1002/lno.11872, 2021.

Guerreiro, C. V., Ferreira, A., Cros, L., Stuut, J.-B., Baker, A., Tracana, A., Pinto, C., Veloso, V., Rees, A. P., Cachão, M. A. P., Nunes, T., and Brotas, V.: Response of coccolithophore communities to oceanographic and atmospheric processes across the North- and Equatorial Atlantic, Front. Mar. Sci., 10, https://doi.org/10.3389/fmars.2023.1119488, 2023.

Guieu, C., Dulac, F., Ridame, C., and Pondaven, P.: Introduction to project DUNE, a DUst experiment in a low Nutrient, low chlorophyll Ecosystem, Biogeosciences, 11, 425–442, https://doi.org/10.5194/bg-11-425-2014, 2014.

Haarig, M., Ansmann, A., Gasteiger, J., Kandler, K., Althausen, D., Baars, H., Radenz, M. and Farrell, D. A.: Dry versus wet marine particle optical properties: RH dependence of depolarization ratio, backscatter, and extinction from multiwavelength lidar measurements during SALTRACE, Atmos. Chem. Phys., 17(23), 14199–14217, doi:10.5194/acp-17-14199-2017, 2017a.

Haarig, M., Ansmann, A., Althausen, D., Klepel, A., Gross, S., Freudenthaler, V., Toledano, C., Mamouri, R.-E., Farrell, D. A., Prescod, D. A., Marinou, E., Burton, S. P., Gasteiger, J., Engelmann, R. and Baars, H.: Triple-wavelength depolarization-ratio profiling of Saharan dust over Barbados during SALTRACE in 2013 and 2014, Atmos. Chem. Phys., 17(17), 10767–10794, doi:10.5194/acp-17-10767-2017, 2017b.

Hand, J. L., Mahowald, N. M., Chen, Y., Siefert, R. L., Luo, C., Subramaniam, A., and Fung, I.: Estimates of atmospheric-processed soluble iron from observations and a global mineral aerosol model: Biogeochemical implications, Journal of Geophysical Research: Atmospheres, 109, https://doi.org/10.1029/2004JD004574, 2004.

Haustein, K., Pérez, C., Baldasano, J. M., Jorba, O., Basart, S., Miller, R. L., Janjic, Z., Black, T., Nickovic, S., Todd, M. C., Washington, R., Müller, D., Tesche, M., Weinzierl, B., Esselborn, M., and Schladitz, A.: Atmospheric dust modeling from meso to global scales with the online NMMB/BSC-Dust model – Part 2: Experimental campaigns in Northern Africa, Atmospheric Chemistry and Physics, 12, 2933–2958, https://doi.org/10.5194/acp-12-2933-2012, 2012.

Hersbach, H., Bell, B., Berrisford, P., Hirahara, S., Horányi, A., Muñoz-Sabater, J., Nicolas, J., Peubey, C., Radu, R., Schepers, D., Simmons, A., Soci, C., Abdalla, S., Abellan, X., Balsamo, G., Bechtold, P., Biavati, G., Bidlot, J., Bonavita, M., De Chiara, G., Dahlgren, P., Dee, D., Diamantakis, M., Dragani, R., Flemming, J., Forbes, R., Fuentes, M., Geer, A., Haimberger, L., Healy, S., Hogan, R. J., Hólm, E., Janisková, M., Keeley, S., Laloyaux, P., Lopez, P., Lupu, C., Radnoti, G., de Rosnay, P., Rozum, I., Vamborg, F., Villaume, S., and Thépaut, J.-N.: The ERA5 global reanalysis, Quarterly Journal of the Royal Meteorological Society, 146, 1999–2049, https://doi.org/10.1002/qj.3803, 2020.

Hess, M., Koepke, P., and Schult, I.: Optical Properties of Aerosols and Clouds: The Software Package OPAC. Bulletin American Meteorological Society, 79, 831–844, 1998.

Hoesly, R. M., Smith, S. J., Feng, L., Klimont, Z., Janssens-Maenhout, G., Pitkanen, T., Seibert, J. J., Vu, L., Andres, R. J., Bolt, R. M., Bond, T. C., Dawidowski, L., Kholod, N., Kurokawa, J.-I., Li, M., Liu, L., Lu, Z., Moura, M. C. P., O'Rourke, P. R., and Zhang, Q.: Historical (1750–2014) anthropogenic emissions of reactive gases and aerosols from the Community Emissions Data System (CEDS), Geosci. Model Dev., 11, 369–408, https://doi.org/10.5194/gmd-11-369-2018, 2018.

Hofer, J., Althausen, D., Abdullaev, S. F., Makhmudov, A. N., Nazarov, B. I., Schettler, G., Engelmann, R., Baars, H., Fomba, K. W., Mueller, K., Heinold, B., Kandler, K. and Ansmann, A.: Long-term profiling of mineral dust and pollution aerosol with multiwavelength polarization Raman lidar at the Central Asian site of Dushanbe, Tajikistan: case studies, Atmos. Chem. Phys., 17(23), 14559–14577, doi:10.5194/acp-17-14559-2017, 2017.

Honjo, S. and Manganini, S. J.: Annual biogenic particle fluxes to the interior of the North Atlantic Ocean; studied at 34°N 21°W and 48°N 21°W, Deep Sea Research Part II: Topical Studies in Oceanography, 40, 587–607, https://doi.org/10.1016/0967-0645(93)90034-K, 1993.

Hostetler, C. A., Behrenfeld, M. J., Hu, Y., Hair, J. W., and Schulien, J. A.: Spaceborne Lidar in the Study of Marine Systems, Annual Review of Marine Science, 10, 121–147, https://doi.org/10.1146/annurev-marine-121916-063335, 2018.

Huang, J., Zhang, C., and Prospero, J. M.: African dust outbreaks: A satellite perspective of temporal and spatial variability over the tropical Atlantic Ocean, Journal of Geophysical Research: Atmospheres, 115, https://doi.org/10.1029/2009JD012516, 2010.

Huneeus, N., Schulz, M., Balkanski, Y., Griesfeller, J., Prospero, J., Kinne, S., Bauer, S., Boucher, O., Chin, M., Dentener, F., Diehl, T., Easter, R., Fillmore, D., Ghan, S., Ginoux, P., Grini, A., Horowitz, L., Koch, D., Krol, M. C., Landing, W., Liu, X., Mahowald, N., Miller, R., Morcrette, J.-J., Myhre, G., Penner, J., Perlwitz, J., Stier, P., Takemura, T., and Zender, C. S.: Global

dust model intercomparison in AeroCom phase I, Atmospheric Chemistry and Physics, 11, 7781–7816, https://doi.org/10.5194/acp-11-7781-2011, 2011.

Hunt, W. H., Winker, D. M., Vaughan, M. A., Powell, K. A., Lucker, P. L. and Weimer, C.: CALIPSO Lidar Description and Performance Assessment, J. Atmos. Oceanic Technol., 26(7), 1214–1228, doi:10.1175/2009JTECHA1223.1, 2009.

Inness, A., Ades, M., Agustí-Panareda, A., Barré, J., Benedictow, A., Blechschmidt, A.-M., Dominguez, J. J., Engelen, R., Eskes, H., Flemming, J., Huijnen, V., Jones, L., Kipling, Z., Massart, S., Parrington, M., Peuch, V.-H., Razinger, M., Remy, S., Schulz, M., and Suttie, M.: The CAMS reanalysis of atmospheric composition, Atmospheric Chemistry and Physics, 19, 3515–3556, https://doi.org/10.5194/acp-19-3515-2019, 2019.

Iacono, M. J., Mlawer, E. J., Clough, S. A., and Morcrette, J. J.: Impact of an improved longwave radiation model, RRTM, on the energy budget and thermodynamic properties of the NCAR community climate model, CCM3, J. Geophys. Res., 105, 14873–14890, 2000.

Iacono, M. J., Delamere, J. S., Mlawer, E. J., Shephard, M. W., Clough, S. A., and Collins, W. D.: Radiative forcing by long-lived greenhouse gases: Calculations with the AER radiative transfer models, Journal of Geophysical Research: Atmospheres, 113, https://doi.org/10.1029/2008JD009944, 2008.

Illingworth, A. J., Barker, H. W., Beljaars, A., Ceccaldi, M., Chepfer, H., Clerbaux, N., Cole, J., Delanoe, J., Domenech, C., Donovan, D. P., Fukuda, S., Hirakata, M., Hogan, R. J., Huenerbein, A., Kollias, P., Kubota, T., Nakajima, T., Nakajima, T. Y., Nishizawa, T., Ohno, Y., Okamoto, H., Oki, R., Sato, K., Satoh, M., Shephard, M. W., Velazquez-Blazquez, A., Wandinger, U., Wehr, T., and van Zadelhoff, G.-J.: THE EARTHCARE SATELLITE The Next Step Forward in Global Measurements of Clouds, Aerosols, Precipitation, and Radiation, B. Am. Meteorol. Soc., 96, 1311–1332, https://doi.org/10.1175/BAMS-D-12-00227.1, 2015.

IPCC, 2014: Climate Change 2014: Synthesis Report. Contribution of Working Groups I, II and III to the Fifth Assessment Report of the Intergovernmental Panel on Climate Change [Core Writing Team, R.K. Pachauri and L.A. Meyer (eds.)]. IPCC, Geneva, Switzerland, 151 pp.

Ito, T. and Follows, M.: Upper ocean control on the solubility pump of CO2. Journal of Marine Research, 61 (4), 465-489, 2003. https://doi.org/10.1357/002224003322384898.

Ito, A. and Shi, Z.: Delivery of anthropogenic bioavailable iron from mineral dust and combustion aerosols to the ocean, Atmospheric Chemistry and Physics, 16, 85–99, https://doi.org/10.5194/acp-16-85-2016, 2016.

Ito, A., Myriokefalitakis, S., Kanakidou, M., Mahowald, N. M., Scanza, R. A., Hamilton, D. S., Baker, A. R., Jickells, T., Sarin, M., Bikkina, S., Gao, Y., Shelley, R. U., Buck, C. S., Landing, W. M., Bowie, A. R., Perron, M. M. G., Guieu, C., Meskhidze, N., Johnson, M. S., Feng, Y., Kok, J. F., Nenes, A., and Duce, R. A.: Pyrogenic iron: The missing link to high iron solubility in aerosols, Sci. Adv., 5, eaau7671, https://doi.org/10.1126/sciadv.aau7671, 2019.

Ito, A., Ye, Y., Baldo, C., and Shi, Z.: Ocean fertilization by pyrogenic aerosol iron, npj Clim Atmos Sci, 4, 1–20, https://doi.org/10.1038/s41612-021-00185-8, 2021.

Janjic, Z. I.: A nonhydrostatic model based on a new approach, Meteorol Atmos Phys, 82, 271–285, https://doi.org/10.1007/s00703-001-0587-6, 2003.

Janjic, A. Z. and Gall, A. R. L.: Scientific documentation of the NCEP nonhydrostatic multiscale model on the B grid (NMMB). Part 1 Dynamics, n.d.

Jickells, T. D., Newton, P. P., King, P., Lampitt, R. S., and Boutle, C.: A comparison of sediment trap records of particle fluxes from 19 to 48°N in the northeast Atlantic and their relation to surface water productivity, Deep Sea Research Part I: Oceanographic Research Papers, 43, 971–986, https://doi.org/10.1016/0967-0637(96)00063-5, 1996.

Jickells, T. D., Dorling, S., Deuser, W. G., Church, T. M., Arimoto, R., and Prospero, J. M.: Air-borne dust fluxes to a deep water sediment trap in the Sargasso Sea, Global Biogeochemical Cycles, 12, 311–320, https://doi.org/10.1029/97GB03368, 1998.

Jickells, T. D., An, Z. S., Andersen, K. K., Baker, A. R., Bergametti, G., Brooks, N., Cao, J. J., Boyd, P. W., Duce, R. A., Hunter, K. A., Kawahata, H., Kubilay, N., laRoche, J., Liss, P. S., Mahowald, N., Prospero, J. M., Ridgwell, A. J., Tegen, I., and Torres, R.: Global Iron Connections Between Desert Dust, Ocean Biogeochemistry, and Climate, Science, 308, 67–71, https://doi.org/10.1126/science.1105959, 2005.

Jickells, T. and Moore, C. M.: The Importance of Atmospheric Deposition for Ocean Productivity, Annual Review of Ecology, Evolution, and Systematics, 46, https://doi.org/10.1146/annurev-ecolsys-112414-054118, 2015.

Johnson, M. S., Meskhidze, N., Solmon, F., Gassó, S., Chuang, P. Y., Gaiero, D. M., Yantosca, R. M., Wu, S., Wang, Y., and Carouge, C.: Modeling dust and soluble iron deposition to the South Atlantic Ocean, Journal of Geophysical Research: Atmospheres, 115, https://doi.org/10.1029/2009JD013311, 2010.

Jones, C., Mahowald, N., and Luo, C.: The Role of Easterly Waves on African Desert Dust Transport, Journal of Climate, 16, 3617–3628, https://doi.org/10.1175/1520-0442(2003)016, 2003.

Kacenelenbogen, M., Vaughan, M. A., Redemann, J., Hoff, R. M., Rogers, R. R., Ferrare, R. A., Russell, P. B., Hostetler, C. A., Hair, J. W., and Holben, B. N.: An accuracy assessment of the CALIOP/CALIPSO version 2/version 3 daytime aerosol extinction product based on a detailed multi-sensor, multi-platform case study, Atmos. Chem. Phys., 11, 3981–4000, https://doi.org/10.5194/acp-11-3981-2011, 2011.

Kalnay, E., Kanamitsu, M., Kistler, R., Collins, W., Deaven, D., Gandin, L., Iredell, M., Saha, S., White, G., Woollen, J., Zhu, Y., Chelliah, M., Ebisuzaki, W., Higgins, W., Janowiak, J., Mo, K. C., Ropelewski, C., Wang, J., Leetmaa, A., Reynolds, R., Jenne, R., and Joseph, D.: The NCEP/NCAR 40-Year Reanalysis Project, 1996.

Kanitz, T., Ansmann, A., Engelmann, R. and Althausen, D.: North-south cross sections of the vertical aerosol distribution over the Atlantic Ocean from multiwavelength Raman/polarization lidar during Polarstern cruises, Journal of Geophysical Research: Atmospheres, 118(6), 2643–2655, doi:10.1002/jgrd.50273, 2013.

Kanitz, T., Engelmann, R., Heinold, B., Baars, H., Skupin, A. and Ansmann, A.: Tracking the Saharan Air Layer with shipborne lidar across the tropical Atlantic, Geophysical Research Letters, 41(3), 1044–1050, doi:10.1002/2013GL058780, 2014.

Kar, J., Vaughan, M. A., Lee, K.-P., Tackett, J. L., Avery, M. A., Garnier, A., Getzewich, B. J., Hunt, W. H., Josset, D., Liu, Z., Lucker, P. L., Magill, B., Omar, A. H., Pelon, J., Rogers, R. R., Toth, T. D., Trepte, C. R., Vernier, J.-P., Winker, D. M. and Young, S. A.: CALIPSO lidar calibration at 532 nm: version 4 nighttime algorithm, Atmospheric Measurement Techniques, 11(3), 1459–1479, doi:https://doi.org/10.5194/amt-11-1459-2018, 2018.

Kar, J., Lee, K.-P., Vaughan, M. A., Tackett, J. L., Trepte, C. R., Winker, D. M., Lucker, P. L. and Getzewich, B. J.: CALIPSO level 3 stratospheric aerosol profile product: version 1.00 algorithm description and initial assessment, Atmospheric Measurement Techniques, 12(11), 6173–6191, doi:https://doi.org/10.5194/amt-12-6173-2019, 2019.

Kaufman, Y. J., Koren, I., Remer, L. A., Tanré, D., Ginoux, P., and Fan, S.: Dust transport and deposition observed from the Terra-Moderate Resolution Imaging Spectroradiometer (MODIS) spacecraft over the Atlantic Ocean, Journal of Geophysical Research: Atmospheres, 110, https://doi.org/10.1029/2003JD004436, 2005.

Kim, D., Chin, M., Yu, H., Diehl, T., Tan, Q., Kahn, R. A., Tsigaridis, K., Bauer, S. E., Takemura, T., Pozzoli, L., Bellouin, N., Schulz, M., Peyridieu, S., Chédin, A., and Koffi, B.: Sources, sinks, and transatlantic transport of North African dust aerosol: A multimodel analysis and comparison with remote sensing data, Journal of Geophysical Research: Atmospheres, 119, 6259–6277, https://doi.org/10.1002/2013JD021099, 2014.

Kim, M.-H., Omar, A. H., Tackett, J. L., Vaughan, M. A., Winker, D. M., Trepte, C. R., Hu, Y., Liu, Z., Poole, L. R., Pitts, M. C., Kar, J. and Magill, B. E.: The CALIPSO version 4 automated aerosol classification and lidar ratio selection algorithm, Atmospheric Measurement Techniques, 11(11), 6107–6135, doi:https://doi.org/10.5194/amt-11-6107-2018, 2018.

Klose, M., Shao, Y., Karremann, M. K., and Fink, A.: Sahel dust zone and synoptic background, Geophys. Res. Lett., 37, L09802, https://doi.org/10.1029/2010GL042816, 2010.

Klose, M., Jorba, O., Gonçalves Ageitos, M., Escribano, J., Dawson, M. L., Obiso, V., Di Tomaso, E., Basart, S., Montané Pinto, G., Macchia, F., Ginoux, P., Guerschman, J., Prigent, C., Huang, Y., Kok, J. F., Miller, R. L., and Pérez García-Pando, C.: Mineral dust cycle in the Multiscale Online Nonhydrostatic AtmospheRe CHemistry model (MONARCH) Version 2.0, Geoscientific Model Development, 14, 6403–6444, https://doi.org/10.5194/gmd-14-6403-2021, 2021.

Knauer, G. and Asper, V.: Sediment Trap Technology and Sampling, U.S. Global Ocean Flux Study, WHOI, US GOFS Planning Report, 1989.

Knippertz, P., Deutscher, C., Kandler, K., Mueller, T., Schulz, O. and Schuetz, L.: Dust mobilization due to density currents in the Atlas region: Observations from the Saharan Mineral Dust Experiment 2006 field campaign, J. Geophys. Res.-Atmos., 112(D21), D21109, doi:10.1029/2007JD008774, 2007.

Knippertz, P., Ansmann, A., Althausen, D., Mueller, D., Tesche, M., Bierwirth, E., Dinter, T., Mueller, T., Von Hoyningen-Huene, W., Schepanski, K., Wendisch, M., Heinold, B., Kandler, K., Petzold, A., Schuetz, L. and Tegen, I.: Dust mobilization and transport in the northern Sahara during SAMUM 2006 - a meteorological overview, Tellus Ser. B-Chem. Phys. Meteorol., 61(1), 12–31, doi:10.1111/j.1600-0889.2008.00380.x, 2009.

Knippertz, P., Tesche, M., Heinold, B., Kandler, K., Toledano, C. and Esselborn, M.: Dust mobilization and aerosol transport from West Africa to ~~Cape Verde~~Cabo Verde-a meteorological overview of SAMUM-2, Tellus Ser. B-Chem. Phys. Meteorol., 63(4), 430–447, doi:10.1111/j.1600-0889.2011.00544.x, 2011.

Knippertz, P. and Todd, M. C.: Mineral dust aerosols over the Sahara: Meteorological controls on emission and transport and implications for modeling, Reviews of Geophysics, 50, 2012.

Koch, J. and Renno, N. O.: The role of convective plumes and vortices on the global aerosol budget, Geophys. Res. Lett., 32(18), L18806, doi:10.1029/2005GL023420, 2005.

Kohfeld, K. E. and Harrison, S. P.: DIRTMAP: the geological record of dust, Earth-Science Reviews, 54, 81–114, https://doi.org/10.1016/S0012-8252(01)00042-3, 2001.

Kok, J. F.: A scaling theory for the size distribution of emitted dust aerosols suggests climate models underestimate the size of the global dust cycle, PNAS, 108, 1016–1021, https://doi.org/10.1073/pnas.1014798108, 2011.

Kok, J. F., Adebiyi, A. A., Albani, S., Balkanski, Y., Checa-Garcia, R., Chin, M., Colarco, P. R., Hamilton, D. S., Huang, Y., Ito, A., Klose, M., Li, L., Mahowald, N. M., Miller, R. L., Obiso, V., Pérez García-Pando, C., Rocha-Lima, A., and Wan, J. S.: Contribution of the world's main dust source regions to the global cycle of desert dust, Atmospheric Chemistry and Physics, 21, 8169–8193, https://doi.org/10.5194/acp-21-8169-2021, 2021.

Kok, J. F., Storelvmo, T., Karydis, V. A., Adebiyi, A. A., Mahowald, N. M., Evan, A. T., He, C., and Leung, D. M.: Mineral dust aerosol impacts on global climate and climate change, Nat Rev Earth Environ, 1–16, https://doi.org/10.1038/s43017-022-00379-5, 2023.

Koopmann, B. (1981): Sedimentation von Saharastaub im subtropischen Nordatlantik während der letzten 25.000 Jahre , "Meteor" Forschungs-Ergebnisse, C, Bremerhaven, PANGAEA, 35 , pp. 23-59 .

Koren, I., Kaufman, Y. J., Washington, R., Todd, M. C., Rudich, Y., Martins, J. V., and Rosenfeld, D.: The Bodélé depression: a single spot in the Sahara that provides most of the mineral dust to the Amazon forest, Environ. Res. Lett., 1, 014005, https://doi.org/10.1088/1748-9326/1/1/014005, 2006.

Korte, L. F., Brummer, G.-J. A., van der Does, M., Guerreiro, C. V., Hennekam, R., van Hateren, J. A., Jong, D., Munday, C. I., Schouten, S., and Stuut, J.-B. W.: Downward particle fluxes of biogenic matter and Saharan dust across the equatorial North Atlantic, Atmospheric Chemistry and Physics, 17, 6023–6040, https://doi.org/10.5194/acp-17-6023-2017, 2017.

Kremling, K. and Streu, P.: Saharan dust influenced trace element fluxes in deep North Atlantic subtropical waters, Deep Sea Research Part I: Oceanographic Research Papers, 40, 1155–1168, https://doi.org/10.1016/0967-0637(93)90131-L, 1993.

Krishnamurthy, A., Moore, J. K., Zender, C. S., and Luo, C.: Effects of atmospheric inorganic nitrogen deposition on ocean biogeochemistry, Journal of Geophysical Research: Biogeosciences, 112, https://doi.org/10.1029/2006JG000334, 2007.

Krishnamurthy, A., Moore, J. K., Mahowald, N., Luo, C., and Zender, C. S.: Impacts of atmospheric nutrient inputs on marine biogeochemistry, J. Geophys. Res., 115, G01006, https://doi.org/10.1029/2009JG001115, 2010.

Kuss, J. and Kremling, K.: Particulate trace element fluxes in the deep northeast Atlantic Ocean, Deep Sea Research Part I: Oceanographic Research Papers, 46, 149–169, https://doi.org/10.1016/S0967-0637(98)00059-4, 1999.

Lavaysse, C., Flamant, C., Janicot, S., Parker, D. J., Lafore, J.-P., Sultan, B., and Pelon, J.: Seasonal evolution of the West African heat low: a climatological perspective, Clim Dyn, 33, 313–330, https://doi.org/10.1007/s00382-009-0553-4, 2009.

Lawrence, C. R. and Neff, J. C.: The contemporary physical and chemical flux of aeolian dust: A synthesis of direct measurements of dust deposition, Chemical Geology, 267, 46–63, https://doi.org/10.1016/j.chemgeo.2009.02.005, 2009.

~~Liu, Z., Vaughan, M., Winker, D., Kittaka, C., Getzewich, B., Kuehn, R., Omar, A., Powell, K., Trepte, C. and Hostetler, C.: The CALIPSO Lidar Cloud and Aerosol Discrimination: Version 2 Algorithm and Initial Assessment of Performance, J. Atmos. Ocean. Technol., 26(7), 1198–1213, doi:10.1175/2009JTECHA1229.1, 2009.~~

Liu, Z., Vaughan, M., Winker, D., Kittaka, C., Getzewich, B., Kuehn, R., Omar, A., Powell, K., Trepte, C., and Hostetler, C.: The CALIPSO Lidar Cloud and Aerosol Discrimination: Version 2 Algorithm and Initial Assessment of Performance, J. Atmos. Ocean. Technol., 26, 1198–1213, https://doi.org/10.1175/2009JTECHA1229.1, 2009.

Liu, Z., Kar, J., Zeng, S., Tackett, J., Vaughan, M., Avery, M., Pelon, J., Getzewich, B., Lee, K.-P., Magill, B., Omar, A., Lucker, P., Trepte, C. and Winker, D.: Discriminating between clouds and aerosols in the CALIOP version 4.1 data products, Atmospheric Measurement Techniques, 12(1), 703–734, doi:https://doi.org/10.5194/amt-12-703-2019, 2019.

Luo, C., Mahowald, N. M., and del Corral, J.: Sensitivity study of meteorological parameters on mineral aerosol mobilization, transport, and distribution, Journal of Geophysical Research: Atmospheres, 108, https://doi.org/10.1029/2003JD003483, 2003.

Luo, C., Mahowald, N. M., and del Corral, J.: Sensitivity study of meteorological parameters on mineral aerosol mobilization, transport, and distribution, Journal of Geophysical Research: Atmospheres, 108, https://doi.org/10.1029/2003JD003483, 2003.

Mahowald, N., Albani, S., Engelstaedter, S., Winckler, G., and Goman, M.: Model insight into glacial–interglacial paleodust records, Quaternary Science Reviews, 30, 832–854, https://doi.org/10.1016/j.quascirev.2010.09.007, 2011.

Mahowald, N., Luo, C., del Corral, J., and Zender, C. S.: Interannual variability in atmospheric mineral aerosols from a 22-year model simulation and observational data, Journal of Geophysical Research: Atmospheres, 108, https://doi.org/10.1029/2002JD002821, 2003.

Mahowald, N. M., Engelstaedter, S., Luo, C., Sealy, A., Artaxo, P., Benitez-Nelson, C., Bonnet, S., Chen, Y., Chuang, P. Y., Cohen, D. D., Dulac, F., Herut, B., Johansen, A. M., Kubilay, N., Losno, R., Maenhaut, W., Paytan, A., Prospero, J. M., Shank, L. M., and Siefert, R. L.: Atmospheric Iron Deposition: Global Distribution, Variability, and Human Perturbations*, Annual Review of Marine Science, 1, 245–278, https://doi.org/10.1146/annurev.marine.010908.163727, 2009.

Mahowald, N. M., Kloster, S., Engelstaedter, S., Moore, J. K., Mukhopadhyay, S., McConnell, J. R., Albani, S., Doney, S. C., Bhattacharya, A., Curran, M. a. J., Flanner, M. G., Hoffman, F. M., Lawrence, D. M., Lindsay, K., Mayewski, P. A., Neff, J., Rothenberg, D., Thomas, E., Thornton, P. E., and Zender, C. S.: Observed 20th century desert dust variability: impact on climate and biogeochemistry, Atmospheric Chemistry and Physics, 10, 10875–10893, https://doi.org/10.5194/acp-10-10875-2010, 2010.

Mamouri, R. E., Ansmann, A., Nisantzi, A., Kokkalis, P., Schwarz, A. and Hadjimitsis, D.: Low Arabian dust extinction-to-backscatter ratio, Geophysical Research Letters, 40(17), 4762–4766, doi:10.1002/grl.50898, 2013.

Mamouri, R. E. and Ansmann, A.: Fine and coarse dust separation with polarization lidar, Atmos. Meas. Tech., 7, 3717–3735, https://doi.org/10.5194/amt-7-3717-2014, 2014.

Mamouri, R. E. and Ansmann, A.: Estimated desert-dust ice nuclei profiles from polarization lidar: methodology and case studies, Atmos. Chem. Phys., 15, 3463–3477, https://doi.org/10.5194/acp-15-3463-2015, 2015.

Mamouri, R.-E. and Ansmann, A.: Potential of polarization lidar to provide profiles of CCN- and INP-relevant aerosol parameters, Atmos. Chem. Phys., 16, 5905–5931, https://doi.org/10.5194/acp-16-5905-2016, 2016.

Mamouri, R.-E. and Ansmann, A.: Potential of polarization/Raman lidar to separate fine dust, coarse dust, maritime, and anthropogenic aerosol profiles, Atmos. Meas. Tech., 10, 3403–3427, https://doi.org/10.5194/amt-10-3403-2017, 2017.

Marinou, E., Amiridis, V., Binietoglou, I., Tsikerdekis, A., Solomos, S., Proestakis, E., Konsta, D., Papagiannopoulos, N., Tsekeri, A., Vlastou, G., Zanis, P., Balis, D., Wandinger, U. and Ansmann, A.: Three-dimensional evolution of Saharan dust transport towards Europe based on a 9-year EARLINET-optimized CALIPSO dataset, Atmos. Chem. Phys., 17(9), 5893–5919, doi:10.5194/acp-17-5893-2017, 2017.

Marticorena, B. and Bergametti, G.: Modelling the atmospheric dust cycle: 1. Design of a soil drived dust emission scheme., J. Geophys. Res., 100, 16415–16430, doi:10.1029/95jd00690, 1995.

Marticorena, B., Bergametti, G., Aumont, B., Callot, Y., N'Doumé, C., and Legrand, M.: Modelling the atmospheric dust cycle: 2. Simulation of Saharan dust sources, J. Geophys. Res., 102, 4387–4404, 1997.

Mazzonia, E. and Vazquez, M.: Desertification in Patagonia, in: Natural hazards and human-exacerbated disasters in Latin America, edited by: Latrubesse, E. M., 13, 351–377, Elsevier, https://doi.org/10.1016/S0928-2025(08)10017-7, 2009.

McConnell, J. R., Aristarain, A. J., Banta, J. R., Edwards, P. R., and Simões, J. C.: 20th-century doubling in dust archived in an Antarctic Peninsula ice core parallels climate change and desertification in South America, P. Natl. Acad. Sci. USA, 104, 5743–5748, 2007.

McCave, I. N., Manighetti, B., and Robinson, S. G.: Sortable silt and fine sediment size/composition slicing: Parameters for palaeocurrent speed and palaeoceanography, Paleoceanography, 10, 593–610, https://doi.org/10.1029/94PA03039, 1995.

McGill, M. J., Yorks, J. E., Scott, V. S., Kupchock, A. W., and Selmer, P. A.: The Cloud-Aerosol Transport System (CATS): a technology demonstration on the International Space Station, in: Lidar Remote Sensing for Environmental Monitoring XV, Lidar Remote Sensing for Environmental Monitoring XV, 34–39, https://doi.org/10.1117/12.2190841, 2015.

Mortier, A., Gliß, J., Schulz, M., Aas, W., Andrews, E., Bian, H., Chin, M., Ginoux, P., Hand, J., Holben, B., Zhang, H., Kipling, Z., Kirkevåg, A., Laj, P., Lurton, T., Myhre, G., Neubauer, D., Olivié, D., von Salzen, K., Skeie, R. B., Takemura, T., and Tilmes, S.: Evaluation of climate model aerosol trends with ground-based observations over the last 2 decades – an AeroCom and CMIP6 analysis, Atmos. Chem. Phys., 20, 13355–13378, https://doi.org/10.5194/acp-20-13355-2020, 2020.

Müller, D., Ansmann, A., Mattis, I., Tesche, M., Wandinger, U., Althausen, D. and Pisani, G.: Aerosol-type-dependent lidar ratios observed with Raman lidar, Journal of Geophysical Research: Atmospheres, 112(D16), doi:10.1029/2006JD008292, 2007~~a~~.

Myriokefalitakis, S., Ito, A., Kanakidou, M., Nenes, A., Krol, M. C., Mahowald, N. M., Scanza, R. A., Hamilton, D. S., Johnson, M. S., Meskhidze, N., Kok, J. F., Guieu, C., Baker, A. R., Jickells, T. D., Sarin, M. M., Bikkina, S., Shelley, R., Bowie, A., Perron, M. M. G., and Duce, R. A.: Reviews and syntheses: the GESAMP atmospheric iron deposition model intercomparison study, Biogeosciences, 15, 6659–6684, https://doi.org/10.5194/bg-15-6659-2018, 2018.

Myriokefalitakis, S., Gröger, M., Hieronymus, J., and Döscher, R.: An explicit estimate of the atmospheric nutrient impact on global oceanic productivity, Ocean Science, 16, 1183–1205, https://doi.org/10.5194/os-16-1183-2020, 2020.

Myriokefalitakis, S., Bergas-Massó, E., Gonçalves-Ageitos, M., Pérez García Pando, C., van Noije, T., and Le Sager, P.: EC-Earth3.3.2.1-Fe., Zenodo [data set], https://doi.org/10.5281/zenodo.5752596, 2021.

Myriokefalitakis, S., Bergas-Massó, E., Gonçalves-Ageitos, M., Pérez García-Pando, C., van Noije, T., Le Sager, P., Ito, A., Athanasopoulou, E., Nenes, A., Kanakidou, M., Krol, M. C., and Gerasopoulos, E.: Multiphase processes in the EC-Earth model and their relevance to the atmospheric oxalate, sulfate, and iron cycles, Geosci. Model Dev., 15, 3079–3120, https://doi.org/10.5194/gmd-15-3079-2022, 2022.

Nenes, A., Krom, M. D., Mihalopoulos, N., Van Cappellen, P., Shi, Z., Bougiatioti, A., Zarmpas, P., and Herut, B.: Atmospheric acidification of mineral aerosols: A source of bioavailable phosphorus for the oceans, Atmospheric Chemistry and Physics, 11, 6265–6272, https://doi.org/10.5194/acp-11-6265-2011, 2011.

Neuer, S., Freudenthal, T., Davenport, R., et al.: Seasonality of sur face water properties and particle flux along a productivity gradient off NW Africa, Deep-Sea Res. II, 49, 3561–3576, 2002.

Nicolae, D., Nemuc, A., Müller, D., Talianu, C., Vasilescu, J., Belegante, L. and Kolgotin, A.: Characterization of fresh and aged biomass burning events using multiwavelength Raman lidar and mass spectrometry, Journal of Geophysical Research: Atmospheres, 118(7), 2956–2965, doi:10.1002/jgrd.50324, 2013.

Noh, Y. M., Müller, D., Lee, H. and Choi, T. J.: Influence of biogenic pollen on optical properties of atmospheric aerosols observed by lidar over Gwangju, South Korea, Atmospheric Environment, 69, 139–147, doi:10.1016/j.atmosenv.2012.12.018, 2013.

Okin, G. S., Baker, A. R., Tegen, I., Mahowald, N. M., Dentener, F. J., Duce, R. A., Galloway, J. N., Hunter, K., Kanakidou, M., Kubilay, N., Prospero, J. M., Sarin, M., Surapipith, V., Uematsu, M., and Zhu, T.: Impacts of atmospheric nutrient deposition on marine productivity: Roles of nitrogen, phosphorus, and iron, Global Biogeochemical Cycles, 25, https://doi.org/10.1029/2010GB003858, 2011.

O'Neill, N. T., Eck, T. F., Holben, B. N., Smirnov, A., Dubovik, O., and Royer, A.: Bimodal size distribution influences on the variation of Angstrom derivatives in spectral and optical depth space, J. Geophys. Res., 106, 9787–9806, 2001a.

O'Neill, N. T., Dubovik, O., and Eck, T. F.: A modified Angstrom coefficient for the characterization of sub-micron aerosols, App. Opt., 40, 2368–2374, 2001b.

O'Neill, N. T., Eck, T. F., Smirnov, A., Holben, B. N., and Thulasiraman, S.: Spectral discrimination of coarse and fine mode optical depth, J. Geophys. Res., 108, 4559–4573, https://doi.org/10.1029/2002JD002975, 2003.

Omar, A. H., Winker, D. M., Vaughan, M. A., Hu, Y., Trepte, C. R., Ferrare, R. A., Lee, K.-P., Hostetler, C. A., Kittaka, C., Rogers, R. R., Kuehn, R. E. and Liu, Z.: The CALIPSO Automated Aerosol Classification and Lidar Ratio Selection Algorithm, J. Atmos. Oceanic Technol., 26(10), 1994–2014, doi:10.1175/2009JTECHA1231.1, 2009.

Pabortsava, K., Lampitt, R. S., Benson, J., Crowe, C., McLachlan, R., Le Moigne, F. A. C., Mark Moore, C., Pebody, C., Provost, P., Rees, A. P., Tilstone, G. H., and Woodward, E. M. S.: Carbon sequestration in the deep Atlantic enhanced by Saharan dust, Nature Geosci, 10, 189–194, https://doi.org/10.1038/ngeo2899, 2017.

Pappalardo, G., Amodeo, A., Apituley, A., Comeron, A., Freudenthaler, V., Linne, H., Ansmann, A., Boesenberg, J., D'Amico, G., Mattis, I., Mona, L., Wandinger, U., Amiridis, V., Alados-Arboledas, L., Nicolae, D. and Wiegner, M.: EARLINET: towards an advanced sustainable European aerosol lidar network, Atmos. Meas. Tech., 7(8), 2389–2409, doi:10.5194/amt-7-2389-2014, 2014.

Parker, D. J., Thorncroft, C. D., Burton, R. R., and Diongue-Niang, A.: Analysis of the African easterly jet, using aircraft observations from the JET2000 experiment, Quarterly Journal of the Royal Meteorological Society, 131, 1461–1482, https://doi.org/10.1256/qj.03.189, 2005a.

Parker, D. J., Burton, R. R., Diongue-Niang, A., Ellis, R. J., Felton, M., Taylor, C. M., Thorncroft, C. D., Bessemoulin, P., and Tompkins, A. M.: The diurnal cycle of the West African monsoon circulation, Quarterly Journal of the Royal Meteorological Society, 131, 2839–2860, https://doi.org/10.1256/qj.04.52, 2005b.

Pérez, C., Haustein, K., Janjic, Z., Jorba, O., Huneeus, N., Baldasano, J. M., Black, T., Basart, S., Nickovic, S., Miller, R. L., Perlwitz, J. P., Schulz, M., and Thomson, M.: Atmospheric dust modeling from meso to global scales with the online NMMB/BSC-Dust model and ash; Part 1: Model description, annual simulations and evaluation, Atmospheric Chemistry and Physics, 11, 13001–13027, https://doi.org/10.5194/acp-11-13001-2011, 2011.

Powell, K. A., Hostetler, C. A., Vaughan, M. A., Lee, K.-P., Trepte, C. R., Rogers, R. R., Winker, D. M., Liu, Z., Kuehn, R. E., Hunt, W. H. and Young, S. A.: CALIPSO Lidar Calibration Algorithms. Part I: Nighttime 532-nm Parallel Channel and 532-nm Perpendicular Channel, J. Atmos. Oceanic Technol., 26(10), 2015–2033, doi:10.1175/2009JTECHA1242.1, 2009.

Proestakis, E., Amiridis, V., Marinou, E., Georgoulias, A. K., Solomos, S., Kazadzis, S., Chimot, J., Che, H., Alexandri, G., Binietoglou, I., Daskalopoulou, V., Kourtidis, K. A., de Leeuw, G. and Ronald, J. van der A.: Nine-year spatial and temporal evolution of desert dust aerosols over South and East Asia as revealed by CALIOP, Atmos. Chem. Phys., 18(2), 1337–1362, doi:10.5194/acp-18-1337-2018, 2018.

Proestakis, E., Amiridis, V., Marinou, E., Binietoglou, I., Ansmann, A., Wandinger, U., Hofer, J., Yorks, J., Nowottnick, E., Makhmudov, A., Papayannis, A., Pietruczuk, A., Gialitaki, A., Apituley, A., Szkop, A., Muñoz Porcar, C., Bortoli, D., Dionisi, D., Althausen, D., Mamali, D., Balis, D., Nicolae, D., Tetoni, E., Liberti, G. L., Baars, H., Mattis, I., Stachlewska, I. S., Voudouri, K. A., Mona, L., Mylonaki, M., Perrone, M. R., Costa, M. J., Sicard, M., Papagiannopoulos, N., Siomos, N., Burlizzi, P., Pauly, R., Engelmann, R., Abdullaev, S., and Pappalardo, G.: EARLINET evaluation of the CATS Level 2 aerosol backscatter coefficient product, Atmospheric Chemistry and Physics, 19, 11743–11764, https://doi.org/10.5194/acp-19-11743-2019, 2019.

Proestakis, E., Gkikas, A., Georgiou, T., Kampouri, A., Drakaki, E., Ryder, C. L., Marenco, F., Marinou, E., and Amiridis, V.: A near-global multiyear climate data record of the fine-mode and coarse-mode components of atmospheric pure dust, Atmos. Meas. Tech., 17, 3625–3667, https://doi.org/10.5194/amt-17-3625-2024, 2024.

Proestakis, E., Amiridis, V., García-Pando, C. P., Tsyro, S., Griesfeller, J., Gkikas, A., Georgiou, T., Ageitos, M. G., Escribano, J., Myriokefalitakis, S., Masso, E. B., Di Tomaso, E., Basart, S., Stuut, J.-B. W., and Benedetti, A.: Quantifying Dust Deposition over the Atlantic Ocean, Earth Syst. Sci. Data, [data set], 10.5281/zenodo.14608538, 2025.

Prospero, J. M. and Carlson, T. N.: Saharan air outbreaks over the tropical North Atlantic, Pure Appl. Geophys., 119, 677–691, https://doi.org/10.1007/BF00878167, 1981.

Prospero, J. M., 1996. Saharan dust transport over the North Atlantic Ocean and Mediterranean: an overview, in: The Impact of Desert Dust Across the Mediterranean, edited by: Guerzoni, S., and Chester, R., Kluwer Academic, Dordrecht, 133–151. https://doi.org/10.1007/978-94-017-3354-0_13.

Prospero, J. M., Glaccum, R. A., and Nees, R. T.: Atmospheric transport of soil dust from Africa to South America, Nature, 289, 570–572, https://doi.org/10.1038/289570a0, 1981.

Prospero, J. M.: Long-range transport of mineral dust in the global atmosphere: Impact of African dust on the environment of the southeastern United States, P. Natl. Acad. Sci. USA, 96, 3396–3403, 1999.

Prospero, J. M., Ginoux, P., Torres, O., Nicholson, S. E. and Gill, T. E.: Environmental Characterization of Global Sources of Atmospheric Soil Dust Identified with the Nimbus 7 Total Ozone Mapping Spectrometer (toms) Absorbing Aerosol Product, Reviews of Geophysics, 40(1), 2-1-2–31, doi:10.1029/2000RG000095, 2002.

Prospero, J. M., Nees, R. T., and Uematsu, M.: Deposition rate of particulate and dissolved aluminum derived from saharan dust in precipitation at Miami, Florida, Journal of Geophysical Research: Atmospheres, 92, 14723–14731, https://doi.org/10.1029/JD092iD12p14723, 1987.

Prospero, J. M., Collard, F.-X., Molinié, J., and Jeannot, A.: Characterizing the annual cycle of African dust transport to the Caribbean Basin and South America and its impact on the environment and air quality, Global Biogeochemical Cycles, 28, 757–773, https://doi.org/10.1002/2013GB004802, 2014.

Prospero, J. M., Landing, W. M., and Schulz, M.: African dust deposition to Florida: Temporal and spatial variability and comparisons to models, Journal of Geophysical Research: Atmospheres, 115, https://doi.org/10.1029/2009JD012773, 2010.

Ratmeyer, V., Fischer, G., and Wefer, G.: Lithogenic particle fluxes and grain size distributions in the deep ocean off northwest Africa: Implications for seasonal changes of aeolian dust input and downward transport, Deep Sea Research Part I: Oceanographic Research Papers, 46, 1289–1337, https://doi.org/10.1016/S0967-0637(99)00008-4, 1999.

Raupach, M. R., Canadell, J. G., and Le Quéré, C.: Anthropogenic and biophysical contributions to increasing atmospheric CO2 growth rate and airborne fraction, Biogeosciences, 5, 1601–1613, https://doi.org/10.5194/bg-5-1601-2008, 2008.

Remer, L. A., Kaufman, Y. J., Tanré, D., Mattoo, S., Chu, D. A., Martins, J. V., Li, R.-R., Ichoku, C., Levy, R. C., Kleidman, R. G., Eck, T. F., Vermote, E., and Holben, B. N.: The MODIS Aerosol Algorithm, Products, and Validation, https://doi.org/10.1175/JAS3385.1, 2005.

Ridley, D. A., Heald, C. L., and Ford, B.: North African dust export and deposition: A satellite and model perspective, Journal of Geophysical Research: Atmospheres, 117, https://doi.org/10.1029/2011JD016794, 2012.

~~Rittmeister, F., Ansmann, A., Engelmann, R., Skupin, A., Baars, H., Kanitz, T. and Kinne, S.: Profiling of Saharan dust from the Caribbean to western Africa - Part 1: Layering structures and optical properties from shipborne polarization/Raman lidar observations, Atmos. Chem. Phys., 17(21), 12963–12983, doi:10.5194/acp-17-12963-2017, 2017.~~

Ridley, D. A., Heald, C. L., and Ford, B.: North African dust export and deposition: A satellite and model perspective: NORTH AFRICAN DUST EXPORT AND DEPOSITION, J. Geophys. Res., 117, n/a-n/a, https://doi.org/10.1029/2011JD016794, 2012.

Ridley, D. A., Heald, C. L., and Prospero, J. M.: What controls the recent changes in African mineral dust aerosol across the Atlantic?, Atmospheric Chemistry and Physics, 14, 5735–5747, https://doi.org/10.5194/acp-14-5735-2014, 2014.

Rittmeister, F., Ansmann, A., Engelmann, R., Skupin, A., Baars, H., Kanitz, T. and Kinne, S.: Profiling of Saharan dust from the Caribbean to western Africa - Part 1: Layering structures and optical properties from shipborne polarization/Raman lidar observations, Atmos. Chem. Phys., 17(21), 12963–12983, doi:10.5194/acp-17-12963-2017, 2017.

Rodier, S., Vaughan, M., Palm, S., Yorks, J., McGill, M., Jensen, M., Murray, T., Lee, K.-P., and Trepte, C.: Laser Remote Sensing from ISS: CATS Cloud and Aerosol Data Products, Proceedings of the ILRC 2015, New York, 2015.

Rodríguez, S., Riera, R., Fonteneau, A., Alonso-Pérez, S., and López-Darias, J.: African desert dust influences migrations and fisheries of the Atlantic skipjack-tuna, Atmospheric Environment, 312, 120022, https://doi.org/10.1016/j.atmosenv.2023.120022, 2023.

Rogers, R. R., Vaughan, M. A., Hostetler, C. A., Burton, S. P., Ferrare, R. A., Young, S. A., Hair, J. W., Obland, M. D., Harper, D. B., Cook, A. L., and Winker, D. M.: Looking through the haze: evaluating the CALIPSO level 2 aerosol optical depth using airborne high spectral resolution lidar data, Atmos. Meas. Tech., 7, 4317–4340, https://doi.org/10.5194/amt-7-4317-2014, 2014.

Ryder, C. L., Marenco, F., Brooke, J. K., Estelles, V., Cotton, R., Formenti, P., McQuaid, J. B., Price, H. C., Liu, D., Ausset, P., Rosenberg, P. D., Taylor, J. W., Choularton, T., Bower, K., Coe, H., Gallagher, M., Crosier, J., Lloyd, G., Highwood, E. J., and Murray, B. J.: Coarse-mode mineral dust size distributions, composition and optical properties from AER-D aircraft measurements over the tropical eastern Atlantic, Atmos. Chem. Phys., 18, 17225–17257, https://doi.org/10.5194/acp-18-17225-2018, 2018.

Sarnthein, M., Thiede, J., P¯aumann, U., Erlenkeuser, H., Futterer, D., Koopmann, B. et al., 1982. Atmospheric and oceanic circulation patterns o€ Northwest Africa during the past 25 million years. In: von Rad, U., Hinz, K., Sarnthein, M., Seibold, E. (Eds.), Geology of the Northwest African Continental Margin. Springer-Verlag, Berlin, pp. 545-603.

Scanza, R. A., Hamilton, D. S., Perez Garcia-Pando, C., Buck, C., Baker, A., and Mahowald, N. M.: Atmospheric processing of iron in mineral and combustion aerosols: development of an intermediate-complexity mechanism suitable for Earth system models, Atmospheric Chemistry and Physics, 18, 14175–14196, https://doi.org/10.5194/acp-18-14175-2018, 2018.

Schepanski, K., Tegen, I., and Macke, A.: Saharan dust transport and deposition towards the tropical northern Atlantic, Atmospheric Chemistry and Physics, 9, 1173–1189, https://doi.org/10.5194/acp-9-1173-2009, 2009.

Schepanski, K., Heinold, B., and Tegen, I.: Harmattan, Saharan heat low, and West African monsoon circulation: modulations on the Saharan dust outflow towards the North Atlantic, Atmos. Chem. Phys., 17, 10223–10243, https://doi.org/10.5194/acp-17-10223-2017, 2017.

Schlosser, C., Klar, J. K., Wake, B. D., Snow, J. T., Honey, D. J., Woodward, E. M. S., Lohan, M. C., Achterberg, E. P., and Moore, C. M.: Seasonal ITCZ migration dynamically controls the location of the (sub)tropical Atlantic biogeochemical divide, Proceedings of the National Academy of Sciences, 111, 1438–1442, https://doi.org/10.1073/pnas.1318670111, 2014.

Schneider, D. P., C. Deser, J. Fasullo, and K. E. Trenberth, 2013: Climate Data Guide Spurs Discovery and Understanding. Eos Trans. AGU, 94, 121–122, https://doi.org/10.1002/2013eo130001.

Schneider, T., Bischoff, T., and Haug, G. H.: Migrations and dynamics of the intertropical convergence zone, Nature, 513, 45–53, https://doi.org/10.1038/nature13636, 2014.

Schubert, S. D., Rood, R. B., and Pfaendtner, J.: An Assimilated Dataset for Earth Science Applications, 1993.

Seland, Ø., Bentsen, M., Olivié, D., Toniazzo, T., Gjermundsen, A., Graff, L. S., Debernard, J. B., Gupta, A. K., He, Y.-C., Kirkevåg, A., Schwinger, J., Tjiputra, J., Aas, K. S., Bethke, I., Fan, Y., Griesfeller, J., Grini, A., Guo, C., Ilicak, M., Karset, I. H. H., Landgren, O., Liakka, J., Moseid, K. O., Nummelin, A., Spensberger, C., Tang, H., Zhang, Z., Heinze, C., Iversen, T., and Schulz, M.: Overview of the Norwegian Earth System Model (NorESM2) and key climate response of CMIP6 DECK, historical, and scenario simulations, Geoscientific Model Development, 13, 6165–6200, https://doi.org/10.5194/gmd-13-6165-2020, 2020.

Shang, X., Giannakaki, E., Bohlmann, S., Filioglou, M., Saarto, A., Ruuskanen, A., Leskinen, A., Romakkaniemi, S., and Komppula, M.: Optical characterization of pure pollen types using a multi-wavelength Raman polarization lidar, Atmos. Chem. Phys., 20, 15323–15339, https://doi.org/10.5194/acp-20-15323-2020, 2020.

Shi, Z., Krom, M. D., Bonneville, S., Baker, A. R., Bristow, C., Drake, N., Mann, G., Carslaw, K., McQuaid, J. B., Jickells, T., and Benning, L. G.: Influence of chemical weathering and aging of iron oxides on the potential iron solubility of Saharan dust during simulated atmospheric processing, Global Biogeochemical Cycles, 25, GB2010, https://doi.org/10.1029/2010GB003837, 2011.

Shimizu, A., Sugimoto, N., Matsui, I., Arao, K., Uno, I., Murayama, T., Kagawa, N., Aoki, K., Uchiyama, A., and Yamazaki, A.: Continuous observations of Asian dust and other aerosols by polarization lidars in China and Japan during ACE-Asia, J. Geophys. Res.-Atmos., 109, D19S17, https://doi.org/10.1029/2002JD003253, 2004.

Siegel, D. A. and Deuser, W. G.: Trajectories of sinking particles in the Sargasso Sea: modeling of statistical funnels above deep-ocean sediment traps, Deep Sea Research Part I: Oceanographic Research Papers, 44, 1519–1541, https://doi.org/10.1016/S0967-0637(97)00028-9, 1997.

Siegel, D. A., Granata, T. C., Michaels, A. F., and Dickey, T. D.: Mesoscale eddy diffusion, particle sinking, and the interpretation of sediment trap data, Journal of Geophysical Research: Oceans, 95, 5305–5311, https://doi.org/10.1029/JC095iC04p05305, 1990.

Sicard, M., Izquierdo, R., Alarcón, M., Belmonte, J., Comerón, A., and Baldasano, J. M.: Near-surface and columnar measurements with a micro pulse lidar of atmospheric pollen in Barcelona, Spain, Atmos. Chem. Phys., 16, 6805–6821, https://doi.org/10.5194/acp-16-6805-2016, 2016.

Simpson, D., Benedictow, A., Berge, H., Bergström, R., Emberson, L. D., Fagerli, H., Flechard, C. R., Hayman, G. D., Gauss, M., Jonson, J. E., Jenkin, M. E., Nyíri, A., Richter, C., Semeena, V. S., Tsyro, S., Tuovinen, J.-P., Valdebenito, A., and Wind, P.: The EMEP MSC-W chemical transport model – technical description, Atmos. Chem. Physics, 12, 7825–7865, https://doi.org/10.5194/acp-12-7825-2012, 2012.

Stephens, G., Winker, D., Pelon, J., Trepte, C., Vane, D., Yuhas, C., L'Ecuyer, T. and Lebsock, M.: CloudSat and CALIPSO within the A-Train: Ten Years of Actively Observing the Earth System, Bull. Amer. Meteor. Soc., 99(3), 569–581, doi:10.1175/BAMS-D-16-0324.1, 2018.

Stoffelen, A., Pailleux, J., Källén, E., Vaughan, J. M., Isaksen, L., Flamant, P., Wergen, W., Andersson, E., Schyberg, H., Culoma, A., Meynart, R., Endemann, M., and Ingmann, P.: THE ATMOSPHERIC DYNAMICS MISSION FOR GLOBAL WIND FIELD MEASUREMENT, https://doi.org/10.1175/BAMS-86-1-73, 2005.

Stuut, J.-B., Zabel, M., Ratmeyer, V., Helmke, P., Schefuß, E., Lavik, G., and Schneider, R.: Provenance of present-day eolian dust collected off NW Africa, Journal of Geophysical Research: Atmospheres, 110, https://doi.org/10.1029/2004JD005161, 2005.

~~Schubert, S. D., Rood, R. B., and Pfaendtner, J.: An Assimilated Dataset for Earth Science Applications, 1993.~~

Sugimoto, N., Uno, I., Nishikawa, M., Shimizu, A., Matsui, I., Dong, X., Chen, Y. and Quan, H.: Record heavy Asian dust in Beijing in 2002: Observations and model analysis of recent events, Geophysical Research Letters, 30(12), doi:10.1029/2002GL016349, 2003.

Tackett, J. L., Winker, D. M., Getzewich, B. J., Vaughan, M. A., Young, S. A. and Kar, J.: CALIPSO lidar level 3 aerosol profile product: version 3 algorithm design, Atmos. Meas. Tech., 11(7), 4129–4152, doi:10.5194/amt-11-4129-2018, 2018.

Tagliabue, A., Bowie, A. R., Boyd, P. W., Buck, K. N., Johnson, K. S., and Saito, M. A.: The integral role of iron in ocean biogeochemistry, Nature, 543, 51–59, https://doi.org/10.1038/nature21058, 2017.

Tegen, I., Heinold, B., Todd, M., Helmert, J., Washington, R., and Dubovik, O.: Modelling soil dust aerosol in the Bodélé depression during the BoDEx campaign, Atmos. Chem. Phys., 6, 4345–4359, https://doi.org/10.5194/acp-6-4345-2006, 2006.

Tegen, I., Harrison, S. P., Kohfeld, K., Prentice, I. C., Coe, M., and Heimann, M.: Impact of vegetation and preferential source areas on global dust aerosol: Results from a model study, Journal of Geophysical Research: Atmospheres, 107, AAC 14-1-AAC 14-27, https://doi.org/10.1029/2001JD000963, 2002.

Tegen, I., Werner, M., Harrison, S. P., and Kohfeld, K. E.: Relative importance of climate and land use in determining present and future global soil dust emission, Geophysical Research Letters, 31, https://doi.org/10.1029/2003GL019216, 2004.

Tesche, M., Ansmann, A., Müller, D., Althausen, D., Engelmann, R., Hu, M. and Zhang, Y.: Particle backscatter, extinction, and lidar ratio profiling with Raman lidar in south and north China, Appl. Opt., AO, 46(25), 6302–6308, doi:10.1364/AO.46.006302, 2007.

Tesche, M., Ansmann, A., Müller, D., Althausen, D., Engelmann, R., Freudenthaler, V., and ~~Groß~~Gross, S.: Vertically resolved separation of dust and smoke over ~~Cape Verde~~Cabo Verde using multiwavelength Raman and polarization lidars during Saharan Mineral Dust Experiment 2008, J. Geophys. Res.-Atmos., 114, D13202, https://doi.org/10.1029/2009JD011862, 2009.

Tesche, M., Gross, S., Ansmann, A., Müller, D., Althausen, D., Freudenthaler, V. and Esselborn, M.: Profiling of Saharan dust and biomass-burning smoke with multiwavelength polarization Raman lidar at ~~Cape Verde~~Cabo Verde, Tellus B: Chemical and Physical Meteorology, 63(4), 649–676, doi:10.1111/j.1600-0889.2011.00548.x, 2011.

Toth, T. D., Campbell, J. R., Reid, J. S., Tackett, J. L., Vaughan, M. A., Zhang, J., and Marquis, J. W.: Minimum aerosol layer detection sensitivities and their subsequent impacts on aerosol optical thickness retrievals in CALIPSO level 2 data products, Atmos. Meas. Tech., 11, 499–514, https://doi.org/10.5194/amt-11-499-2018, 2018.

Tsamalis, C., Chédin, A., Pelon, J., and Capelle, V.: The seasonal vertical distribution of the Saharan Air Layer and its modulation by the wind, Atmos. Chem. Phys., 13, 11235–11257, https://doi.org/10.5194/acp-13-11235-2013, 2013.

Tyson, P. D., Garstang, M., Swap, R., Kallberg, P., and Edwards, M.: An air transport climatology for subtropical southern Africa, Int. J. Climatol., 16, 265–291, 1996.

van der Does, M., Korte, L. F., Munday, C. I., Brummer, G.-J. A., and Stuut, J.-B. W.: Particle size traces modern Saharan dust transport and deposition across the equatorial North Atlantic, Atmos. Chem. Phys., 16, 13697–13710, https://doi.org/10.5194/acp-16-13697-2016, 2016.

van der Does, M., Pourmand, A., Sharifi, A., and Stuut, J.-B. W.: North African mineral dust across the tropical Atlantic Ocean: Insights from dust particle size, radiogenic Sr-Nd-Hf isotopes and rare earth elements (REE), Aeolian Research, 33, 106–116, https://doi.org/10.1016/j.aeolia.2018.06.001, 2018a.

van der Does, M., Brummer, G.-J. A., van Crimpen, F. C. J., Korte, L. F., Mahowald, N. M., Merkel, U., Yu, H., Zuidema, P., and Stuut, J.-B. W.: Tropical Rains Controlling Deposition of Saharan Dust Across the North Atlantic Ocean, Geophysical Research Letters, 47, e2019GL086867, https://doi.org/10.1029/2019GL086867, 2020.

van der Does, M., Brummer, G.-J. A., Korte, L. F., and Stuut, J.-B. W.: Seasonality in Saharan Dust Across the Atlantic Ocean: From Atmospheric Transport to Seafloor Deposition, Journal of Geophysical Research: Atmospheres, 126, e2021JD034614, https://doi.org/10.1029/2021JD034614, 2021.

van der Does, M., Knippertz, P., Zschenderlein, P., Giles Harrison, R., and Stuut, J.-B. W.: The mysterious long-range transport of giant mineral dust particles, Science Advances, 4, eaau2768, https://doi.org/10.1126/sciadv.aau2768, 2018b.

van der Jagt, H., Friese, C., Stuut, J.-B. W., Fischer, G., and Iversen, M. H.: The ballasting effect of Saharan dust deposition on aggregate dynamics and carbon export: Aggregation, settling, and scavenging potential of marine snow, Limnology and Oceanography, 63, 1386–1394, https://doi.org/10.1002/lno.10779, 2018.

van Noije, T. P. C., Le Sager, P., Segers, A. J., van Velthoven, P. F. J., Krol, M. C., Hazeleger, W., Williams, A. G., and Chambers, S. D.: Simulation of tropospheric chemistry and aerosols with the climate model EC-Earth, Geosci. Model Dev., 7, 2435–2475, https://doi.org/10.5194/gmd-7-2435-2014, 2014.

van Noije, T., Bergman, T., Le Sager, P., O'Donnell, D., Makkonen, R., Gonçalves-Ageitos, M., Döscher, R., Fladrich, U., von Hardenberg, J., Keskinen, J.-P., Korhonen, H., Laakso, A., Myriokefalitakis, S., Ollinaho, P., Pérez García-Pando, C., Reerink, T., Schrödner, R., Wyser, K., and Yang, S.: EC-Earth3-AerChem: a global climate model with interactive aerosols and atmospheric chemistry participating in CMIP6, Geoscientific Model Development, 14, 5637–5668, https://doi.org/10.5194/gmd-14-5637-2021, 2021.

Vaughan, M. A., Powell, K. A., Winker, D. M., Hostetler, C. A., Kuehn, R. E., Hunt, W. H., Getzewich, B. J., Young, S. A., Liu, Z. and McGill, M. J.: Fully Automated Detection of Cloud and Aerosol Layers in the CALIPSO Lidar Measurements, J. Atmos. Oceanic Technol., 26(10), 2034–2050, doi:10.1175/2009JTECHA1228.1, 2009.

Vaughan, M., Garnier, A., Josset, D., Avery, M., Lee, K.-P., Liu, Z., Hunt, W., Pelon, J., Hu, Y., Burton, S., Hair, J., Tackett, J. L., Getzewich, B., Kar, J. and Rodier, S.: CALIPSO lidar calibration at 1064 nm: version 4 algorithm, Atmospheric Measurement Techniques, 12(1), 51–82, doi:https://doi.org/10.5194/amt-12-51-2019, 2019.

Veselovskii, I., Goloub, P., Podvin, T., Bovchaliuk, V., Derimian, Y., Augustin, P., Fourmentin, M., Tanre, D., Korenskiy, M., Whiteman, D. N., Diallo, A., Ndiaye, T., Kolgotin, A., and Dubovik, O.: Retrieval of optical and physical properties of African dust from multiwavelength Raman lidar measurements during the SHADOW campaign in Senegal, Atmos. Chem. Phys., 16, 7013–7028, https://doi.org/10.5194/acp-16-7013-2016, 2016.

Veselovskii, I., Hu, Q., Goloub, P., Podvin, T., Barchunov, B., and Korenskii, M.: Combining Mie–Raman and fluorescence observations: a step forward in aerosol classification with lidar technology, Atmos. Meas. Tech., 15, 4881–4900, https://doi.org/10.5194/amt-15-4881-2022, 2022.

~~Vaughan, M. A., Powell, K. A., Winker, D. M., Hostetler, C. A., Kuehn, R. E., Hunt, W. H., Getzewich, B. J., Young, S. A., Liu, Z. and McGill, M. J.: Fully Automated Detection of Cloud and Aerosol Layers in the CALIPSO Lidar Measurements, J. Atmos. Oceanic Technol., 26(10), 2034–2050, doi:10.1175/2009JTECHA1228.1, 2009.~~

Vickery, K. J., Eckardt, F. D., and Bryant, R. G.: A sub-basin scale dust plume source frequency inventory for southern Africa, 2005–2008, Geophysical Research Letters, 40, 5274–5279, https://doi.org/10.1002/grl.50968, 2013.

Vignati, E., Wilson, J., and Stier, P.: M7: An efficient size-resolved aerosol microphysics module for large-scale aerosol transport models, Journal of Geophysical Research: Atmospheres, 109, https://doi.org/10.1029/2003JD004485, 2004.

Volk, T. and Hoffert, M. I.: Ocean Carbon Pumps: Analysis of Relative Strengths and Efficiencies in Ocean-Driven Atmospheric CO2 Changes, in: The Carbon Cycle and Atmospheric CO2: Natural Variations Archean to Present, American Geophysical Union (AGU), 99–110, https://doi.org/10.1029/GM032p0099, 1985.

Wallace, J. M. and Hobbs, P. V.: 3 – Atmospheric Thermodynamics, in: Atmospheric Science, 2nd edn., Academic Press, San Diego, 63–111, https://doi.org/10.1016/B978-0-12-732951-2.50008-9, 2006.

Washington, R., Bouet, C., Cautenet, G., Mackenzie, E., Ashpole, I., Engelstaedter, S., Lizcano, G., Henderson, G. M., Schepanski, K., and Tegen, I.: Dust as a tipping element: the Bodélé Depression, Chad, P. Natl. Acad. Sci. USA, 106, 20564–20571, https://doi.org/10.1073/pnas.0711850106, 2009.

Wefer, G. and Fischer, G.: Seasonal patterns of vertical particle flux in equatorial and coastal upwelling areas of the eastern Atlantic, Deep Sea Research Part I: Oceanographic Research Papers, 40, 1613–1645, https://doi.org/10.1016/0967-0637(93)90019-Y, 1993.

Weinzierl, B., Ansmann, A., Prospero, J. M., Althausen, D., Benker, N., Chouza, F., Dollner, M., Farrell, D., Fomba, W. K., Freudenthaler, V., Gasteiger, J., ~~Groß~~Gross, S., Haarig, M., Heinold, B., Kandler, K., Kristensen, T. B., Mayol-Bracero, O. L., Müller, T., Reitebuch, O., Sauer, D., Schäfler, A., Schepanski, K., Spanu, A., Tegen, I., Toledano, C. and Walser, A.: The Saharan Aerosol Long-Range Transport and Aerosol–Cloud-Interaction Experiment: Overview and Selected Highlights, Bull. Amer. Meteor. Soc., 98(7), 1427–1451, doi:10.1175/BAMS-D-15-00142.1, 2016.

Wiegner, M., ~~Groß~~Gross, S., Freudenthaler, V., Schnell, F. and Gasteiger, J.: The May/June 2008 Saharan dust event over Munich: Intensive aerosol parameters from lidar measurements, Journal of Geophysical Research: Atmospheres, 116(D23), doi:10.1029/2011JD016619, 2011.

Winker, D. M., Hunt, W. H., and McGill, M. J.: Initial performance assessment of CALIOP, Geophysical Research Letters, 34, https://doi.org/10.1029/2007GL030135, 2007.

Winker, D. M., Vaughan, M. A., Omar, A., Hu, Y., Powell, K. A., Liu, Z., Hunt, W. H. and Young, S. A.: Overview of the CALIPSO Mission and CALIOP Data Processing Algorithms, J. Atmos. Ocean. Technol., 26(11), 2310–2323, doi:10.1175/2009JTECHA1281.1, 2009.

Winker, D. M., Pelon, J., Coakley, J. A., Ackerman, S. A., Charlson, R. J., Colarco, P. R., Flamant, P., Fu, Q., Hoff, R. M., Kittaka, C., Kubar, T. L., Le Treut, H., Mccormick, M. P., Mégie, G., Poole, L., Powell, K., Trepte, C., Vaughan, M. A. and Wielicki, B. A.: The CALIPSO MissionA Global 3D View of Aerosols and Clouds, Bull. Amer. Meteor. Soc., 91(9), 1211–1230, doi:10.1175/2010BAMS3009.1, 2010.

Winker, D. M., Tackett, J. L., Getzewich, B. J., Liu, Z., Vaughan, M. A. and Rogers, R. R.: The global 3-D distribution of tropospheric aerosols as characterized by CALIOP, Atmospheric Chemistry and Physics, 13(6), 3345–3361, doi:https://doi.org/10.5194/acp-13-3345-2013, 2013.

Yorks, J. E., McGill, M. J., Palm, S. P., Hlavka, D. L., Selmer, P. A., Nowottnick, E. P., Vaughan, M. A., Rodier, S. D., and Hart, W. D.: An overview of the CATS level 1 processing algorithms and data products, Geophysical Research Letters, 43, 4632–4639, https://doi.org/10.1002/2016GL068006, 2016.

Young, S. and Vaughan, M.: The retrieval of profiles of particulate extinction from Cloud Aerosol Lidar Infrared Pathfinder Satellite, Observations (CALIPSO) data: algorithm description, J. Atmos. Ocean. Tech., 26, 1105–1119, https://doi.org/10.1175/2008JTECHA1221.1, 2009.

Yu, H., Remer, L. A., Kahn, R. A., Chin, M., and Zhang, Y.: Satellite perspective of aerosol intercontinental transport: From qualitative tracking to quantitative characterization, Atmospheric Research, 124, 73–100, https://doi.org/10.1016/j.atmosres.2012.12.013, 2013.

Yu, H., Chin, M., Yuan, T., Bian, H., Remer, L. A., Prospero, J. M., Omar, A., Winker, D., Yang, Y., Zhang, Y., Zhang, Z., and Zhao, C.: The fertilizing role of African dust in the Amazon rainforest: A first multiyear assessment based on data from Cloud-Aerosol Lidar and Infrared Pathfinder Satellite Observations, Geophysical Research Letters, 42, 1984–1991, https://doi.org/10.1002/2015GL063040, 2015a.

Yu, H., Chin, M., Bian, H., Yuan, T., Prospero, J. M., Omar, A. H., Remer, L. A., Winker, D. M., Yang, Y., Zhang, Y., and Zhang, Z.: Quantification of trans-Atlantic dust transport from seven-year (2007–2013) record of CALIPSO lidar measurements, Remote Sensing of Environment, 159, 232–249, https://doi.org/10.1016/j.rse.2014.12.010, 2015b.

Yu, H., Tan, Q., Chin, M., Remer, L. A., Kahn, R. A., Bian, H., Kim, D., Zhang, Z., Yuan, T., Omar, A. H., Winker, D. M., Levy, R. C., Kalashnikova, O., Crepeau, L., Capelle, V., and Chédin, A.: Estimates of African Dust Deposition Along the Trans-Atlantic Transit Using the Decadelong Record of Aerosol Measurements from CALIOP, MODIS, MISR, and IASI, Journal of Geophysical Research: Atmospheres, 124, 7975–7996, https://doi.org/10.1029/2019JD030574, 2019.

Yu, H., Zhou, Y., Bian, H., and Song, Q.: Godzilla dust plume: Evolution of MODIS and GEOS AOD from June 10 to 30, 2020, TIB, https://doi.org/10.5446/50830, 2021.

Zender, C., Bian, H., and Newman, D.: Mineral Dust Entrainment and Deposition (DEAD) model: Description and 1990s dust climatology., J. Geophys. Res., 108, 4416–4437, doi:10.1029/2002jd002775, 2003.

Zeng, S., Vaughan, M., Liu, Z., Trepte, C., Kar, J., Omar, A., Winker, D., Lucker, P., Hu, Y., Getzewich, B. and Avery, M.: Application of high-dimensional fuzzy k-means cluster analysis to CALIOP/CALIPSO version 4.1 cloud–aerosol discrimination, Atmospheric Measurement Techniques, 12(4), 2261–2285, doi:https://doi.org/10.5194/amt-12-2261-2019, 2019.

Zhang, K., O'Donnell, D., Kazil, J., Stier, P., Kinne, S., Lohmann, U., Ferrachat, S., Croft, B., Quaas, J., Wan, H., Rast, S., and Feichter, J.: The global aerosol-climate model ECHAM-HAM, version 2: sensitivity to improvements in pro- cess representations, Atmos. Chem. Phys., 12, 8911–8949, https://doi.org/10.5194/acp-12-8911-2012, 2012.